HIGH FREQUENCY BACKSCATTER FROM THE POLAR AND AURORAL E-REGION IONOSPHERE

By

Victoriya V. Forsythe, B.S.

A Dissertation Submitted in Partial Fulfillment of the Requirements

for the Degree of

Doctor of Philosophy

in

Space Physics

University of Alaska Fairbanks

May 2017

APPROVED:

William Bristow, Committee Chair
Mark Conde, Committee Member
John Sahr, Committee Member
Hui Zhang, Committee Member
Renate Wackerbauer, Chair
Department of Physics
Paul Layer, Dean
College of Natural Science and Mathematics
Michael Castellini, *Dean of the Graduate School*

Abstract

The Earth's ionosphere contains collisional and partially-ionized plasma. The electric field, produced by the interaction between the Earth's magnetosphere and the solar wind, drives the plasma bulk motion, also known as convection, in the F-region of the ionosphere. It can also destabilize the plasma in the E-region, producing irregularities or waves. Intermediate-scale waves with wavelengths of hundreds of meters can cause scintillation and fading of the Global Navigation Satellite System (GNSS) signals, whereas the small-scale waves ($\lambda < 100$ m) can scatter radar signals, making possible detection of these plasma structures and measurements of their characteristics such as their phase velocity and intensity. In this work, production of the decameter-scale ($\lambda \approx 10$ m) irregularities in the ionospheric E-region (100–120 km in altitude) at high latitudes is investigated both theoretically, using linear fluid theory of plasma instability processes that generate small-scale plasma waves, and experimentally, by analyzing data collected with the newly-deployed high-southern-latitude radars within the Super Dual Auroral Radar Network (SuperDARN). The theoretical part of this work focuses on symmetry properties of the general dispersion relation that describes wave propagation in the collisional plasma in the two-stream and gradient-drift instability regimes. The instability growth rate and phase velocity are examined under the presence of a background parallel electric field, whose influence is demonstrated to break the spatial symmetry of the wave propagation patterns. In the observational part of this thesis, a novel dual radar setup is used to examine E-region irregularities in the magnetic polar cap by probing the E-region along the same line from opposite directions. The phase velocity analysis together with raytracing simulations demonstrated that, in the polar cap, the radar backscatter is primarily controlled by the plasma density conditions. In particular, when the E-region layer is strong and stratified, the radar backscatter properties are controlled by the convection velocity, whereas for a tilted E-layer, the height and aspect angle conditions are more important. Finally, the fundamental dependence of the E-region irregularity phase velocity on the component of the plasma convection is investigated using two new SuperDARN radars at high southern latitudes where plasma convection estimates are accurately deduced from all SuperDARN radars in the southern hemisphere. Statistical analysis is presented showing that the predominance of the E-region echoes of a particular polarity is strongly dictated by the orientation of the convection plasma flow which itself has a significant asymmetry towards westward zonal flow.

Table of Contents

List of Figures

List of Tables

Acknowledgements

I would like to thank my committee chair Dr. William Bristow, and the committee members, Dr. Mark Conde, Dr. John Sahr, and Dr. Hui Zhang for your insightful questions, comments and suggestions during our committee meetings.

Thank you to all the professors of the University of Alaska Fairbanks who taught the graduate courses and shared their knowledge of physics with me.

A very special thank you goes to my fellow doctoral student, Leslie Lamarche, who shared with me both good and challenging moments of our PhD journey.

Thank you to all Physics Graduate Student Association members, it was always fun to explore the beautiful Alaskan nature with all of you.

A very dear thank you to Jeffree Forsythe, I would not survive through first two years of graduate school without your love and support. Thank you for moving to Alaska with me and always believing in me.

Thank you to my Mom and Dad. Even being on another side of the world, I always felt your support and kept going to make you proud. I would like to dedicate this work to two of you, you are my everything.

Nomenclature

AACGM	altitude-adjusted corrected geomagnetic
ACF	autocorrelation function
AEH	anomalous electron heating
BPK	SuperDARN TIGER Buckland Park
CCI	current-convective instability
CIRA	COSPAR International Reference Atmosphere
DCE	SuperDARN Dome Concordia East
DMSP	Defense Meteorological Satellite Program
EISCAT	European Incoherent Scatter
ETI	electron thermal instability
FBI	Farley-Buneman instability
FoV	field-of-view
GDI	gradient-drift instability
GNSS	Global Navigation Satellite System
HAIR	High Aspect angle Irregularity Region
HAL	SuperDARN Halley
HF	high frequency
IDM	Ion Drift Meter
IMF	Interplanetary Magnetic Field
IRI	International Reference Ionosphere model
ISR	incoherent scatter radar
ITI	ion thermal instability
KER	SuperDARN Kergulen
LOS	line-of-sight
LT	local time
MCM	SuperDARN McMurdo
MHD	magnetohydrodynamic
MLAT	magnetic latitude
MLT	magnetic local time
MSISE	Mass Spectrometer and Incoherent Scatter Extension
PIC	particle-in-cell

PRF	pulse repetition frequency
RTI	range-time-intensity
SAN	SuperDARN Sanae
SNR	signal-to-noise ratio
SPS	SuperDARN South Pole Station
STARE	Scandinavian Twin Auroral Radar Experiment
SuperDARN	Super Dual Auroral Radar Network
SYE	SuperDARN Syowa East
SYS	SuperDARN Syowa South
TIG	SuperDARN TIGER Tasmania
UNW	SuperDARN TIGER Unwin
UT	universal time
VHF	very high frequency
ZHO	SuperDARN Zhongshan

Chapter 1
Introduction

> Beginnings are usually scary, and endings are usually sad,
> but it's everything in between that makes it all worth living.
>
> — Bob Marley

This thesis is concerned with a phenomenon that is called "radar aurora", which refers to the scattering of the radio waves from coherent irregularities in the plasma density of the ionosphere. Starting from the definition of plasma and the description of the near-Earth plasma environment, Section 1.1 gradually introduces main geophysical processes in the auroral and polar ionosphere. Sections 1.2 and 1.3 present reviews of theoretical and experimental work on E-region plasma irregularities, respectively. Section 1.4 presents the motivation, objectives, and outline of this thesis.

1.1 The Near-Earth Space Environment

In the universe matter exists in four different fundamental states. Figure 1.1 illustrates the conversion of one state of matter into another with an increasing temperature. At low temperatures, matter is in a solid state with atoms arranged in well-organized grids. When temperature increases above a critical value, solid matter melts and takes a form of a liquid, in which molecular bonds are maintained but the grid of atoms is broken. If the temperature keeps increasing above the second critical point, the liquid will eventually turn into a gas. What distinguishes the gas from liquids and solids is the vast separation of the individual gas particles and the fact that gas will take all the space given to it. If temperature increases even further, the electrons will get stripped of the atoms turning them into ions. The gas that is fully or partially ionized is called *plasma*, the fourth state of matter.

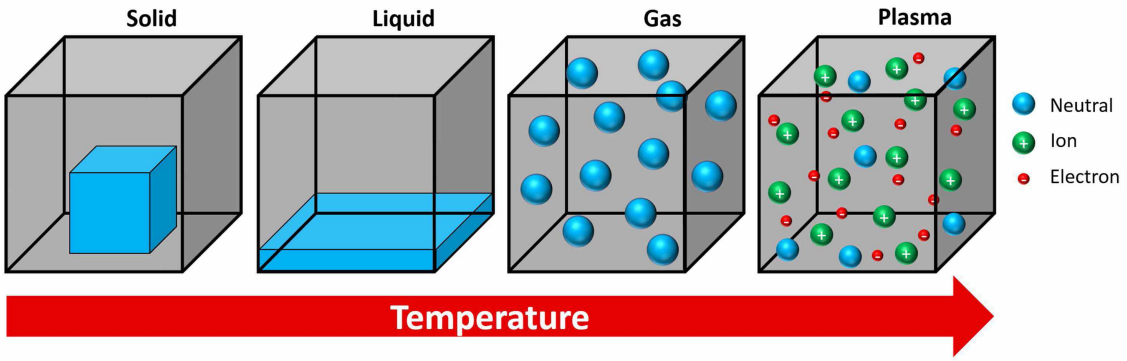

Figure 1.1. Four fundamental states of matter under increasing temperature.

To understand what it means "to be plasma", one needs to look at its fundamental properties, since these are significantly different from properties of the other three states of matter. Because the plasma is made of the electrically charged particles, it is strongly influenced by electric and magnetic fields. The differential motions of the ions and electrons as a reaction to the externally imposed fields create electric currents. In addition to the externally imposed fields, the localized charge concentration and electric currents create the fields within the plasma. In contrast to the neutral gas, the plasma behavior has a coherent and collective quality. Because of the approximately equal numbers of positively and negatively charged particles the plasma is said to be quasi-neutral.

There are not many examples of naturally occurring plasma that we can refer to in our everyday life. The few of them are lightning strikes, upper atmospheric phenomenon called sprites, and certain parts of fire. However, man-made plasmas have permeated our modern life and can be found in TV screens, fluorescent lamps, neon signs, and plasma-based propulsion systems. Despite appearances though, our little corner of the universe is nearly the only place (apart from other planets and non-ionized nebulaes) where the plasma is not an abundant state of matter. Above an altitude of 80 km, most matter is in the state of plasma. It has often been quoted that plasma composes as much as 99% of the visible universe. The Sun and other stars, the solar wind, the interplanetary and interstellar medium, the hot gas between galaxies, all are in the state of plasma.

1.1.1 Magnetospheric Regions

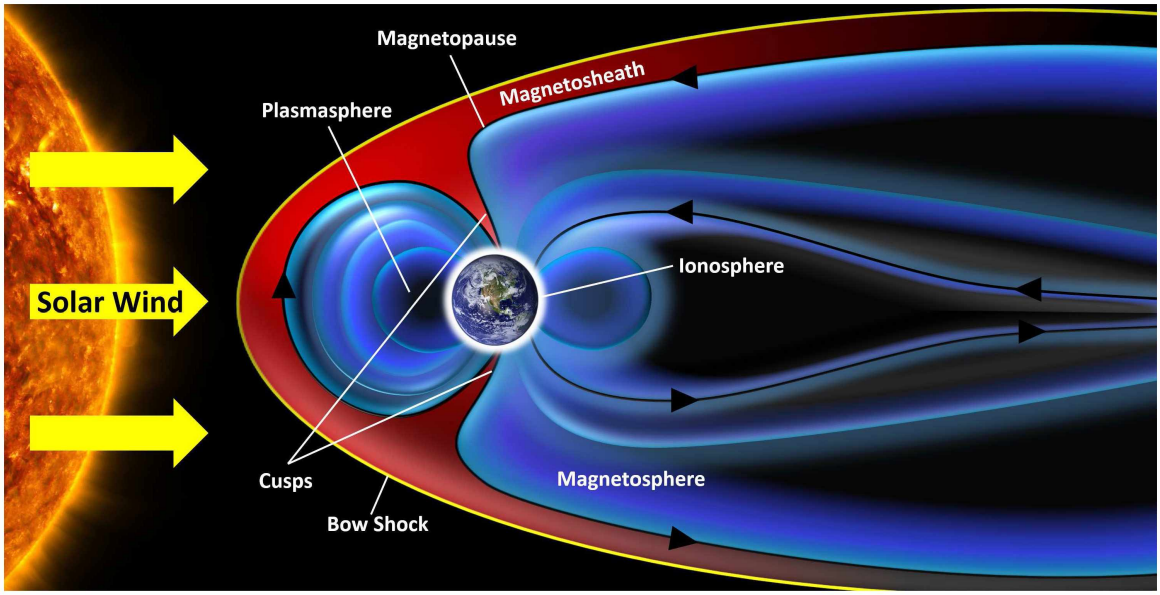

Figure 1.2. Earth's local plasma environment.

Figure 1.2 shows the local plasma environment of the Earth, which is highly influenced by the Sun's activity. The Sun's outermost region, *solar corona*, is characterized by the hot plasma that streams outward in all directions. This flow of plasma is known as the *solar wind* and is highly conductive and carries the "frozen-in" *Interplanetary Magnetic Field* (IMF). The frozen-in condition implies that plasma and the magnetic field move together. The Earth has an internally produced dipole-like planetary magnetic field that shields the Earth from the constantly blowing solar wind. Under pressure from the supersonic solar wind, the Earth's *magnetosphere* is compressed on the dayside forming the *bow shock*. On the nightside, the solar wind stretches the Earth's magnetosphere a few hundreds of the Earth radii (R_E) away from the Sun, forming the *magnetotail*. The region just inside of the bow shock, where the plasma has been slowed, is called the *magnetosheath* (shown in red in Figure 1.2), while the outer boundary of the magnetosphere is called the *magnetopause*. Energetic particles of the solar wind can penetrate to the magnetosphere through the *cusp* regions leading to the magnetic poles. The *ionosphere* envelops the entire Earth and reflects the processes in the whole geospace environment. The ionosphere has a direct coupling to the Sun via ultraviolet and X-ray radiation, as well as indirect but very strong coupling via

geomagnetic processes. The system of these four regions is called the *solar-terrestrial* or *geospace environment*.

1.1.2 Ionospheric Regions

The Earth's ionosphere is mainly formed through the processes of *photoionization* and *particle precipitation* in the upper atmosphere. The process of photoionization is a primary source of charged particles and it occurs when solar photons charge the neutral atmospheric molecules by removing their electrons. A second and very important ionization process is due to the particle precipitation. The charged particles in a plasma gyrate around the magnetic field lines of the Earth and are free to move along these field lines. The magnetic field magnitude increases towards magnetic poles, which creates a situation similar to a magnetic bottle, where the particle bounces from pole to pole performing a *magnetic mirroring*. The mirroring point can be deep within the atmosphere where a bouncing particle is likely to instead collide with a neutral particle and ionize it through the process that is called *impact ionization*.

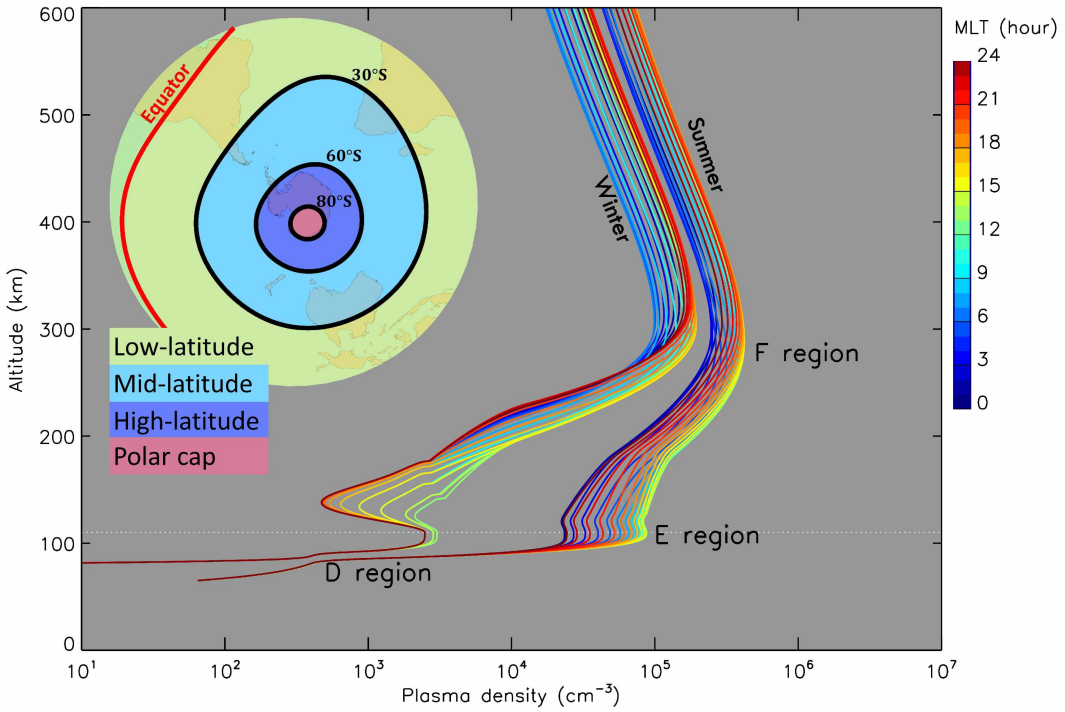

Figure 1.3. Latitudinal domains of the ionosphere and the plasma density profiles for winter and summer months color-coded in MLT. The separation into latitudinal domains is based on magnetic latitudes which are obtained from the AACGM coordinate system.

It is common to divide the ionosphere into three latitudinal zones with different ionospheric properties. This is in part because the photoionization is controlled by the amount of the solar radiation and the solar zenith angle, whereas the particle precipitation is restricted to the area around the poles. Figure 1.3 shows these three zones in the top-left corner as filled color contours. Low-latitude zone occurs below the magnetic latitude (MLAT) of 30°, mid-latitude zone extends from 30° to 60°, and the high-latitude zone extends above 60° [*Hunsucker and Hargreaves*, 2003]. In Figure 1.3 one more nominal latitudinal zone, the polar cap, is shown above the MLAT of 80°. In this presentation the polar cap is very approximately shown as a fixed area, whereas in practice it is defined as a region with "open" field lines that expands and contracts according to geomagnetic activity. The lines of equal MLATs in Figure 1.3 were obtained from the altitude-adjusted corrected geomagnetic (AACGM) coordinate system model with 2010 coefficients [*Shepherd*, 2014]. The plasma processes in the high-latitude zone and the polar cap in the southern hemisphere are the primary focus of this research.

Along with the latitudinal variation, the ionosphere has a particular altitudinal structure. A set of ionospheric density profiles obtained from the International Reference Ionosphere (IRI) model is presented on the right of Figure 1.3. The model has been run for the location (−77.88° Lat, 166.73° Lon, geographic) inside of the magnetic polar cap, on June 13 and February 13, 2013. The color of the lines indicates the magnetic local time (MLT), also based on the AACGM model. As can be seen in Figure 1.3, the ionosphere has three distinct layers or regions. The lowest portion of the ionosphere is called the D-region and it has a peak at about 80 km altitude. The next region peaks at about 110 km and is called the E-region, followed by the F-region with a peak at about 300 km. Figure 1.3 shows that the density peaks in the E- and F-regions exhibit significant variations with season and time of the day. For example, the E-region peak density is about two orders of magnitude higher in February than in June. In addition, the peak density at magnetic noon (green line in Figure 1.3) is almost twice as high as that at midnight (dark red line). These seasonal and diurnal variations of the ionospheric plasma density arise mostly because of the different solar illumination of the different latitudinal zones together with the diurnal change in the solar zenith angle.

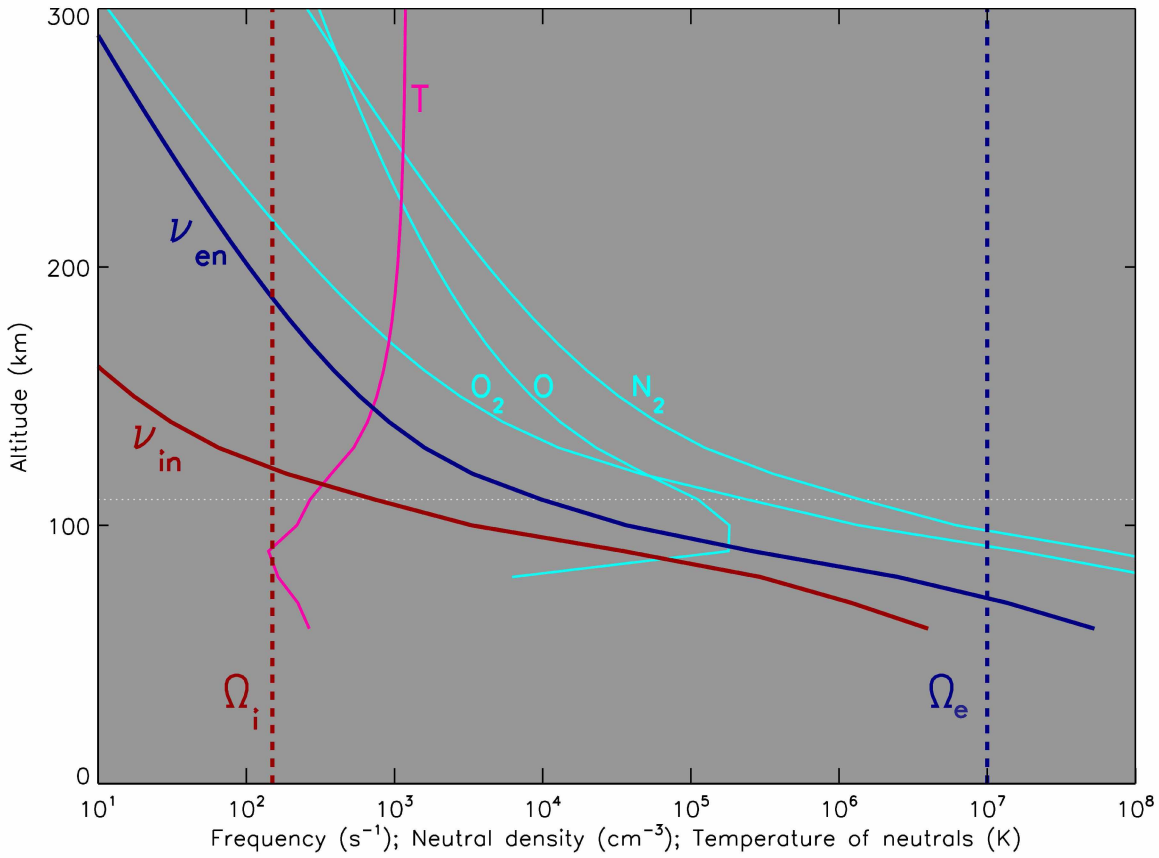

Figure 1.4. Altitude variation of the collision frequency between the charged and neutral particles (ν_{en} and ν_{in}), gyrofrequencies of electrons and ions (Ω_e and Ω_i), density of the neutral species, and the temperature of the neutrals (T).

In addition to the plasma density varying with altitude, the neutral density and collision frequency between the charged and neutral particles also change significantly with height. Figure 1.4 shows how the density of the three dominant neutral particles O, O_2 and N_2 changes with altitude (cyan lines). This result was obtained from the Mass Spectrometer and Incoherent Scatter Extension (MSISE-90) model [*Hedin*, 1991] (Section 3.4), using the same coordinates as in Figure 1.3 for December 01, 2013. The density of the neutral species roughly follows the barometric altitudinal dependency. The temperature of the neutrals, obtained from MSISE-90 as well, is shown in magenta color. The collision frequency between the neutral and charged particles can be calculated from the density and temperature of the neutrals using the standard expressions given by *Schunk and Nagy* [1978]. The resultant collision frequencies between neutrals and ions (ν_{in}) and neutrals and electrons (ν_{en}) are shown in red and blue, respectively. The difference between the collision frequencies at the

F- and E-region heights is as large as about 5 orders of magnitude. This plays a great role in the plasma motions in the E- and F-regions.

In the high-latitude ionosphere, electric fields exist as a consequence of the interaction between the solar wind and the magnetosphere. The solar wind "drags" the magnetic flux tubes from the dayside to the nightside of the magnetosphere. The charged particles can move freely along the magnetic field lines, therefore the magnetic field lines act as equipotential lines for the electric field. The electric fields mapped from the magnetosphere to the ionosphere are shown with yellow arrows in Figure 1.5 and the equipotential contours (or equivalently the bulk plasma motion lines) for this electric field are shown in pink. In Figure 1.5, the numerical annotations represent the MLT with midday located at the top of the figure and dotted lines representing the lines of equal MLATs. The magnetic field is directed out of the page, as indicated by the circles with the dots. The bulk plasma motion is strongly controlled by the relative magnitudes of the collision frequency and the strength of the electric field. At F-region altitudes, the gyrofrequencies $\Omega_\alpha \equiv q_\alpha B/m_\alpha$ of ions and electrons, shown with dashed lines in Figure 1.4, are much greater than collision frequencies with neutrals. In other words, the motion of both ions and electrons are strongly controlled by the magnetic field, which results in the $\mathbf{E} \times \mathbf{B}$ drift motion of both species. Thus, both electrons and ions follow two-cell convective motion along the equipotential lines, with the antisunward direction inside the polar cap and sunward direction along the lines of equal MLAT in the high-latitude region. Figure 1.5 represents an ideal case, when both convection cells are equal. In reality, convection patterns can deviate significantly from the symmetric two-cell pattern, with a significant dawn-dusk asymmetry, and even consist of

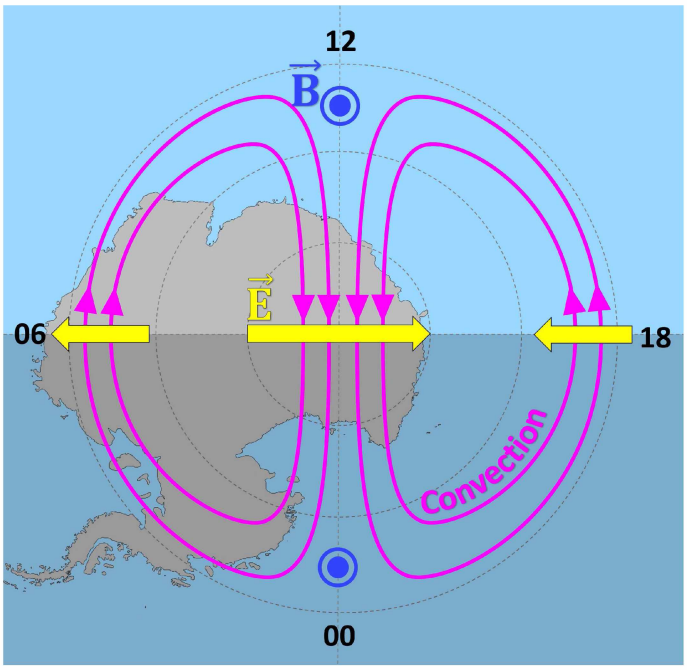

Figure 1.5. F-region plasma convection and the convection electric fields.

multiple convection cells, depending on the strength and the direction of IMF. In short, the ionospheric convection is a reflection of the complicated coupling processes between the solar wind and the magnetosphere.

In the E-region, the collision frequency between the ions and neutrals ν_{in} is significantly larger than that in the F-region. This can be seen in Figure 1.4, where at a height of 110 km, shown with the white dashed line, the gyrofrequency Ω_i is less than ν_{in}. In other words, the ions are not fully magnetized in the E-region, but collisional. The electrons, on the other hand, are still magnetized and exhibit the same behavior as their F-region counterparts. The mean free path of the ions exponentially increases with altitude; for example, at an altitude of 100 km, the ion mean free path is several centimeters and at an altitude of 130 km it is several meters. Because of the differences in collisional effects with neutrals, the ions and electrons no longer move together with the same velocity. The differential flow between electrons and ions causes ionospheric currents in the opposite direction to the electron flow.

In the D-region, the plasma density is much lower (see Figure 1.3), the density of the neutral particles is much greater (see Figure 1.4), and the collisions between the electrons and the neutrals are much more frequent than in the E- and F-regions. As a result, the electrons are no longer magnetized and the neutral wind almost fully controls the plasma flow.

The content and properties of the ionosphere change with the geomagnetic location and altitude, defining the nominal latitudinal zones and the altitudinal regions. In the current body of work, the focus is on the E- and F-regions of the high-latitude and polar cap zones.

1.2 Review of the Theory of the *E*-Region Irregularities

Besides latitudinal and altitudinal structure, the plasma in the ionosphere is not uniform at smaller scales. During the early radar experiments at auroral latitudes, *Eckersley* [1937] and *Harang and Stoffregen* [1938] reported the detection of radio echoes from an unknown source that was ~10 m in size at the E-region heights. They called this source of the radar backscatter an irregular ionic clouds or *irregularities*. Only in the 1960s the first theories of the density irregularity formation were developed. In this section, an updated review of the theory of the ionospheric plasma irregularities is presented, focusing on the E-region and arbitrary-altitude theories developed more recently.

The pioneers in developing the theory of the ionospheric irregularities were *Farley* [1963], who developed a kinetic approach, and *Buneman* [1963], who used a fluid approach. They proposed that the plasma in the E-region ionosphere becomes unstable when the differential motion between the fast moving magnetized electrons and the collisional slow ions exceeds the ion-acoustic speed, which is the speed of the sound waves propagating in plasma; this instability was named the *modified two-stream* or *Farley-Buneman instability* (FBI). Later it was discovered that other factors can also destabilize plasma, including a significant plasma density gradient in the direction of the local electric field [*Simon*, 1963; *Hoh*, 1963]. This instability is called the *gradient-drift instability* (GDI). Both FBI and GDI are considered to be the primary mechanisms that give growth to the waves or irregularities in the density of the plasma. In the E-region, GDI is operational when the electric field is not high enough to drive the FBI instability, with the gradient along the electric field effectively lowering the necessary threshold electric field. A similar process also occurs in the F-region, except that the threshold is much lower there. In cases when the density gradient is not strong enough to make GDI operational, the current antiparallel to the magnetic field can destabilize the plasma, giving rise to the so called *current-convective instability* (CCI) [*Ossakow and Chaturvedi*, 1979].

The plasma instability processes can be described using the fluid approach, according to which the ionospheric plasma is treated as two inter-penetrating fluids of electrons and ions, both being coupled to the background of the neutral particles through the collisional terms in the momentum equations. The fundamental fluid equations that describe the evolution of density and velocity of plasma species $\alpha = i, e$ (ions and electrons, respectively) are continuity, momentum, and energy equations

$$\frac{\partial n_\alpha}{\partial t} + \nabla \cdot (n_\alpha \mathbf{V}_\alpha) = 0, \tag{1.1}$$

$$m_\alpha \frac{D\mathbf{V}_\alpha}{Dt} = q_\alpha (\mathbf{E} + \mathbf{V}_\alpha \times \mathbf{B}) - \nu_\alpha m_\alpha (\mathbf{V}_\alpha - \mathbf{U}) - \frac{\nabla (n_\alpha T_\alpha)}{n_\alpha}, \tag{1.2}$$

$$n_\alpha^{2/3} \frac{D}{Dt} \left(\frac{T_\alpha}{n_\alpha^{2/3}} \right) = \frac{2}{3} M_{\alpha n} \nu_\alpha V_\alpha^2 - \delta_{\alpha n} \nu_\alpha (T_\alpha - T_n). \tag{1.3}$$

Here $q_\alpha, m_\alpha, \mathbf{V}_\alpha, n_\alpha, \nu_\alpha$, and T_α denote charge, mass, velocity, number density, temperature expressed in energy units, and collision frequency with neutrals of species α; $\mathbf{E}$ and $\mathbf{B}$ are the electric and magnetic fields; $\mathbf{U}$ is the neutral wind velocity; $M_{\alpha n} = m_\alpha m_n/(m_\alpha + m_n)$ is the reduced mass of the two colliding particles (α and a neutral particle n); $\delta_{\alpha n}$ is the average fraction of energy lost by the particle of the kind α during one $\alpha - n$ collision; and D/Dt is the convective derivative.

All studies that use fluid approach utilize a set of assumptions that is applicable to the wave formation in the ionospheric plasma. The first assumption relates to the definition of the plasma, i.e. the *quasineutrality* property of the plasma particles that can be expressed in terms of their densities as $n_e = n_i = n$ which also can be rewritten in terms of their perturbed quantities $\delta n_e = \delta n_i = \delta n$. The second assumption is the *local approximation*, namely that the typical scale of the background gradient is much larger than the wavelength or, equivalently, that the gradient density normalized to the density is much smaller than the wave number $\nabla n/n \ll k$. These two assumptions can, in principle, be applied to any region of the ionosphere.

The fluid theories can also be divided into two large groups. In the first group of the *isothermal theories*, the ion and electron temperatures are assumed to be constant ($T_\alpha = const$), in which case the fluid equation set is truncated to Equations (1.1) and (1.2). In the second group, no such assumption is made and these theories are called *nonisothermal*. In the below review, both groups are considered, with some focus on the isothermal theories.

As mentioned before, the behavior of the electrons and ions in the E- and F-regions are significantly different. During the development of the instability theory for isothermal plasma, the dispersion relation was derived separately for the E-region [*Buneman*, 1963; *Rogister and D'Angelo*, 1970] and F-region [*Linson and Workman*, 1970; *Ossakow et al.*, 1978; *Ossakow and Chaturvedi*, 1979; *Keskinen and Ossakow*, 1982]. This included theories

that considered GDI only [*Linson and Workman*, 1970; *Ossakow et al.*, 1978; *Makarevich*, 2014], combined FBI/GDI [*Rogister and D'Angelo*, 1970], and combined GDI/CCI [*Ossakow and Chaturvedi*, 1979; *Keskinen and Ossakow*, 1982]. A general progression towards the approach that integrates FBI and GDI at different altitudinal regions has also occured [*Rogister and D'Angelo*, 1970; *Sudan et al.*, 1973; *Fejer et al.*, 1975; *Fejer et al.*, 1984]. This progression resulted in the development of the general dispersion relation that combined FBI, GDI, and CCI and is valid for a wide range of altitudes spanning the E- and F-regions [*Dimant and Oppenheim*, 2011a; *Makarevich*, 2016a, b]. Table 1.1 summarizes the isothermal fluid theories, including the used approximations, the order of the wave frequency ω in the dispersion equation, and the references. The notation D_α/Dt in Table 1.1 is the convective derivative with the velocity $\mathbf{V}_\alpha$. One can see from Table 1.1 that with an increasing generality (i.e. fewer assumptions used), the order of the dispersion relation in frequency increases. This resulted in the more advanced numerical methods being applied to find solutions of the dispersion relations [*Makarevich*, 2016a, b]. In the theoretical study presented in Chapter 2 of this body of work, the general dispersion relation of the fourth order derived by *Makarevich* [2016a] is used and analyzed.

In the case of nonisothermal theories, in addition to Equations (1.1) and (1.2), the plasma energy Equation (1.3) is also considered in order to describe the thermal diffusion [*Dimant and Oppenheim*, 2004]. This set of 3 equations is often called 5-moment transport equations. In the case when the thermoelectric effects are considered, the fourth equation is added that describes the heat flow processes, creating a set of equations called 8–moment transport equations [*Kissack et al.*, 1997, 2008a].

Using these 5- or 8-moment equation sets, the electron thermal effects have been shown to result in an additional type of instability, called the *electron thermal instability* (ETI) [*Dimant and Sudan*, 1997; *Kissack et al.*, 1997; *St.-Maurice and Kissack*, 2000; *Kagan and St.-Maurice*, 2004; *Kissack et al.*, 2008a, b], while ion thermal effects result in the *ion thermal instability* (ITI)[e.g. *Dimant and Oppenheim*, 2004]. In addition, the contribution of the neutral wind in the E-region can be strong enough to drive the thermal instability through the frictional heating by collisions [*Kagan and Kelley*, 2000]. Finally, in the most recent theoretical work by *St.-Maurice and Chau* [2016], the nonisothermal ion and electron effects and the variation of the ion drift with altitude have recently been considered, which allowed to explain the slow-narrow spectra of the E-region waves [*Chau and St.-Maurice*, 2016].

Table 1.1. Development of isothermal linear fluid theory, with major instability cases, their altitudinal domains, approximations used, orders of resulting dispersion relation in the oscillation frequency ω, and references.

Mode	Domain	Approximations	Order in ω	Reference
FBI	Main E-region near 110 km	$D_i/Dt \ll \nu_i$, $\nu_e \ll \Omega_e$, $\nu_i \gg \Omega_i$	2	*Buneman* [1963]
GDI Pedersen mode	Main F-region near 200 km	$D_\alpha/Dt \ll \nu_\alpha$, $\nu_\alpha \ll \Omega_\alpha$, $k_\parallel = 0$	1	*Linson and Workman* [1970]
FBI/GDI Hall mode	Main E-region near 110 km	$D_i/Dt \ll \nu_i$, $\nu_e \ll \Omega_e$, $\nu_i \gg \Omega_i$	2	*Rogister and D'Angelo* [1970]
GDI ion inertial mode	Topside F-region near 450 km	$D_e/Dt \ll \nu_e$, $\nu_\alpha \ll \Omega_\alpha$, $k_\parallel = 0$	3	*Ossakow et al.* [1978]
CCI/GDI Pedersen mode	Main F-region	$D_\alpha/Dt \ll \nu_\alpha$, $\nu_\alpha \ll \Omega_\alpha$	1	*Keskinen and Ossakow* [1982]
CCI/GDI Pedersen mode	Main F-region	$D_\alpha/Dt \ll \nu_\alpha$, $\nu_\alpha \ll \Omega_\alpha$, $T_\alpha = 0$	1	*Ossakow and Chaturvedi* [1979]
GDI Pedersen and Hall modes	Lower ionosphere 90–300 km	$D_\alpha/Dt \ll \nu_\alpha$, $k_\parallel = 0$, $T_\alpha = 0$	1	*Makarevich* [2014]
FBI/GDI/CCI	Lower ionosphere 95–300 km		4	*Dimant and Oppenheim* [2011b] *Makarevich* [2016a, b]

Table 1.2 summarizes theoretical studies that used fluid approach to describe the non-isothermal case. One can see from Table 1.2 that, unlike isothermal case, nonisothermal fluid theories have predominantly focused on the E-region, with only a few attempting to describe both ITI and ETI within the same formalism, and with no nonisothermal theory currently being available that would describe the entire lower ionosphere. In particular, effects of the plasma density gradients and the associated instabilities that are also operational in the F-region have not been considered in the context of the nonisothermal formalism. This potentially represents a promising avenue for future theoretical efforts.

In addition to the linear fluid approach, nonlinear theories and numerical simulations have also been used to advance our understanding of irregularity formation mechanisms from a theoretical point of view. Nonlinear effects using 1-D [*Litt et al.*, 2016] and 2D [*Hassan et al.*, 2015] fluid simulations have been recently investigated, where the previously ignored [*Fejer et al.*, 1975] ion viscosity and electron inertia terms were added. The ion viscosity term has been shown to stabilize the large wavelengths around 3-m scale sizes in the vertical direction, and 1-m in the horizontal direction, which verified the cascade of

Table 1.2. Development of nonisothermal linear fluid theory, with major instability cases, their altitudinal domains, approximations used, and references.

Mode	Domain	Approximations	Reference
ETI	Upper D–lower E region 75–105 km	$D_i/Dt \ll \nu_i$, $\nu_e \ll \Omega_e$, $\nu_i \gg \Omega_i$	*Dimant and Sudan* [1997]
ETI	Main E region near 110 km	$D_i/Dt \ll \nu_i$, $\nu_e \ll \Omega_e$, $\nu_i \gg \Omega_i$	*Kissack et al.* [1997]
ETI	Main E region near 110 km	$D_i/Dt \ll \nu_i$, $\nu_e \ll \Omega_e$, $\nu_i \gg \Omega_i$, $k_\parallel = 0$	*St.-Maurice and Kissack* [2000]
ITI driven by neutral wind	E-region 75-125 km	$D_i/Dt \ll \nu_i$	*Kagan and Kelley* [2000]
ITI driven by electric field and ETI	Main E-region	$D_e/Dt \ll \nu_e$, $\nu_e \ll \Omega_e$, $\nu_i \gg \Omega_i$, $k_\parallel = 0$, $T_{i0} \approx T_n$, $T_e \approx T_{e0} \geq T_n$	*Dimant and Oppenheim* [2004]
ETI	Lower E-region 90–110 km	$D_i/Dt \ll \nu_i$, $k_\perp = const$	*Kagan and St.-Maurice* [2004]
ETI	Main E-region near 110 km	$D_i/Dt \ll \nu_i$, $\nu_e \ll \Omega_e$, $\nu_i \gg \Omega_i$, $\delta T_i = 0$	*Kissack et al.* [2008a, b]
ETI and ITI	Main E-region 90–125 km	$D_i/Dt \ll \nu_i$, $\nu_e \ll \Omega_e$, $\nu_i \gg \Omega_i$	*St.-Maurice and Chau* [2016]

energy from large to small structures [*Sudan et al.*, 1973].

Massively parallel supercomputers allowed a simulation of the fully kinetic dynamics of electrons and ions as they respond to a driving electric field and their own self-generated electric field using particle-in-cell (PIC) method in 2D [*Oppenheim et al.*, 2008] and 3D [*Oppenheim and Dimant*, 2013] cases. The set of simulations showed the generation of short-wavelength (1–5 m) modes from noise and the development of longer-wavelength modes through the inverse cascade mechanism in the nonlinear mode coupling. In addition to 2D turbulence effects, the 3D simulation showed the development of small parallel electric fields that heat the electrons at a level that is sufficient to explain the anomalous electron heating (AEH) in the auroral region.

In a theoretical study presented in Chapter 2 of this body of work, the isothermal general dispersion relation is used that has been recently derived by *Makarevich* [2016a]. That study used a general formalism that allowed a derivation of the general dispersion relation that combined the FBI, GDI, and CCI. In this part of the theory review, the same formalism will be followed to show the most important steps in the derivation of the general dispersion

relation and of its limiting case of the FBI/GDI in the E-region for nearly field-aligned irregularities. This is the limiting case that is most important for interpreting observations presented in Chapters 4 and 5 of this thesis.

In general, a dispersion relation describes the effect of dispersion in a medium on the properties of a wave traveling within that medium. It is an equation that relates a complex wave frequency ω to the wave vector $\mathbf{k}$. A dispersion relation can be derived by linearization of continuity and momentum equations, where the perturbations in plasma density and electric potential assumed to have plane wave solution, meaning that these physical quantities can be represented as a sum of the background quantity X_0 and a small perturbed quantity δX. A perturbation represents harmonically varying with space (defined by the positioning vector $\mathbf{r}$) and time t quantity, such as its sum with the background quantity takes the form

$$X = X_0 + \delta X e^{i(\mathbf{k}\cdot\mathbf{r} - \omega t)} = X_0 + \delta X e^{i\mathbf{k}\cdot\mathbf{r}} e^{-it\omega_r} e^{\gamma t}. \tag{1.4}$$

In case of $\gamma < 0$ the perturbed part of the physical wave is damped, and when $\gamma > 0$ the frequency of the perturbation is exponentially growing. In other words, the growth rate γ determines whether the instability is operational or not. Thus, the real part of the wave frequency ω_r determines the amplitude of the time-varying oscillations, and the growth rate γ defines if those oscillations are growing with time or being damped.

A general dispersion relation can be derived by combining Equations (1.1) and (1.2) in Fourier space through the density and electric potential perturbations and assuming the plane wave representation of the perturbed density and electric field. In addition to the quasineutrality, local approximation, and the isothermality, another assumption used for the derivation of the general dispersion relation is the domination of the plasma motion by the convection electric field, which implies that the neutral velocity is much smaller than those of the plasma species $U \ll V_\alpha$. Detailed derivation of the general dispersion relation is presented in *Makarevich* [2016a], with the final form being as follows

$$(H_i - H_e)\omega = (H_i \mathbf{V}_{e0} - H_e \mathbf{V}_{i0}) \cdot \mathbf{k} + (C_i - C_e) H_e H_i. \tag{1.5}$$

In this equation, the following notations are used

$$H_\alpha \equiv S_\alpha F_\alpha + D_\alpha^{-1} F_\parallel, \qquad S_\alpha \equiv (1 + D_\alpha^2)^{-1}, \qquad F_\alpha \equiv ik_\perp^2 D_\alpha + \mathbf{G}\cdot\mathbf{k}_\perp D_\alpha + \mathbf{G}\cdot\mathbf{k}\times\hat{\mathbf{b}},$$
$$D_\alpha = -i\Omega_\alpha^{-1}(\omega - \mathbf{k}\cdot\mathbf{V}_{\alpha 0}) + \frac{\nu_\alpha}{\Omega_\alpha}, \qquad F_\parallel \equiv ik_\parallel^2 + \mathbf{G}\cdot\mathbf{k}_\parallel,$$
$$\mathbf{G} \equiv \frac{\nabla n}{n}, \qquad \hat{\mathbf{b}} \equiv \frac{\mathbf{B}}{B}, \qquad C_\alpha \equiv \frac{T_\alpha}{m_\alpha \Omega_\alpha}. \tag{1.6}$$

The general dispersion relation (1.5) describes a configuration with arbitrary altitude, geometry, wave vector, and gradient. Various limiting cases of interest, such as the FBI and GDI dispersion relations, can be recovered from the general dispersion relation by applying further approximations that are suitable for a particular domain of the interest.

The general dispersion relation (1.5) can be rewritten into alternative form

$$(F_i + S_i^{-1} D_i^{-1} F_\parallel)(\omega' - \mathbf{V}_d\cdot\mathbf{k}) - [S_i^{-1}\omega' + C(F_i + S_i^{-1} D_i^{-1} F_\parallel)](F_e + D_e^{-1} F_\parallel) = 0, \tag{1.7}$$

where the wave frequency ω was transformed into ion frame with $\omega' \equiv \omega - \mathbf{V}_{i0}\cdot\mathbf{k}$, the electron inertia was neglected $S_e^{-1} \approx 1$, and C relates to the standard isothermal ion-acoustic speed C_s through $C \equiv C_i - C_e = (T_i + T_e)/|e|B = C_s^2/\Omega_i$.

Since the main focus of the current body of work is on the E-region, we further consider the limiting case of the general dispersion relation suitable for the E-region domain. The first approximation that is further applied refers to the nearly field-perpendicular propagation of the waves, or the generation of the irregularities in the narrow cone centered at the plane perpendicular to the magnetic field. Mathematically, this approximation can be expressed in terms of the wave components perpendicular and parallel to the magnetic field, $k_\parallel/k_\perp \ll 1$, which leads to the approximation $S_i^{-1} D_i^{-1} F_\parallel \ll F_i$. Second, in the E-region electrons are magnetized, and therefore their gyrofrequency is much greater than the collisional frequency, $\nu_e/\Omega_e \ll 1$. A third approximation is applicable to the high-latitude ionosphere, where the parallel component of the gradient is small as compared to the perpendicular component, $G_\parallel \ll G_\perp$. The dispersion relation in this limiting case is

$$(D_i - iaD_i + ib)(\omega' - \mathbf{V}_d\cdot\mathbf{k}) + [\omega'(1 + D_i^2) + iCk_\perp^2(D_i - iaD_i + ib)](\hat{\psi} r_i^{-1} - ib) = 0, \tag{1.8}$$

where a and b are the gradient terms

$$a \equiv \frac{\mathbf{G}\cdot\mathbf{k}_\perp}{k_\perp^2}, \qquad b \equiv \frac{-\mathbf{G}\cdot\mathbf{k}\times\hat{\mathbf{b}}}{k_\perp^2}. \tag{1.9}$$

In Equation (1.8), quantity $\hat{\psi}$ is the standard anisotropy factor [*Sahr and Fejer*, 1996]

$$\hat{\psi} = -\frac{\nu_e \nu_i}{\Omega_e \Omega_i}\left(1 + \frac{\Omega_e^2}{\nu_e^2}\tan^2\alpha\right), \tag{1.10}$$

that depends on the angle between the wave vector $\mathbf{k}$ and a plane perpendicular to the magnetic field, called the aspect angle $\alpha = \tan^{-1} k_\parallel / k_\perp$. Equation (1.8) is a cubic equation, and can be solved numerically in D_i, and hence in ω' [*Makarevich*, 2016b].

Further approximation to Equation (1.8) is possible using $-iaD_i \ll D_i$, $ib \ll D_i$, and $1 + D_i^2 \approx D_i^2$ [*Makarevich*, 2016b], which leads to the standard quadratic form of the nearly-field-aligned FBI/GDI dispersion relation for the E-region derived by *Fejer et al.* [1984]

$$\omega' - \mathbf{V}_d \cdot \mathbf{k} + (\omega' D_i + iCk_\perp^2)(\hat{\psi} r_i^{-1} - ib) = 0. \tag{1.11}$$

Representing complex wave frequency $\omega' = \omega'_r + i\gamma$, the oscillation frequency and the growth rate are

$$\omega'_r = \frac{\mathbf{V}_d \cdot \mathbf{k}}{1 + \hat{\psi}}, \qquad \gamma_{\mathrm{FBI/GDI}} = \frac{1}{1 + \hat{\psi}}\left[\frac{\hat{\psi}}{\nu_i}\left(\omega_r'^2 - C_s^2 k_\perp^2\right) + \frac{b\omega'_r \nu_i}{\Omega_i}\right]. \tag{1.12}$$

Importantly, the presence of the gradient term b affects only the growth rate γ, but not the oscillation frequency ω'_r, and therefore it does not affect the phase velocity of the irregularities $\mathbf{V}_{ph} = \omega'_r / k\hat{\mathbf{k}}$. The instability is operational when $\gamma > 0$. Figure 1.6 demonstrates the regions in the $\mathbf{k}$ space where the plasma is unstable. In the gradient-free case ($b = 0$), the instability is operational when $V_d \cos\theta > C_s(1 + \hat{\psi})$, where θ is the flow angle between the perpendicular component of the wave vector $\mathbf{k}_\perp$ and the plasma drift $\mathbf{V}_d$ (shown in dim red and white in Figure 1.6, respectively).

In the plane perpendicular to the magnetic field, the waves are unstable in the region defined by the critical flow angle $\theta_0 = C_s(1 + \psi)/V_d$, whereas in the plane parallel to the magnetic field the instability region is defined by a very small critical aspect angle α_0, which is illustrated schematically in Figure 1.6. For a numerically

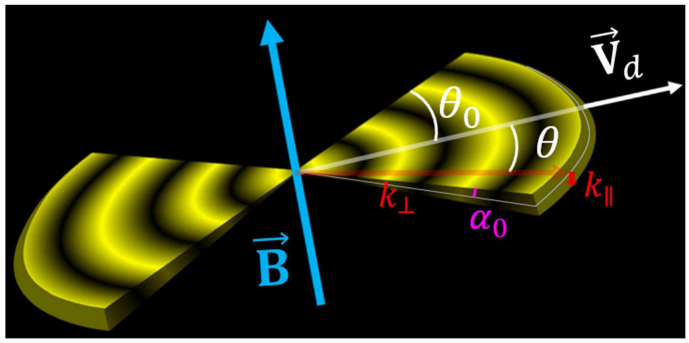

Figure 1.6. Critical flow and aspect angles for linearly unstable waves.

derived distribution of the growth rate and phase velocity in $k_\perp-$space, see Figure 2.5a and 2.5e.

In the presence of the gradient in the electron density $\mathbf{G}$, the threshold velocity is modified [*Farley and Fejer*, 1975]

$$V_d \cos\theta = C_s \sqrt{1 + \frac{b'^2}{C_s^2}} + b', \qquad b' = -\frac{(\mathbf{G} \cdot \hat{\mathbf{k}}_\perp \times \hat{\mathbf{b}})\nu_i \Omega_e}{k_\perp^2 \nu_e}, \tag{1.13}$$

and can be increased or decreased, depending on $\mathbf{G}$ orientation and, through that, sign of b'.

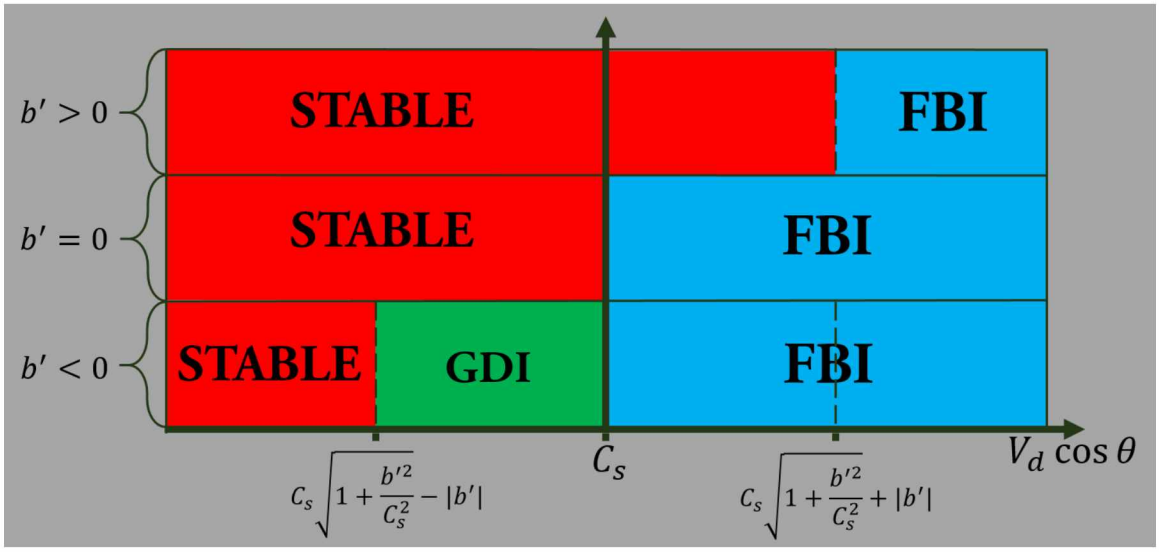

Figure 1.7. *E*-region instability regimes for different threshold velocity values of the convection component, depending on the density gradient orientation relative to the magnetic field and the wave vector.

It is also important to emphasize that Equation (1.12) contains both FBI and GDI regimes of the plasma instability. Figure 1.7 illustrates schematically the three regions where the plasma waves are stable, unstable to GDI, and unstable to FBI, shown in red, green, and blue respectively. In the gradient-free case $b' = 0$, the pure FBI instability is operational, when the condition $V_d \cos\theta > C_s$ is met, and no unstable waves are expected when this condition is not met (shown as blue and red areas in the middle section of Figure 1.7). The b' term contains the information about the magnitude and the orientation of the gradient $\mathbf{G}$ relative to the wave vector and the magnetic field. In case when $b' > 0$, the threshold is increased, therefore no waves are expected when $V_d \cos\theta < C_s\sqrt{1 + b'^2/C_s^2} + |b'|$ (red area in the top section of Figure 1.7). When the gradient $\mathbf{G}$ is oriented in a way

that makes $b' < 0$, the instability is operational in the GDI regime when the condition $C_s\sqrt{1+b'^2/C_s^2} - |b'| < V_d\cos\theta < C_s$ is met, and in a pure FBI regime when $V_d\cos\theta > C_s$ (green and blue areas in the bottom section of Figure 1.7). Figure 1.7 thus illustrates that unfavorable gradient orientations (a case shown in the top section of Figure 1.7) make plasma more stable by increasing the FBI threshold, while favorable gradient orientations (bottom section) make plasma more unstable through GDI by effectively decreasing the FBI threshold.

This section introduced the main formalism in the fluid theory of the plasma irregularity formation, summarized the previous efforts in the unification of the theory, and highlighted some recent developments. In the following section, a review of observations of the E-region irregularities is presented, focusing on the aspects closely related to the main body of the thesis: the aspect angle dependencies of irregularity characteristics, radar observations in the polar cap, and the fundamental dependence of the E-region phase velocity on the plasma convection.

1.3 Review of the Observations of the *E*-Region Irregularities

The history of the ionospheric irregularity observations has started from detection of echoes from the E-region heights by *Eckersley* [1937] and *Harang and Stoffregen* [1938]. A detailed chronology and development of the experimental work that followed can be found in numerous review papers [*Fejer*, 1979; *Fejer and Kelley*, 1980; *Hanuise*, 1983; *Farley*, 1985; *Fejer and Providakes*, 1987; *Haldoupis*, 1989; *Sahr and Fejer*, 1996; *Makarevich et al.*, 2009] and theses [*Sahr*, 1990; *Makarevitch*, 2003; *Carter*, 2011]. In this section, a review of observations most relevant to this body of work is presented that would add greater depth to the discussions in Chapters 2, 4, and 5. More focused reviews on the relevant literature are also presented in Sections 2.2, 4.2, and 5.2.

1.3.1 Aspect Angle Control

From the early observations of the E-region irregularities, it has been noticed that the strongest scatter is observed when the bisector of the incident and scattered radio wave reaches the perpendicularity with the Earth's magnetic field. Just as surface water waves are highly aligned with the Earth's gravity, the E-region waves are aligned with the magnetic field [*Sahr and Fejer*, 1996], i.e. they have their phase fronts nearly parallel to $\mathbf{B}$ and travel in the plane perpendicular to $\mathbf{B}$. This property arises due to the fact that the anisotropy factor (see Equation (1.10)) increases as a tangent squared of the aspect angle α. In the directions departing from perpendicularity, the plasma waves are strongly damped by the diffusion [*Haldoupis*, 1989]. For this reason, the rapid decrease of echo strength with increasing aspect angle has been observed by very high frequency (VHF) [*Ogawa et al.*, 1980; *Schlegel and Moorcroft*, 1989; *Foster et al.*, 1992; *Kustov et al.*, 1994b] and high frequency (HF) [*Koustov et al.*, 2001; *Makarevitch et al.*, 2001, 2002b, a] radars. The behaviour of the phase velocity at different aspect angles has also been investigated using VHF [*Ogawa et al.*, 1980; *Nielsen*, 1986; *Ogawa et al.*, 1982; *Kustov et al.*, 1994b; *Makarevich et al.*, 2006, 2007] and HF [*Makarevitch et al.*, 2002b, 2004] radars.

The rate of the decrease of the phase velocity with the increasing aspect angle was shown to differ between small ($\theta < \theta_0$) and large ($\theta > \theta_0$) flow angles [*Makarevich et al.*, 2007]. This difference appears from the contribution of the ion drift term in the expression of the phase velocity in the reference frame of the neutrals

$$V_{ph} = \frac{V_d \cos\theta}{1+\hat{\Psi}} + \hat{\mathbf{k}} \cdot \mathbf{V}_{i0}. \tag{1.14}$$

It was found that, in case of the large flow angles ($\theta > \theta_0$), the first term in the Equation (1.14) is small, and the phase velocity is dictated by the contribution of the ion flow, which is aspect angle independent, and no variation with changing aspect angle is observed [*Makarevitch et al.*, 2002b; *Makarevich et al.*, 2007].

At small flow angles ($\theta < \theta_0$), the effects predicted by the linear theory were found to be weaker than previously expected, and, instead, the *anomalous collisions* [*Sudan*, 1983], an extremely large electron-neutral collision frequency, were found to play an important role [*Ogawa et al.*, 1980, 1982; *Nielsen*, 1986; *Schlegel and Moorcroft*, 1989; *Foster et al.*, 1992; *Kustov et al.*, 1994b; *Makarevitch et al.*, 2002b]. According to the theory of anomalous collisions, the particle-wave interaction increases the collision frequency in the expression for the anisotropy parameter, making it large enough to saturate the phase velocity at C_s. Importantly, according to this theory, the anomalous collision frequency is also a decreasing function of the flow angle, because the phase velocity V_{ph} is smaller at nonzero flow angles. Observations of the aspect angle effects at the small flow angles were consistent with this idea [*Ogawa et al.*, 1980, 1982; *Nielsen*, 1986; *Schlegel and Moorcroft*, 1989; *Kustov et al.*, 1994b; *Makarevitch et al.*, 2002b].

The above discussed dependence of the phase velocity on the aspect angle is particularly important to this body of work for two main reasons. First, in the theoretical study presented in Chapter 2, the previously unreported effects of the parallel electric field on the above dependence are considered. Second, in the first experimental study presented in Chapter 4, it is shown that the aspect angle control of the phase velocity of the ionospheric irregularities is one of the primary controlling factors of the irregularity velocity and its dependence on the plasma density conditions and altitude in the southern polar cap.

1.3.2 Experimental Evidence for the Destabilizing Density Gradients

As was discussed in Section 1.2, the linear fluid theory predicts the effects of the electron density gradients on the FBI threshold [*Farley and Fejer*, 1975] that can be increased or reduced, depending if the gradient has stabilizing or destabilizing orientation. There is no doubt that strong enough electron density gradients can be present in the ionosphere, particularly during strong sporadic E [*Haldoupis et al.*, 2005]. Multiple experiments have been conducted to estimate the scale length of the plasma gradients, e.g. the high-latitude

study with the European Incoherent Scatter (EISCAT) radar facility estimated the scale length of vertical gradients in the E-region at times of particle precipitation to range between 4 and 7 km [*Haldoupis et al.*, 2000]. In another study on that issue but at mid-latitudes, the gradient scale length was estimated to be 1 km [*Haldoupis et al.*, 2005]. However, the destabilizing or stabilizing effect of the gradients on the FBI has not been established conclusively, due to the difficulty of the simultaneous measurements of the Doppler velocity of the FBI waves and the scale of the driving plasma density gradients. Below, experimental studies are reviewed that presented indirect evidence in support for the effects of the plasma gradients on the FBI threshold, together with the studies that argued against those effects. The evidence for the significant role of gradients can be categorized as (1) observed phase velocities being lower or higher than nominal FBI threshold, (2) observed diurnal variations in spectral width, and (3) observed velocity dependency on the radar frequency.

The first group of observations lend an indirect support to the destabilizing density gradients through observations of the FBI waves with the threshold velocity lower than expected [*Prakash et al.*, 1971], in agreement with the idea illustrated in Figure 1.7. Similarly, observations of irregularity velocities greatly exceeding the expected FBI threshold velocity value are consistent with the notion of stabilizing density gradients [*Milan and Lester*, 2001]. Moreover, observations of the waves with the Doppler shift of opposite sign to that expected from the direction of the electric field also indirectly supports the idea that the growth of these irregularities critically depends on the orientation of the density gradients with respect to the radar look-direction [*Milan and Lester*, 2001].

The second piece of evidence comes from spectral measurements of FBI waves. A regular FBI power spectrum has a narrow peak at C_s, because FBI is operational only when the marginal condition $V_d \cos\theta > C_s$ is met. However, it is frequently observed to be broader during the night than during the day, which indirectly supports the notion that during the night the gradients are much sharper and more variable than during the day. One expects therefore the threshold phase velocity to vary over some range (even when the nominal C_s is constant) diffusing the spectra [*Farley and Fejer*, 1975].

The third piece of evidence is associated with the fact that the gradient term b' in Equation (1.13) is frequency-dependent, since it directly depends on the wave number k. Therefore, the irregularity phase velocity is expected to decrease with a decreasing radar frequency, due to a reduction in the threshold velocity. Two multi-frequency radar experiments in the equatorial electrojet supported this idea. The first experiment used three radar

frequencies in the range of 16–150 MHz and confirmed a decrease of the phase velocity by a factor of 10% with the radar frequency decrease by the factor of 3 [*Balsley and Farley*, 1971]. The second multi-frequency experiment also confirmed a reduction of the phase velocity with a decreasing frequency in the range of 30–50 MHz, indicating the presence of the destabilizing plasma density gradients with 6-km scales [*Hanuise and Crochet*, 1981].

In the auroral E-region, several studies predicted the variation of the phase velocity with radar frequency for a particular gradient scale [*Farley and Fejer*, 1975; *Hamza and St.-Maurice*, 1993]. The results of the multi-frequency HF observations by *Makarevitch et al.* [2002b] reasonably agreed with the theoretical prediction in the spread of the Doppler velocity at a particular gradient scale length of ~10 km for 5 different wavelengths, again, indirectly supporting the above idea.

There are, however, several experimental studies that argue against the theoretical idea of the threshold velocity modification by the density gradients. Thus, the FBI waves with no expected gradient effects were simultaneously observed at two VHF frequencies of 50 and 144 MHz from sporadic E, where steep perpendicular density gradients are believed to be present [*Haldoupis et al.*, 2005]. Also, observations of the meteor-induced backscatter echoes were supposed to have a very sharp density gradients showed the presence of GDI echoes and a few pure FBI echoes, but no presence of the FBI echoes with the modified threshold velocity [*Haldoupis et al.*, 2005]. One more experimental study with the orientation of the high-latitude HF radar along the flow direction, where the effects from both horizontal and vertical gradients are supposed to be the strongest, showed much less deviation from the threshold velocity than theoretically predicted [*Lacroix and Moorcroft*, 2001].

The effects of the electron density gradients on the FBI threshold discussed above are particularly important to this body of work. This is because in Chapter 5 of this body of work additional observational evidence is presented in support of the idea of the destabilizing density gradients affecting the FBI threshold value.

1.3.3 Observations of the Radar Aurora in the Polar Cap

Since E-region irregularities are magnetic-field-aligned, the orientation of the Earth's magnetic field is an important factor for the location of the irregularities. In order for a radar to receive backscatter, the radar signal needs to reach orthogonality with the magnetic field in the E-region. The orthogonality condition for HF radars can be easily reached in the high-latitude zone, because the magnetic field has a slight inclination in this region, which

cannot be said about the polar cap region, where the magnetic field is almost vertical. For this reason, the observation of the E-region irregularities in the polar cap has been far less numerous than in the auroral zone [*Hanuise*, 1983].

The early radar observations [*Primdahl et al.*, 1974; *Tsunoda et al.*, 1976; *D'Angelo and Olesen*, 1975; *Iversen et al.*, 1975; *Olesen et al.*, 1975] and rocket measurements [*Bahsen et al.*, 1978] have detected the radar aurora in the polar cap region and showed the presence of FBI waves when the electric field exceeded the threshold value.

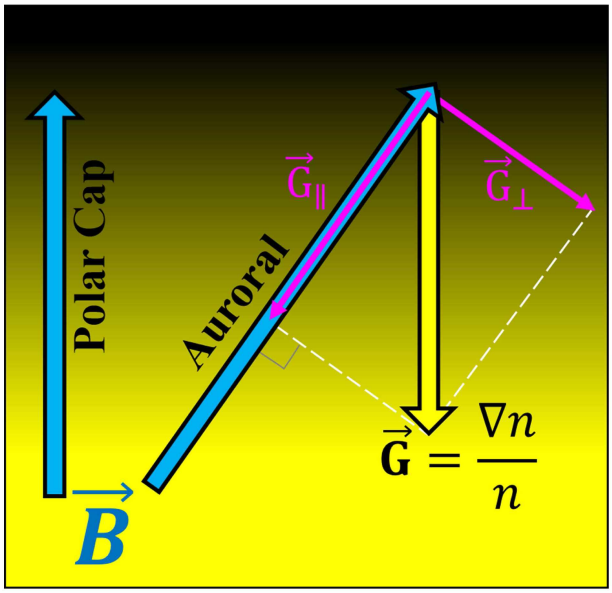

Figure 1.8. Vertical density gradients for polar and auroral ionosphere.

The gradient term b' in Equation (1.13) can modify the FBI threshold only when the gradient vector **G** has a significant component perpendicular to the magnetic field. It has been proposed that the density gradients in the polar and auroral ionosphere are vertical and are mostly associated with particle precipitation [*Hanuise*, 1983]. Figure 1.8 shows the decomposition of the density gradient **G** that is assumed to be purely vertical (yellow arrow) into two components (shown in pink), parallel and perpendicular to the magnetic field **B** (light blue arrows), that itself has a different orientation depending on the latitudinal zone. In the polar cap, the magnetic field is almost vertical and in the auroral zone the magnetic field is inclined from the vertical direction (Figure 1.8). Therefore, only in the auroral zone is there a significant component of the density gradient that is perpendicular to the magnetic field and no such component is present in the polar cap, Figure 1.8. According to this geometry, no GDI echoes are expected to be present in the polar cap, due to the absence of $\mathbf{G}_{\perp}$. However, previous studies in the northern polar cap reported significant presence of low-velocity HF [*Carter et al.*, 2012] and VHF [*Kustov et al.*, 1994a] GDI-produced echoes, in apparent contrast with the above theoretical expectations.

In order to further explore the puzzling presence of the GDI waves in the polar cap

E-region, the plasma-physical characteristics of the plasma waves simultaneously observed by two HF radars in the southern polar cap are investigated in Chapter 4.

1.3.4 Fundamental Relationship Between the *E*-Region Irregularity Phase Velocity and the Plasma Convection

The phase velocity of the E-region waves produced in the linear regime is directly related to the component of the plasma drift velocity $V_d \cos\theta$, Equation (1.14). This fundamental dependence was investigated in several experimental studies [*Nielsen and Schlegel*, 1983; *Koustov et al.*, 2005; *Makarevitch et al.*, 2004; *Carter et al.*, 2012; *Makarevich et al.*, 2015], where the information about the phase velocity of the E-region irregularities were obtained using VHF [*Nielsen and Schlegel*, 1983] and HF [*Koustov et al.*, 2005; *Makarevitch et al.*, 2004; *Carter et al.*, 2012; *Makarevich et al.*, 2015] radars.

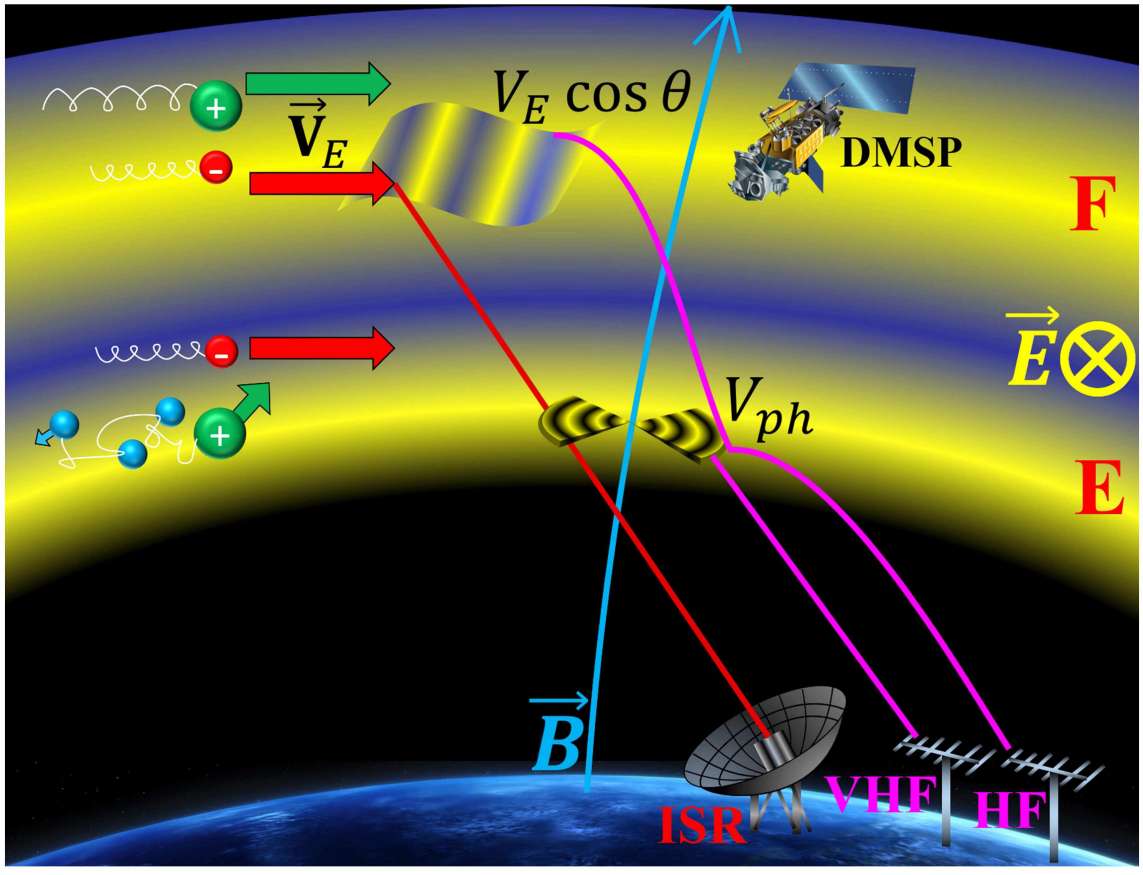

Figure 1.9. E- and F-region observations using coherent and incoherent scatter radars and low-Earth-orbit satellites.

The component of the drift velocity was estimated from the F-region altitudes, where the ions and electrons both flow with the $\mathbf{E}\times\mathbf{B}$ drift, using incoherent scatter radar [*Nielsen and Schlegel*, 1983] or satellite [*Koustov et al.*, 2005] measurements of the ion drift, or HF measurements of the F-region velocity obtained with a single HF radar [*Makarevitch et al.*, 2004; *Carter et al.*, 2012] or a network of HF radars [*Makarevich et al.*, 2015].

Figure 1.9 demonstrates different types of observations used for simultaneous measurements of the E-region phase velocity of the irregularities and the plasma drift in the F-region. Also shown are the background motion of the electrons and ions, where in the F-region both species are magnetized and moving with the same velocity of the plasma flow $\mathbf{V}_E$ (red and green vectors). In the E-region, electrons move with the same velocity as in the F-region (red vector), but the motion of the ions is dictated by the collisions with neutral particles (green vector). Therefore, the background velocity of electrons in the E-region can be estimated from the motion of the ion-acoustic waves in the F-region, that can be detected by an incoherent scatter radar (ISR). In Figure 1.9, the ISR (shown as a dish-based system) is probing the plasma flow in the F-region, thus also making an estimate of the electron flow in the E-region. One example of such measurement of the plasma drift velocity in the E-region from the motion of the ion-acoustic waves was made by *Nielsen and Schlegel* [1983] using the EISCAT tri-static radar facility. The component of the plasma flow velocity in the F-region can also be measured by coherent-scatter radars that detect GDI waves in the F-region that are stationary in the frame of the plasma and move with the large-scale plasma flow [*Carter et al.*, 2012; *Makarevitch et al.*, 2004; *Makarevich et al.*, 2015]. The direct measurement of the component of the plasma flow velocity in the F-region by a HF radar is shown in pink in Figure 1.9. The velocity of the E-region irregularities can be also measured using HF [*Makarevitch et al.*, 2004; *Koustov et al.*, 2005; *Carter et al.*, 2012; *Makarevich et al.*, 2015] and VHF [*Nielsen and Schlegel*, 1983, 1985; *Uspensky et al.*, 2003, 2004; *Makarevich et al.*, 2006, 2007] radars, also shown in pink in Figure 1.9. Comparing the results for HF and VHF radars, it is important to take into account the role of refraction for HF signals caused by the background electron density, which "bends" the radar signal, thus helping to achieve orthogonality with the magnetic field (straight VHF radar signal path versus bent HF signal path in Figure 1.9).

Some of the previous studies showed an agreement between the plasma drift component $V_E\cos\theta$ and the line-of-sight V_{ph} for small velocities (< 700 m/s) [*Nielsen and Schlegel*, 1983], however, other studies showed a depression of the irregularity velocity [*Makarevitch*

et al., 2004; *Koustov et al.*, 2005; *Carter et al.*, 2012; *Makarevich et al.*, 2015], possibly due to more frequent collisions and aspect angle attenuation [*Carter et al.*, 2012; *Makarevich et al.*, 2015], ion drift contribution [*Makarevitch et al.*, 2004], and the presence of the slow echoes from the bottom of the electrojet layer [*Koustov et al.*, 2005].

In the experimental study presented in Chapter 5, we build on this previous effort by analyzing E-region observations using a dual radar setup in the latitudinal domain where high-quality convection measurements are available from the entire SuperDARN array in the southern hemisphere.

1.4 Motivation and Objectives

A particular focus of this work, the Farley-Buneman instability or FBI, may seem at first to be a very narrow topic. Despite this, FBI has in fact much more ubiquitous nature and is not limited to the E-region of the ionosphere. For instance, FBI can be created and observed in the laboratory plasma using a cylindrical chamber with the ionized Argon gas and the uniform magnetic field produced by a pair of Helmholtz coils [*John and Saxena*, 1975]. Moreover, recent studies have shown that FBI can be generated in the collisional plasma of the solar chromosphere [*Fontenla*, 2005; *Fontenla et al.*, 2008; *Gogoberidze et al.*, 2009], where the electrons are strongly magnetized but protons are collisional in the presence of the neutral H atoms and the upward propagating magnetohydrodynamic (MHD) waves. Several studies have even shown that FBI waves in the chromosphere contribute to the heating of the solar coronae through the production of the anomalous resistivity and wave energy dissipation [*Fontenla*, 2005; *Fontenla et al.*, 2008; *Gogoberidze et al.*, 2009]. Therefore, FBI can be closely related to the grand challenge in the heliophysics and astrophysics, i.e. the understanding of the heating processes in the coronae of the Sun and other cool stars with partially ionized chromosphere. In addition, the FBI-produced small-scale irregularities were proposed to be suited for the remote sensing of the chromosphere at meter wavelengths [*Gogoberidze et al.*, 2009], thus opening new possibilities for radio science and studies of the Sun and the solar wind. One practical aspect of this research is *Space Weather*, which is the term used to describe changing conditions in the near-Earth plasma environment due to the disturbances originating from the Sun, most notably geomagnetic storms.

During the largest geomagnetic storm on record, the Carrington event in 1859, the coronal mass ejection hit the Earth's magnetosphere and caused the failure of the telegraph systems all over Europe and North America [*Tsurutani et al.*, 2003]. Nowadays, society has more to lose when (n.b. not if) an event like this happens again. Powerful ionospheric electrojets caused by the highly disturbed magnetic field induce geoelectric fields in the lithosphere and through the voltage differentials damage the transformers of the power grid and can cause blackouts. Energetic particles can directly damage satellites and cause their failure, whereas the increased density in the thermosphere can change the orbit of the satellite due to the increased drag. Radio and satellite communication can also fail due to the strong scintillation in the ionosphere, leaving aviation and military operations without communication and navigation. The economical impact from geomagnetic storms can be tremendous, for example, the event similar to Carrington would cost 0.6–2.6 trillion dollars

to the U.S. alone [*Homeier and Wei*, 2013]. Therefore, the fundamental understanding of the processes in the near-Earth plasmas has a direct impact on the human society and its safety.

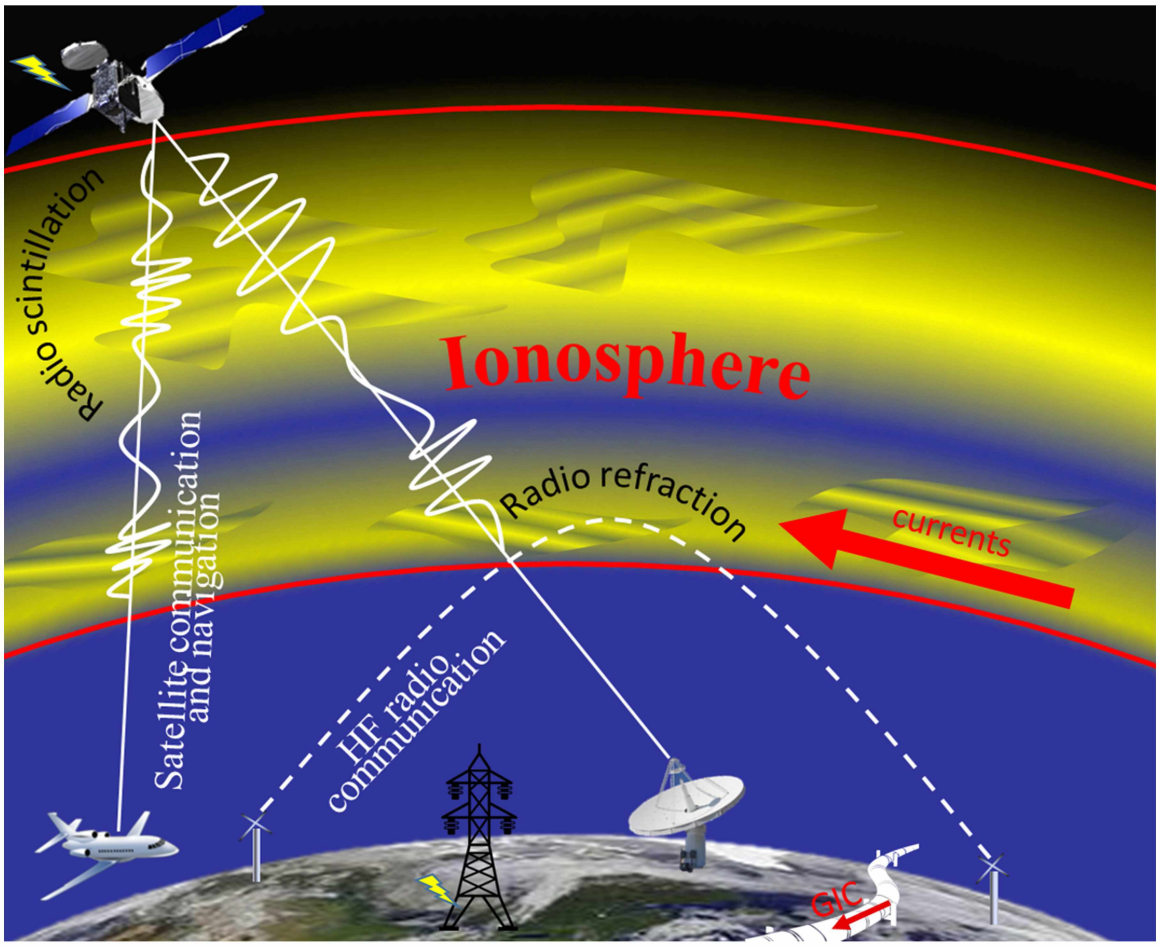

Figure 1.10. Ionosphere and the Space Weather impacts.

The impacts of the Space Weather are evident even during relatively quiet geomagnetic times. Figure 1.10 illustrates the Space Weather impacts on the technological infrastructure. Long-distance radio communication and radar surveillance use the ionosphere as a medium to refract a signal to the distant stations and targets beyond the horizon. Plasma irregularities can cause the fluctuation or scintillation of the radio signal when it passes through the ionosphere. For example, the fading of Global Navigation Satellite System (GNSS) signals due to ionospheric scintillation is a major concern for the future intelligent air transportation system that will fully rely on the GNSS to navigate and land aircraft

[*Pullen et al.*, 2009; *Seo et al.*, 2011]. Unfortunately, ionospheric scintillation and plasma irregularities driven by FBI and GDI are very difficult phenomena to predict or model on the global scale. The high-latitude region is a particularly problematic zone to model the scintillation [*Deshpande et al.*, 2014].

The main motivation for this research is to advance understanding of the irregularity formation in the Earth's ionosphere and improve the ability to predict irregularity occurrence and propagation. Understanding the origins and enabling better prediction of the plasma wave characteristics will potentially improve our ability to mitigate the adverse effects of scintillation on satellite navigation and radio communication during various Space Weather conditions.

The more specific objectives of this thesis can be formulated as follows:

(1) Theoretically analyze the general dispersion relation with the presence of the parallel electric field.

(2) Determine if parallel electric field can result in experimentally measurable differences between characteristics of FBI waves with parallel propagation components of opposite polarity.

(3) Investigate small-scale irregularity production in the polar E-region and the factors that control the irregularity phase velocity.

(4) Study the specifics of HF radar signal propagation in the polar cap.

(5) Statistically analyze occurrence of high-latitude E-region irregularities.

(6) Evaluate the extent of the control of the irregularity characteristics by the F-region plasma convection.

The outline of the thesis is as follows. Chapter 2 presents a theoretical study of symmetry properties of the FBI dispersion relation with respect to a reversal of the wave propagation component parallel and perpendicular to the magnetic field. The same results were also presented in a recent journal article [*Forsythe and Makarevich*, 2016]. In Chapter 3, the primary instrument used in the observational part of this research, the Super Dual Auroral Radar Network (SuperDARN) is introduced, as well as the instruments and computational models that complemented this research, including the Defense Meteorological Satellite Program (DMSP) satellites, the International Reference Ionosphere model (IRI), and the Mass Spectrometer and Incoherent Scatter model (MSIS). In Chapter 4, the characteristics of the FBI waves in the southern polar cap are investigated using a dual radar experiment, where the E-region was probed from opposite directions by two SuperDARN

radars at McMurdo and Dome Concordia Antarctic stations. These results have also been recently published [*Forsythe and Makarevich*, 2015]. Chapter 5 presents an experimental statistical study of the occurrence of the high-latitude E-region irregularities observed by the SuperDARN South Pole and Zhongshan radars. E-region velocity distributions are examined together with the distributions of the F-region convection component derived from all southern SuperDARN radars, in order to investigate the fundamental dependence of the phase velocity on the plasma convection component. These results were also presented in a recent journal article [*Forsythe and Makarevich*, 2017]. Finally, Chapter 6 describes major conclusions of this body of work and presents suggestions for future research.

1.5 References

Bahsen, A. E., E. Ungstrup, C. G. Falthammar, U. Fahleson, J. K. Olesen, F. Primadahl, F. Spangslev, and A. Pedersen (1978), Electrostatic waves observed in an unstable polar cap ionosphere, *J. Geophys. Res.*, *83*, 5191–5198.

Balsley, B. B., and D. T. Farley (1971), Radar studies of the equatorial electrojet at three frequencies, *J. Geophys. Res.*, *76*, 8341–8351.

Buneman, O. (1963), Excitation of field-aligned sound waves by electron streams, *Phys. Rev. Lett.*, *10*, 285–287.

Carter, B. A. (2011), HF radar observations of E-region plasma waves in the sub-auroral, auroral and polar regions, PhD Thesis, La Trobe University, Bundoora.

Carter, B. A., R. A. Makarevich, J. C. Devlin, and A. J. McDonald (2012), Coincident multi-point observations of the E- and F-region decametre-scale plasma waves at high latitudes, *J. Atmos. Sol. Terr. Phys.*, *80*, 323–335.

Chau, J. L., and J.-P. St.-Maurice (2016), Unusual 5 m E region field-aligned irregularities observed from Northern Germany during the magnetic storm of 17 March 2015, *J. Geophys. Res. Space Physics*, *121*(10), 10,316–10,340, doi:10.1002/2016JA023104.

D'Angelo, N., and J. K. Olesen (1975), On the relation of the 'slant E condition' in polar cap ionograms to the solar wind sector structure, *J. Geophys. Res.*, *80*, 2866–2868.

Deshpande, K., G. Bust, C. Clauer, C. Rino, and C. Carrano (2014), Satellite-beacon Ionospheric-scintillation Global Model of the upper Atmosphere (SIGMA) I: High-latitude sensitivity study of the model parameters, *J. Geophys. Res. Space Physics*, *119*, 4026–4043.

Dimant, Y. S., and M. M. Oppenheim (2004), Ion thermal effects on E-region instabilities: linear theory, *J. Atmos. Sol. Terr. Phys.*, *66*, 1639–1654, doi:10.1016/j.jastp.2004.07.006.

Dimant, Y. S., and M. M. Oppenheim (2011a), Magnetosphere-ionosphere coupling through E region turbulence: 1. Energy budget, *J. Geophys. Res.*, *116*, A09303, doi:10.1029/2011JA016648.

Dimant, Y. S., and M. M. Oppenheim (2011b), Magnetosphere-ionosphere coupling through E region turbulence: 2. Anomalous conductivities and frictional heating, *J. Geophys. Res.*, *116*, A09304, doi:10.1029/2011JA016649.

Dimant, Y. S., and R. N. Sudan (1997), Physical nature of a new cross-field current-driven instability in the lower ionosphere, *J. Geophys. Res.*, *102*, 2551–2564.

Eckersley, T. L. (1937), Irregular ionic clouds in the E layer of the ionosphere, *Nature*, *140*, 846–847.

Farley, D. T. (1963), A plasma instability resulting in field-aligned irregularities in the ionosphere, *J. Geophys. Res.*, *68*, 6083–6093.

Farley, D. T. (1985), Theory of equatorial electrojet plasma waves: new developments and current status, *J. Atmos. Terr. Phys.*, *47*, 729–744.

Farley, D. T., and B. G. Fejer (1975), The effect of the gradient drift term on type 1 electrojet irregularities, *J. Geophys. Res.*, *80*(22), 3087–3090.

Fejer, B. G., and M. C. Kelley (1980), Ionospheric irregularities, *Geophys. Rev.*, *18*, 401–454.

Fejer, B. G., D. T. Farley, B. B. Balsley, and R. F. Woodman (1975), Vertical structure of the VHF backscattering region in the equatorial electrojet and the gradient drift instability, *J. Geophys. Res.*, *80*, 1313–1324.

Fejer, B. G., J. Providakes, and D. T. Farley (1984), Theory of plasma waves in the auroral E region, *J. Geophys. Res.*, *89*, 7487–7494.

Fejer, J. A. (1979), Ionospheric instabilities and fine structure, *J. Atmos. Sol. Terr. Phys.*, *41*(7), 895 – 915.

Fejer, J. A., and J. F. Providakes (1987), High latitude E-region irregularities: new results., *Phys. Scripta.*, *18*, 167 – 178.

Fontenla, J. M. (2005), Chromospheric plasma and the Farley-Buneman instability in solar magnetic regions, *A&A*, *442*, 1099–1103.

Fontenla, J. M., W. K. Peterson, and J. Harder (2008), Chromospheric heating by the Farley-Buneman instability, *A&A*, *480*, 839–846.

Forsythe, V. V., and R. A. Makarevich (2015), Dual radar investigation of E region plasma waves in the southern polar cap, *J. Geophys. Res. Space Physics*, *120*(10), 9132–9147, doi:10.1002/2015JA021664.

Forsythe, V. V., and R. A. Makarevich (2016), Asymmetry in the Farley-Buneman dispersion relation caused by parallel electric fields, *J. Geophys. Res. Space Physics*, *121*(11), 11,391–11,406, doi:10.1002/2016JA023390.

Forsythe, V. V., and R. A. Makarevich (2017), Global view of the E-region irregularity and convection velocities in the high-latitude southern hemisphere, *J. Geophys. Res. Space Physics*, *122*, doi:10.1002/2016JA023711.

Foster, J. C., D. Tetenbaum, C. F. del Pozo, J.-P. St-Maurice, and D. R. Moorcroft (1992), Aspect angle variations in intensity, phase velocity and altitude for high-latitude 34 cm *E* region irregularities, *J. Geophys. Res.*, *97*, 8601–8617.

Gogoberidze, G., Y. Voitenko, S. Poedts, and M. Goossens (2009), Farley-Buneman instability in the solar chromosphere, *The Astrophys. J.*, *706*, L12–L16.

Haldoupis, C. (1989), A review on radio studies of auroral E region ionospheric irregularities, *Ann. Geophysicae*, *7*, 239–258.

Haldoupis, C., K. Schlegel, and G. Hussey (2000), Auroral E-region electron density gradients measured with EISCAT, *Ann. Geophysicae*, *18*, 1172–1181.

Haldoupis, C., T. Ogawa, K. Schlegel, J. A. Koehler, and T. Ono (2005), Is there a plasma density gradient role on the generation of short-scale Farley-Buneman waves?, *Ann. Geophysicae*, *23*, 3323–3337.

Hamza, A. M., and J.-P. St.-Maurice (1993), A turbulent theoretical framework for the study of current-driven *E* region irregularities at high latitudes: Basic derivation and application to gradient-free situations, *J. Geophys. Res.*, *98*, 11,587–11,599.

Hanuise, C. (1983), High latitude ionospheric irregularities, *Radio Sci.*, *18*, 1093–1121.

Hanuise, C., and M. Crochet (1981), 5–50-m wavelength plasma instabilities in the equatorial electrojet 2. Two-stream conditions, *J. Geophys. Res.*, *86*, 3567–3572.

Harang, L., and W. Stoffregen (1938), Scattered reflections of radio waves from a height of more than 100 km, *Nature*, *142*, 832–833.

Hassan, E., W. Horton, A. I. Smolyakov, D. R. Hatch, and S. K. Litt (2015), Multiscale equatorial electrojet turbulence: Baseline 2-D model, *J. Geophys. Res. Space Physics*, *120*(2), 1460–1477, doi:10.1002/2014JA020387.

Hedin, A. E. (1991), Extension of the MSIS thermospheric model into the middle and lower atmosphere, *J. Geophys. Res.*, *96*, 1159–1172.

Hoh, F. C. (1963), Instability of Penning-type discharge, *Phys. Fluids*, *6*, 1184–1191.

Homeier, N., and L. Wei (2013), Solar storm risk to the north American electric grid, *Tech. rep.*, Lloyd's and the Atmospheric and Environmental Research.

Hunsucker, R. D., and J. K. Hargreaves (2003), *The high latitude ionosphere and its effects on radio propagation*, Cambridge University Press, Cambridge.

Iversen, I. B., N. D'Angelo, and J. K. Olesen (1975), Further evidence for the Farley-Buneman instability in the polar cap ionosphere, *J. Geophys. Res.*, *80*, 3713–3714.

John, P. I., and Y. C. Saxena (1975), Observation of the Farley-Buneman instability in laboratory plasma, *Phys. Res. Lab.*, *2*, 251–254.

Kagan, L. M., and M. C. Kelley (2000), A thermal mechanism for generation of small-scale irregularities in the ionospheric E region, *J. Geophys. Res.*, *105*, 5291–5303.

Kagan, L. M., and J.-P. St.-Maurice (2004), Impact of electron thermal effects on Farley-Buneman waves at arbitrary aspect angles, *J. Geophys. Res. Space Physics*, *109*(A12), doi:10.1029/2004JA010444.

Keskinen, M. J., and S. L. Ossakow (1982), Nonlinear evolution of plasma enhancements in the auroral ionosphere. I - Long wavelength irregularities, *J. Geophys. Res.*, *87*, 144–150.

Kissack, R. S., J.-P. St.-Maurice, and D. R. Moorcroft (1997), The effect of electron-neutral energy exchange on the fluid Farley-Buneman instability threshold, *J. Geophys. Res.*, *102*(A11), 24,091–24,115.

Kissack, R. S., L. M. Kagan, and J.-P. St.-Maurice (2008a), Thermal effects on Farley-Buneman waves at nonzero aspect and flow angles. I. Dispersion relation, *Phys. Plasmas*, *15*, 022901, doi:10.1063/1.2834275.

Kissack, R. S., L. M. Kagan, and J.-P. St.-Maurice (2008b), Thermal effects on Farley-Buneman waves at nonzero aspect and flow angles. II. Behavior near threshold, *Phys. Plasmas*, *15*, 022902, doi:10.1063/1.2834276.

Koustov, A. V., K. Igarashi, D. André, K. Ohtaka, N. Sato, H. Yamagishi, and A. Yukimatu (2001), Observations of 50- and 12-MHz auroral coherent echoes at the Antarctic Syowa station, *J. Geophys. Res.*, *106*, 12,875–12,887.

Koustov, A. V., D. W. Danskin, R. A. Makarevitch, and J. D. Gorin (2005), On the relationship between the velocity of E-region HF echoes and ExB plasma drift, *Ann. Geophysicae*, *23*, 371–378.

Kustov, A. V., J. A. Koehler, G. J. Sofko, D. W. Danskin, and M. J. McKibben (1994a), Observations of 50-MHz type-II coherent echoes from within the polar cap, *Ann. Geophysicae*, *12*(8), 765–774.

Kustov, A. V., M. V. Uspensky, G. J. Sofko, J. A. Koehler, and J. Mu (1994b), Aspect angle dependence of the radar aurora Doppler velocity, *J. Geophys. Res.*, *99*, 2131–2144.

Lacroix, P. J., and D. R. Moorcroft (2001), Ion acoustic HF radar echoes at high latitudes and far ranges, *J. Geophys. Res.*, *106*(A12), 29,091–29,103, doi:10.1029/2001JA000024.

Linson, L. M., and J. B. Workman (1970), Formation of striations in ionospheric plasma clouds, *J. Geophys. Res.*, *75*, 3211–3219.

Litt, S. K., A. I. Smolyakov, A. S. Bains, O. A. Pokhotelov, O. G. Onishchenko, and W. Horton (2016), Nonlinear equation for Farley-Buneman waves in multispecies plasma, *Plasma Phys. Rep.*, *42*(5), 400–406, doi:10.1134/S1063780X16050081.

Makarevich, R. A. (2014), Symmetry considerations in the two-fluid theory of the gradient drift instability in the lower ionosphere, *J. Geophys. Res. Space Physics*, *119*(9), 7902–7913, doi:10.1002/2014JA020292.

Makarevich, R. A. (2016a), Toward an integrated view of ionospheric plasma instabilities: Altitudinal transitions and strong gradient case, *J. Geophys. Res. Space Physics*, *121*, 3634–3647, doi:10.1002/2016JA022515.

Makarevich, R. A. (2016b), Toward an integrated view of ionospheric plasma instabilities: 2. Three inertial modes of a cubic dispersion relation, *J. Geophys. Res. Space Physics*, doi:10.1002/2016JA022864.

Makarevich, R. A., A. Senior, A. V. Koustov, M. V. Uspensky, F. Honary, and P. L. Dyson (2006), A study of aspect angle effects in the E-region irregularity velocity using multi-point electric field measurements, *Geophys. Res. Lett.*, *33*, L21102, doi:10.1029/2006GL027740.

Makarevich, R. A., A. V. Koustov, A. Senior, M. Uspensky, F. Honary, and P. L. Dyson (2007), Aspect angle dependence of the E-region irregularity velocity at large flow angles, *J. Geophys. Res.*, *112*, A11303, doi:10.1029/2007JA012342.

Makarevich, R. A., A. C. Kellerman, Y. V. Bogdanova, and A. V. Koustov (2009), Time evolution of the subauroral electric fields: A case study during a sequence of two substorms, *J. Geophys. Res.*, *114*, A04312, doi:10.1029/2008JA013944.

Makarevich, R. A., V. V. Forsythe, and A. C. Kellerman (2015), Electric field control of E region coherent echoes: Evidence from radar observations at the South Pole, *J. Geophys. Res. Space Physics*, *120*, 2148–2165, doi:10.1002/2014JA020844.

Makarevitch, R. (2003), Formation of small-scale irregularities in the auroral E region, PhD Thesis, University of Saskatchewan.

Makarevitch, R. A., T. Ogawa, K. Igarashi, A. V. Koustov, N. Sato, K. Ohtaka, H. Yamagishi, and A. Yukimatu (2001), On the power-velocity relationship for 12- and 50-MHz auroral coherent echoes, *J. Geophys. Res.*, *106*, 15,455–15,470.

Makarevitch, R. A., A. V. Koustov, K. Igarashi, N. Sato, T. Ogawa, K. Ohtaka, H. Yamagishi, and A. S. Yukimatu (2002a), Comparison of flow angle variations of E-region echo characteristics at VHF and HF, *Adv. Polar Upper Atmos. Res.*, *16*, 59–83.

Makarevitch, R. A., A. V. Koustov, G. J. Sofko, D. André, and T. Ogawa (2002b), Multifrequency measurements of HF Doppler velocity in the auroral E region, *J. Geophys. Res.*, *107*, 1212, doi:10.1029/2001JA000268.

Makarevitch, R. A., F. Honary, and A. V. Koustov (2004), Simultaneous HF measurements of E- and F-region Doppler velocity at large flow angles, *Ann. Geophysicae*, *22*, 1177–1188.

Milan, S. E., and M. Lester (2001), A classification of spectral populations observed in HF radar backscatter from the E region auroral electrojets, *Ann. Geophysicae*, *19*, 189–204.

Nielsen, E. (1986), Aspect angle dependence of mean Doppler velocities of 1-m auroral plasma waves, *J. Geophys. Res.*, *91*, 10,173–10,177.

Nielsen, E., and K. Schlegel (1983), A first comparison of STARE and EISCAT electron drift velocity measurements, *J. Geophys. Res.*, *88*, 5745–5750.

Nielsen, E., and K. Schlegel (1985), Coherent radar Doppler measurements and their relationship to the ionospheric electron drift velocity, *J. Geophys. Res.*, *90*, 3498–3504.

Ogawa, T., B. B. Balsley, W. L. Ecklund, D. A. Carter, and P. E. Johnston (1980), Aspect angle dependence of irregularity phase velocities in the auroral electrojet, *Geophys. Res. Lett.*, *7*, 1081–1084.

Ogawa, T., B. B. Balsley, W. L. Ecklund, D. A. Carter, and P. E. Johnston (1982), Auroral radar observations at Siple Station, *J. Atmos. Terr. Phys.*, *44*, 529–537.

Olesen, J. K., F. Primdahl, F. Spangslev, and N. D'Angelo (1975), On the Farley instability in the polar cap E region, *J. Geophys. Res.*, *80*, 696–698.

Oppenheim, M. M., and Y. S. Dimant (2013), Kinetic simulations of 3-D Farley-Buneman turbulence and anomalous electron heating, *J. Geophys. Res.*, *118*, 1306–1318, doi:10.1002/jgra.50196.

Oppenheim, M. M., Y. Dimant, and L. P. Dyrud (2008), Large-scale simulations of 2-D fully kinetic Farley-Buneman turbulence, *Ann. Geophysicae*, *26*, 543–553, doi:10.5194/angeo-26-543-2008.

Ossakow, S. L., and P. K. Chaturvedi (1979), Current convective instability in the diffuse aurora, *Geophys. Res. Lett.*, *6*, 332–334.

Ossakow, S. L., P. K. Chaturvedi, and J. B. Workman (1978), High-altitude limit of the gradient drift instability, *J. Geophys. Res.*, *83*, 2691–2693.

Prakash, S., S. P. Gupta, B. H. Subbaraya, and C. L. Jain (1971), Electrostatic plasma instability in the equatorial electrojet, *Nature*, *233*, 56–58.

Primdahl, F., J. K. Olesen, and F. Spangslev (1974), Backscatter from a postulated plasma instability in the polar cap ionosphere and the direct measurement of a horizontal E region current, *J. Geophys. Res.*, *79*, 4262–4268.

Pullen, S., Y. S. Park, and P. Enge (2009), Impact and mitigation of ionospheric anomalies on ground-based augmentation of GNSS, *Radio Sci.*, *44*.

Rogister, A., and N. D'Angelo (1970), Type II irregularities in the equatorial electrojet, *J. Geophys. Res.*, *75*, 3879–3887.

Sahr, J., and B. G. Fejer (1996), Auroral electrojet plasma irregularity theory and experiment: A critical review of present understanding and future directions, *J. Geophys. Res.*, *101*, 26,893–26,909.

Sahr, J. D. (1990), Observation and theory of the radar aurora, PhD Thesis, Cornell University.

Schlegel, K., and D. R. Moorcroft (1989), EISCAT as a tristatic auroral radar, *J. Geophys. Res.*, *94*, 1430–1438.

Schunk, R. W., and A. F. Nagy (1978), Electron temperatures in the F region of the ionosphere: Theory and observations, *Rev. Geophys. Space Phys.*, *16*, 355–399.

Seo, J., T. Walter, and P. Enge (2011), Availability impact on GPS aviation due to strong ionospheric scintillation, *IEEE Transactions on Aerospace and Electronic Systems*, *47*, 1963–1973.

Shepherd, S. G. (2014), Altitude-adjusted corrected geomagnetic coordinates: Definition and functional approximations, *J. Geophys. Res.*, *119*(9), 7501–7521, doi:10.1002/2014JA020264.

Simon, A. (1963), Instability of a partially ionized plasma in a crossed electric and magnetic fields, *Phys. Fluids*, *6*, 382–388.

St.-Maurice, J.-P., and J. L. Chau (2016), A theoretical framework for the changing spectral properties of meter-scale Farley-Buneman waves between 90 and 125 km altitudes, *J. Geophys. Res. Space Physics*, *121*(10), 10,341–10,366, doi:10.1002/2016JA023105.

St.-Maurice, J.-P., and R. S. Kissack (2000), The role played by thermal feedback in heated Farley-Buneman waves at high latitudes, *Ann. Geophysicae*, *18*, 532–546.

Sudan, R. N. (1983), Unified theory of type 1 and type 2 irregularities in the equatorial electrojet, *J. Geophys. Res.*, *88*, 4853–4860.

Sudan, R. N., J. Akinrimisi, and D. T. Farley (1973), Generation of small-scale irregularities in the equatorial electrojet, *J. Geophys. Res.*, *78*, 240–248.

Tsunoda, R. T., P. D. Perreault, and J. C. Hodges (1976), Azimuthal distribution of HF slant E echoes and its relationship to the polar cap electric field, *J. Geophys. Res.*, *81*, 3834–3844.

Tsurutani, B. T., W. D. Gonzalez, G. S. Lakhina, and S. Alex (2003), The extreme magnetic storm of 12 September 1859, *J. Geophys. Res. Space Physics*, *108*, doi: 10.1029/2002JA009504.

Uspensky, M., A. Koustov, P. Janhunen, R. Pellinen, D. Danskin, and S. Nozawa (2003), STARE velocities: importance of off-orthogonality and ion motions, *Ann. Geophysicae*, *21*, 729–743.

Uspensky, M., A. Koustov, P. Janhunen, E. Nielsen, K. Kauristie, O. Amm, R. Pellinen, H. Opgenoorth, and R. Pirjola (2004), STARE velocities: 2 Evening westward electron flow, *Ann. Geophysicae*, *22*, 1077–1091.

Chapter 2

Asymmetry in the Farley-Buneman Dispersion Relation Caused by Parallel Electric Fields [I]

2.1 Abstract

An implicit assumption utilized in studies of E-region plasma waves generated by the Farley-Buneman instability (FBI) is that the FBI dispersion relation and its solutions for the growth rate and phase velocity are perfectly symmetric with respect to the reversal of the wave propagation component parallel to the magnetic field. In the present study, a recently-derived general dispersion relation that describes fundamental plasma instabilities in the lower ionosphere including FBI is considered and it is demonstrated that the dispersion relation is symmetric only for background electric fields that are perfectly perpendicular to the magnetic field. It is shown that parallel electric fields result in significant differences between the growth rates and phase velocities for the parallel propagation components of opposite signs. These differences are evaluated using numerical solutions of the general dispersion relation and shown to exhibit an approximately linear relationship with the parallel electric field near the E region peak altitude of 110 km. An analytic expression for the differences is also derived from an approximate version of the dispersion relation, with comparisons between numerical and analytic results agreeing near 110 km. It is further demonstrated that parallel electric fields do not change the overall symmetry when the full 3D wave propagation vector is reversed, with no symmetry seen when either the perpendicular or parallel component is reversed. The present results indicate that moderate-to-strong parallel electric fields of 0.1–1.0 mV/m can result in experimentally measurable differences between the characteristics of plasma waves with parallel propagation components of opposite polarity.

[I]Published as: Forsythe V. V., and R. A. Makarevich (2016), Asymmetry in the Farley-Buneman dispersion relation caused by parallel electric fields, *J. Geophys. Res. Space Physics*, *121*, 11391-11406, doi:10.1002/2016JA023390.

2.2 Introduction

Plasma in the ionospheric E region becomes unstable to the modified two-stream plasma instability also known as the Farley-Buneman instability (FBI) [*Farley*, 1963; *Buneman*, 1963] when the electric field or, alternatively, the relative drift velocity between electrons and ions exceeds a certain threshold value. The instability generates plasma waves or irregularities that can be detected with coherent radars as ionospheric backscatter or echoes [e.g., see reviews by *Fejer and Kelley*, 1980; *Sahr and Fejer*, 1996]. The plasma irregularity characteristics, such as growth rate and phase velocity, are strongly dependent on the angle between the wave propagation vector $\mathbf{k}$ and the plane perpendicular to the Earth's magnetic field, known as the aspect angle α. A strong decrease for radar echo power with angle α has been experimentally demonstrated by numerous previous studies [e.g. *Ecklund et al.*, 1975; *Koehler et al.*, 1985; *Foster et al.*, 1992], with a similarly strong decrease also found for irregularity velocity [*Ogawa et al.*, 1980; *Nielsen*, 1986; *Kustov et al.*, 1994; *Makarevich et al.*, 2007].

Implicit in all of the above investigations of the fundamental dependence on the aspect angle was the assumption that irregularity characteristics are symmetric functions of aspect angle, i.e. that the echo power or velocity measured at positive and negative aspect angles are expected to be the same. One exception to the above rule for the irregularity growth rate was realized recently by *Bahcivan and Cosgrove* [2010] who investigated the effects of plasma density gradients parallel to the magnetic field, $\nabla_{\parallel} n$, on FBI waves. It was shown that the growth rate of 50-m waves is a symmetric function of aspect angle only in the absence of significant parallel density gradients. The symmetry in the growth rate breaks and becomes more pronounced with strengthening gradients $|\nabla_{\parallel} n|$, with the peak growth achieved at either positive or negative angles α depending on the sign of $\nabla_{\parallel} n$. This also means that FBI waves will tend to propagate at nonzero aspect angles. The phase velocity, however, appeared symmetric with aspect angle for all values of the gradient scale [*Bahcivan and Cosgrove*, 2010, and their Figure 3].

In the present study, it is demonstrated that electric fields parallel to the magnetic field $E_{\parallel}$ also break the symmetry of the FBI dispersion relation with respect to the reversal of the aspect angle and that, unlike the parallel gradients, parallel electric fields can result in significant asymmetries not only for the growth rate but also for the phase velocity. It is further demonstrated that a much more general symmetry property exists when both perpendicular and parallel components of the wave propagation vector are reversed and

that no such symmetry occurs when only one component is reversed.

2.3 Methodology of the Asymmetry Analysis

The linear fluid theory of the FBI waves predicts that both the growth rate γ and phase velocity V_{ph} are fast decreasing function of the aspect angle α [e.g. *Sahr and Fejer*, 1996]. The definition of the aspect angle and the decomposition of the wave propagation vector $\mathbf{k}$ in terms of its components perpendicular and parallel to the magnetic field $\mathbf{B}$ are illustrated in Figure 2.1. The magnetic field was set to be in the $-\hat{z}$ direction, and the plasma drift velocity $\mathbf{V}_E = \mathbf{E} \times \mathbf{B}/B^2$ was set to be in the $\hat{y}$ direction. The magnetic aspect angle α is defined as the angle between the wave vector $\mathbf{k}$ and the plane perpendicular to the magnetic field $\mathbf{B}$: $\tan\alpha = k_z/k_\perp$ or $\sin\alpha = k_z/k$. Figure 2.1 also illustrates that any specific value of the aspect angle $\alpha = const$ defines a surface in the $\mathbf{k}$-space. For the case of $\alpha = 0$, it is a plane perpendicular to the magnetic field, whereas for $\alpha \neq 0$ the surface is a cone. Finally, the angle between the perpendicular component of the differential drift between electrons and ions $\mathbf{V}_{d\perp} = \mathbf{V}_{e0\perp} - \mathbf{V}_{i0\perp}$ and the perpendicular component of the propagation vector $\mathbf{k}_\perp$ is referred to as the flow angle θ.

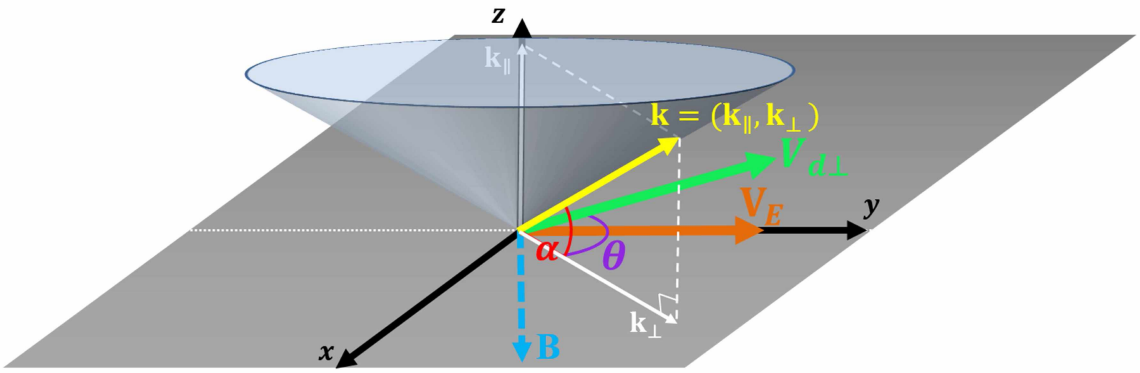

Figure 2.1. Definition of the aspect angle α and the flow angle θ. Shown is the decomposition of the wave propagation vector $\mathbf{k}$ relative to the magnetic field $\mathbf{B}$ and the perpendicular component of the differential drift drift between electrons and ions $\mathbf{V}_{d\perp}$. Also shown are the plasma drift velocity $\mathbf{V}_E$, field-perpendicular plane, and the cone in $\mathbf{k}$-space that defines a surface of constant aspect angle.

In this study, we utilize a general dispersion relation based on the general fluid formalism that integrated both the E and F-region cases for finite inertia, plasma temperature, and arbitrary gradient and propagation vectors [*Makarevich*, 2016a, b]. Numerical solutions for the complex wave frequency $\omega = \omega_r + i\gamma$ and, therefore, for the growth rate γ and phase velocity $V_{ph} = \omega_r/k$ can be obtained from this general dispersion relation by using a simple

iterative process [*Makarevich*, 2016a] or a more advanced and robust numerical method [*Makarevich*, 2016b], with the latter method being predominantly used in the current study.

In this theoretical technique, numerical solutions are obtained for any given combination of the following parameters: plasma drift velocity $\mathbf{V}_E$, gradient vector $\mathbf{G} = \nabla n/n$, wave propagation vector $\mathbf{k}$ and the altitude-dependent ratios between collision and gyro frequencies for both electrons r_e and ions r_i [*Makarevich*, 2016b]. In the current set of calculations, the following parameters were used: no plasma gradients $G = 0$ and the convection velocity of $V_E = 1000$ m/s oriented along the y axis as shown in Figure 2.1. The r_e and r_i values were estimated using neutral densities from the Mass Spectrometer Incoherent Scatter Model Extended (MSIS-E-90) [*Hedin*, 1991] and standard expressions given by *Schunk and Nagy* [1978] and *Schunk and Nagy* [1980]. The gyrofrequencies for ions $\Omega_i = |e|B/m_i$ and electrons $\Omega_e = -|e|B/m_e$ (negative in this notation convention) were taken to be constant with altitude and equal to 150 s^{-1} and -10^7 s^{-1} respectively. The geographic coordinates of 80°E, 60°S and the time of 14:00 magnetic local time (MLT) on February 15, 2013 were selected to represent summer daytime conditions at high southern latitudes which were recently demonstrated to have a significant presence of echoes of likely FBI origin [*Makarevich et al.*, 2015; *Forsythe and Makarevich*, 2015].

Aspect angle α and the flow angle θ are the two parameters that define the position of the wavevector $\mathbf{k}$ in the $\mathbf{k}$-space in relation to the perpendicular component of the differential drift velocity $\mathbf{V}_{d\perp}$ and the magnetic field $\mathbf{B}$, Figure 2.1. In this study, it is demonstrated that a reversal of the aspect angle is equivalent to the reversal of the flow angle and for this reason both complementary dependencies are considered. In practice, numerical solutions of the dispersion relation were obtained for different values of aspect angle α, ranging from $-1°$ to $+1°$ with a $0.02°$ step, and full range of flow angles θ from $0°$ to $360°$ with a $10°$ step.

Three different approaches were used to analyze the asymmetry. First, the symmetry properties with respect to a reversal in the aspect angle were analysed by reversing the parallel component of the wave vector $\mathbf{k}_\parallel$ and keeping the perpendicular component $\mathbf{k}_\perp$ the same, finding the complex wave frequency ω (and hence the growth rate and phase velocity) for these new propagation vectors $\omega\left(-\mathbf{k}_\parallel, \mathbf{k}_\perp\right)$, and comparing with the values obtained before the reversal $\omega\left(\mathbf{k}_\parallel, \mathbf{k}_\perp\right)$, section 2.4. This is equivalent to comparing dependencies on the aspect and flow angles: $\omega\left(-\alpha, \theta\right)$ and $\omega\left(\alpha, \theta\right)$. Second, symmetry with respect to the flow angle reversal was analysed by comparing pairs $\omega\left(\mathbf{k}_\parallel, -\mathbf{k}_\perp\right)$ and $\omega\left(\mathbf{k}_\parallel, \mathbf{k}_\perp\right)$, section

2.5. Finally, the general symmetry in the dispersion relation was analysed by reversing the full 3D wave vector and comparing $\omega(-\mathbf{k})$ and $\omega(\mathbf{k})$, section 2.6.

2.4 Symmetry in Aspect Angle α

Symmetry with respect to the aspect angle α reversal is investigated first. Figure 2.2 shows numerical solutions obtained as described in Section 2.3, in terms of the (a)–(d) growth rate and (e)–(h) phase velocity. The different color lines in Figure 2.2 correspond to different values of the flow angle θ, with the color bar given to the right of the figure. Four rows correspond to different values of the parallel electric field $E_{0\parallel}$, which are given in the top-left corner of the respective row. Electric field can be also expressed through the differential drift between electrons and ions $\mathbf{V}_d = \mathbf{V}_{e0} - \mathbf{V}_{i0}$ [*Makarevich*, 2016a, Equation 6]. The component of the differential drift parallel to the magnetic field $V_{d\parallel}$ is also shown in the top-left corner of each row, expressed as multiples of the ion-acoustic speed C_s: 0 C_s, 25 C_s, 50 C_s, 75 C_s. The specific relationship between $V_{d\parallel}$ and $E_{0\parallel}$ that was used here was $E_{0\parallel} = V_{d\parallel} B/(r_e^{-1} - r_i^{-1})$, obtained from equation (6) of *Makarevich* [2016a]. The magnitude of the magnetic field B was taken to be 50 μT. The ion-acoustic speed C_s was estimated from the convection drift speed of $V_E = 1000$ m/s, using empirical model of *Gorin et al.* [2012].

Figures 2.2a and 2.2e show that, in the absence of a parallel electric field $E_{0\parallel}$, both the growth rate γ and phase velocity V_{ph} are perfectly symmetric with respect to the aspect angle reversal. Only a particular range of the flow angles have positive growth rates $\gamma > 0$. In Figure 2.2a, the lines for flow angles of 0°–180° are behind those for 180°–360°. Once a parallel electric field is introduced, the growth rate is no longer symmetric for any given flow angle and both ranges 0°–180° and 180°–360° are visible, Figures 2.2b–2.2d. The waves become more unstable at negative (positive) aspect angles for flow angles of 0°–180° (180°–360°) with an increasing parallel electric field. Importantly, the phase velocity also loses its symmetry, Figures 2.2f–2.2h. The positive (negative) peak phase velocity shifts more towards positive (negative) aspect angles with increasing $E_{0\parallel}$ and the values on the right (left) of each panel (f)–(h) get progressively higher than those on the left (right).

To further illustrate the point about the asymmetry in the solution, the vertical white dashed lines indicate the aspect angle values of $-0.5°$, 0° and 0.5°, with the values at $\alpha = +0.5°$ being always higher than those at $-0.5°$. These specific values of the aspect angle will be used to quantify the asymmetry of the growth rate and phase velocity in the

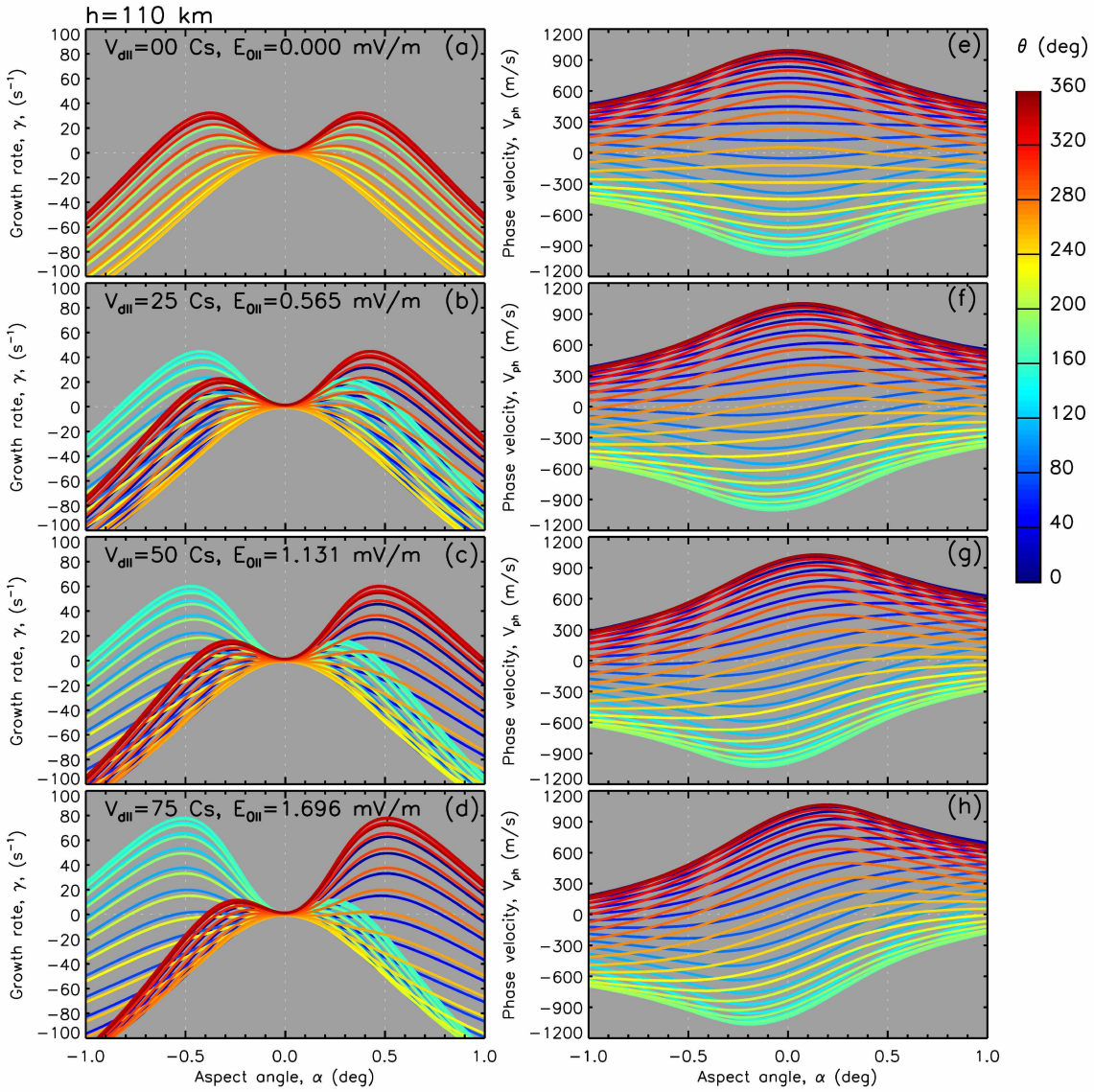

Figure 2.2. Aspect angle dependence of the (a–d) growth rate and (e–h) phase velocity at an altitude of 110 km and for different propagation directions θ indicated by the color of the line according to the color bar on the right. The four rows correspond to four selected values of the parallel differential drift $V_{d\|}$ or, equivalently, parallel electric field $E_{0\|}$, which are given in the top-left corner of each row.

following analysis.

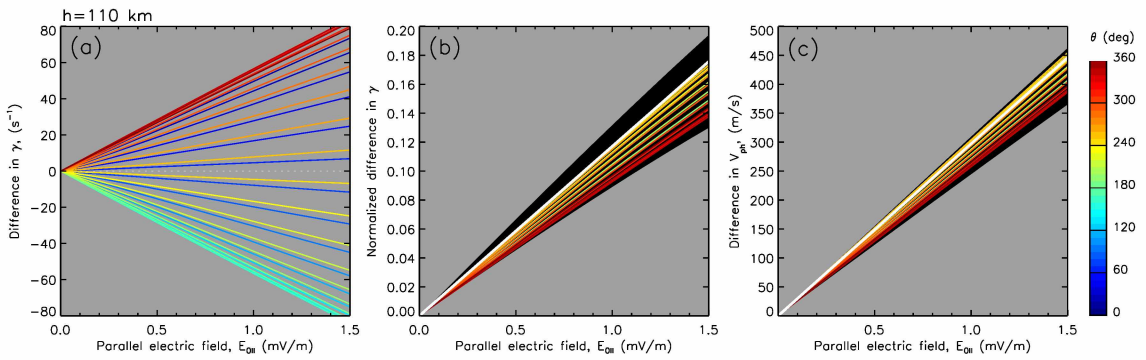

Figure 2.3. The difference in the (a) growth rate, (b) normalized growth rate, and (c) phase velocity between the positive and negative aspect angle values of 0.5° at an altitude of 110 km. The black area in (b) and (c) shows the spread in the analytic solution due to the flow angle variation (see text for details). The white lines in (b) and (c) show results based on the leading terms in the analytic expressions. The color of each line indicates the flow angle θ.

For the next analysis, the asymmetry in the growth rate γ and phase velocity V_{ph} was quantified as the difference between the respective values taken at aspect angles of $+0.5°$ and $-0.5°$. This asymmetry was calculated for different values of the parallel electric field $E_{0\parallel}$ ranging between 0.0 and 1.5 mV/m with a resolution step of 0.1 mV/m.

Figure 2.3a shows the asymmetry versus parallel electric field $E_{0\parallel}$, with different colors again representing different flow angles. As can be seen in Figure 2.3a, the asymmetry in the growth rate γ has a large spread in the flow angle and the lines with 180° difference do not have exactly the same values, since one can see both ranges of $\theta = 0°$–$180°$ and $\theta = 180°$–$360°$. Moreover, the lines at flow angles between $-90°$ and $+90°$ (red and blue) have positive slopes, whereas other lines have negative slopes. This feature indicates that the asymmetry in the growth rate γ may be proportional to the factor $\mathbf{V}_d \cdot \mathbf{k}_\perp = V_d k_\perp \cos\theta$. Figure 2.3b presents the same information as Figure 2.3a, but with the growth rate normalized by the factor $\mathbf{V}_d \cdot \mathbf{k}_\perp$. After the normalization, the growth rate becomes a unitless value. In this presentation, asymmetry in the normalized growth rate is always positive and the spread between lines at different flow angles is much smaller. Now the lines for $\theta = 180°$–$360°$ appear on top of the lines for $\theta = 0°$–$180°$. The spread between the lines with maximum and minimum slopes is relatively small; due to linearity it is independent of $E_{0\parallel}$ and can be estimated at any point, e.g. at $E_{0\parallel} = 1.5$ mV/m it is $(0.175 - 0.135)/0.135 \approx 0.3$ as a dimensionless fraction. That is, the spread in the slope is ∼3 times less than the minimum

slope.

Figure 2.3c presents the difference between the phase velocity values at $\alpha = \pm 0.5°$. It shows that the phase velocity asymmetry has a spread in the flow angle θ that is relatively small and is more similar to that in the normalized growth rate. The estimated spread between the lines with maximum and minimum slopes is $\sim 1/6$, i.e. it is smaller than that for the growth rate by a factor of 2. The velocity difference is 100–150 m/s at $E_{0\parallel} = 0.5$ mV/m and it rises quickly with increasing $E_{0\parallel}$. Figures 2.3a–2.3c also show that the increase with parallel electric field in all three quantities appears to be linear.

The final comment about Figure 2.3 is related to the results of analytic analysis conducted in an attempt to express the asymmetry in γ and V_{ph} as explicit functions of $E_{0\parallel}$. This analysis was based on approximate solutions of the general dispersion relation that are valid in the E region [*Makarevich*, 2016b]. The detailed derivation of these analytic expressions is presented in Appendix 2.A and the resulting expressions are shown below.

$$\gamma(\mathbf{k}_\parallel) - \gamma(-\mathbf{k}_\parallel) = \frac{4\hat{\psi}\mathbf{V}_d \cdot \mathbf{k}_\perp \mathbf{V}_d \cdot \mathbf{k}_\parallel}{\nu_i(1+\hat{\psi})^3}\left[1 + \frac{6\hat{\psi}^2 r_i^{-1} C k_\perp^2}{\nu_i(1+\hat{\psi})^2} - \frac{10\hat{\psi}^2\left((\mathbf{V}_d \cdot \mathbf{k}_\perp)^2 + (\mathbf{V}_d \cdot \mathbf{k}_\parallel)^2 - 3\hat{\psi}^2 r_i^{-2} C^2 k_\perp^4\right)}{\nu_i^2(1+\hat{\psi})^4}\right] \tag{2.1}$$

$$V_{ph}(\mathbf{k}_\parallel) - V_{ph}(-\mathbf{k}_\parallel) = \frac{2\mathbf{V}_{i0} \cdot \mathbf{k}_\parallel}{k} + \frac{2\mathbf{V}_d \cdot \mathbf{k}_\parallel}{k(1+\hat{\psi})}\left[1 + \frac{2\hat{\psi}^2 r_i^{-1} C k_\perp^2}{\nu_i(1+\hat{\psi})^2} - \frac{2\hat{\psi}^2\left((\mathbf{V}_d \cdot \mathbf{k}_\parallel)^2 + 3(\mathbf{V}_d \cdot \mathbf{k}_\perp)^2 - 3\hat{\psi}^2 r_i^{-2} C^2 k_\perp^4\right)}{\nu_i^2(1+\hat{\psi})^4}\right] \tag{2.2}$$

The results for the asymmetry in normalized growth rate and phase velocity based on Equations (2.1) and (2.2) are plotted in Figures 2.3b and 2.3c, respectively. To keep the diagram readable, the analytic results are presented as a black area between the lines with the largest and the smallest slopes. The flow angles where the extreme slopes were achieved were $\theta_{max} = 10°, 190°$ and $\theta_{min} = 100°, 280°$. The white lines in Figures 2.3b and 2.3c represent the leading terms in Equations (2.1) and (2.2), respectively.

Figures 2.3b and 2.3c show that the analytic results for both growth rate and phase velocity agree well with the numerically derived results. Importantly, this analysis confirms that the spread in the growth rate seen for different flow angles in Figure 2.3a is mostly due

to the common factor $\mathbf{V}_d \cdot \mathbf{k}_\perp$ in Equation (2.1) and that the spread can be much reduced if the growth rate is normalized by $\mathbf{V}_d \cdot \mathbf{k}_\perp$. The analytic results (2.1) and (2.2) reproduce the numerical results reasonably well even in their simplest form given by the leading term in Equations (2.1) and (2.2); this was shown by the white line in Figures 2.3b and 2.3c. The same trends with the two leading terms agreed closely with the steepest lines with all analytic terms included (not presented here for brevity). All other terms in Equations (2.1) and (2.2) are small and they mostly reduce the slopes from their highest values given by the two leading terms. The term proportional to $(\mathbf{V}_d \cdot \mathbf{k}_\perp)^2$ in both Equations (2.1) and (2.2) introduces a spread due to the flow angle variation which largely matches that of the numerical solutions (after normalization by the common factor $\mathbf{V}_d \cdot \mathbf{k}_\perp$ for growth rate). The reasons why analytic results have a somewhat larger spread than the numerical results are further discussed in section 5.7. Finally, apart from the term proportional to $\left(\mathbf{V}_d \cdot \mathbf{k}_\parallel\right)^3$, all terms are linear with $E_{0\parallel}$, which explains the linearity of numerical solutions seen in Figure 2.3. The cubic term $\left(\mathbf{V}_d \cdot \mathbf{k}_\parallel\right)^3$ introduces some nonlinearity, but it is hardly noticeable for the values of α and $E_{0\parallel}$ of interest.

So far the numerical solutions were calculated for an altitude of 110 km. This height is associated with the peak of the irregularity production through the FBI mechanism [e.g. *Pfaff et al.*, 1984]. This is also the altitudinal region where a general cubic dispersion relation can be approximated as a quadratic equation, with exact or approximate analytic solutions being available [*Makarevich*, 2016b] and used in the current study to compare with numerical solutions of the cubic equation. In order to determine whether similar parallel electric field effects occur at higher altitudes, numerical solutions of the cubic dispersion relation were calculated at altitudes of 110, 115, and 120 km and the same analysis was applied to find the asymmetry in the growth rate γ and phase velocity V_{ph}.

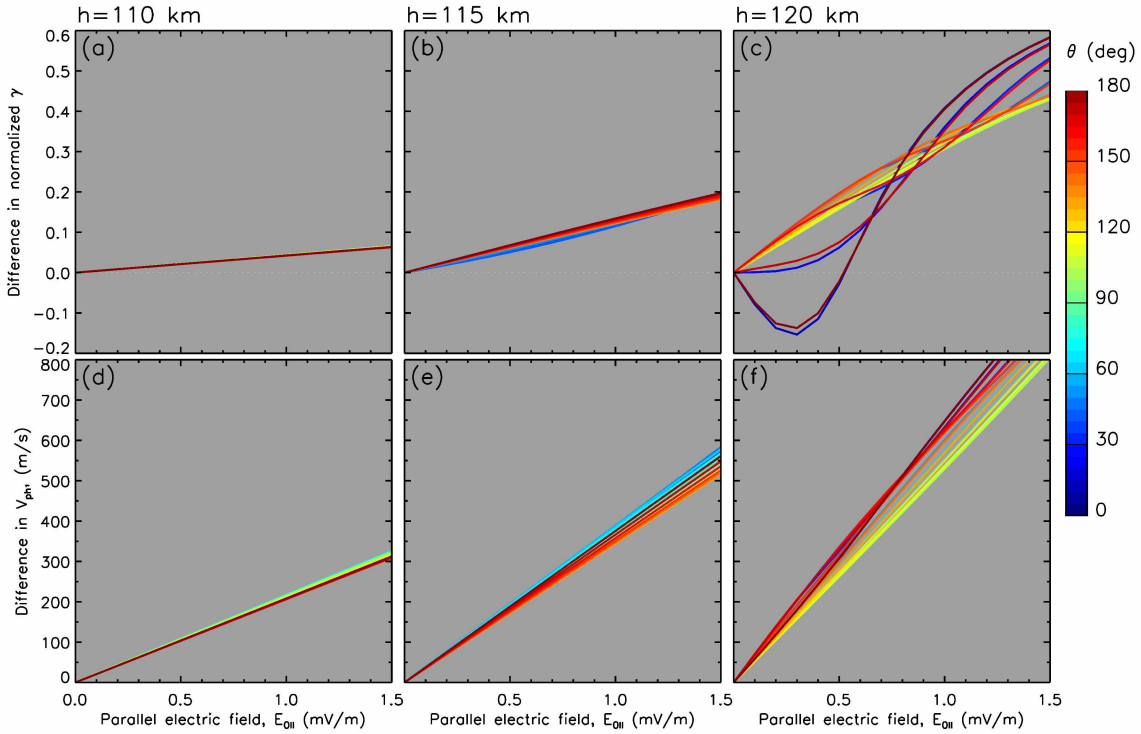

Figure 2.4. The difference in the (a–c) normalized growth rate and (d–f) the phase velocity between the positive and negative aspect angle values of 0.5° for three selected altitudes of 110, 115 and 120 km. The color of each line indicates the flow angle θ.

Figure 2.4 presents the results for the (a–c) normalized growth rate γ and (d–f) phase velocity V_{ph} for three altitudes of 110, 115, and 120 km, as indicated on top of the corresponding column. The range of the flow angles is restricted to 0°–180° here, since the lines for 0°–180° overlap with lines for 180°–360°. Figure 2.4 shows that the slopes become greater at higher altitudes. Interestingly, the linearity of the asymmetry breaks very slightly at the altitude of 115 km for θ of 0°–30° for the growth rate, and it breaks completely at altitude of 120 km, particularly for the growth rate and for the flow angles close to 0° and 180°. At an altitude of 110 km an approximate quadratic solution to the dispersion relation is appropriate, whereas at the higher altitudes one must consider the full cubic form of the solution to the dispersion relation. The fact that the linearity breaks with an increasing altitude is most likely due to a transition from a quadratic to cubic form of the solution to the dispersion relation, as further discussed in section 5.7.

2.5 Symmetry in Flow Angle θ

In addition to symmetry with respect to the aspect angle reversal, it is often assumed that properties of FBI waves are also symmetric with respect to the flow angle reversal, including existence of two symmetric cones of flow angles. This section will help the reader visualize how the symmetry of these cones breaks under the influence of the parallel electric field. In this presentation, the parallel electric field effects on the flow angle cones are more evident as compared to presentations of Figures 2.2 and 2.3. In addition, the previous analysis was performed for a fixed wavelength of 10 m ($k = 0.628$ m^{-1}), while in this section the effects of the parallel electric field are demonstrated in the somewhat broader range $\lambda > 5$ m.

Figure 2.5 shows the (a)–(d) growth rates and (e)–(h) phase velocities for different perpendicular wave vectors $\mathbf{k}_\perp$ and for an aspect angle of 0.5°. Different columns correspond to different values of the parallel electric field $E_{0\parallel}$ as indicated at the top of each column. Two-dimensional vectors $\mathbf{k}_\perp$ and $-\mathbf{k}_\perp$ and their components (k_x, k_y), $(-k_x, -k_y)$, are also shown in white. The direction of the perpendicular component of the differential drift velocity vector $\mathbf{V}_{d\perp}$ is shown in black in panel (a).

In the case when $E_{0\parallel} = 0$, Figures 2.5a and 2.5e, there are two symmetric flow angle cones where the growth rate is positive (red color), with the phase velocity of opposite polarities and of the same magnitude. This is further illustrated by the colors at the tips of the vectors $\mathbf{k}_\perp$ and $-\mathbf{k}_\perp$ that correspond to the (a) same and (e) opposite values. However, once $E_{0\parallel}$ increases, the symmetry breaks. For example, the cone at $k_y > 0$ gets larger in Figures 2.5a–2.5d and the cone at $k_y < 0$ gets smaller in Figures 2.5a–2.5c and finally disappears in Figure 2.5d. This is reflected in the colors at the tips of the two vectors $\mathbf{k}_\perp$ and $-\mathbf{k}_\perp$ becoming more different from Figure 2.5b to Figure 2.5d. For the phase velocity, its peak magnitude at $k_y > 0$ is also greater than that at $k_y < 0$, e.g. the shade of red is deeper in Figure 2.5h than in Figure 2.5e, while the shade of blue is lighter. Overall, Figure 2.5 clearly shows that no symmetry in the growth rate or antisymmetry in the phase velocity is seen when the perpendicular wave vector $\mathbf{k}_\perp$ is reversed except when $E_{0\parallel} = 0$.

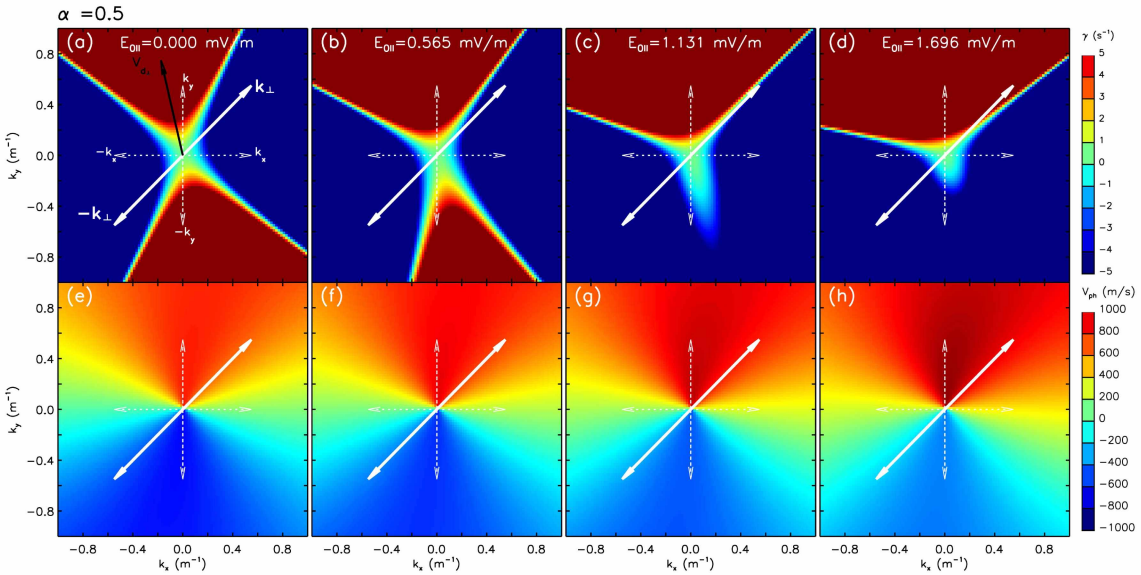

Figure 2.5. Dependence of the (a–d) growth rate and (e–h) phase velocity on the propagation vector $\mathbf{k}_\perp$ for the aspect angle of 0.5°. Columns 1 to 4 refer to different parallel electric field values as indicated in the top-left corner of each column. Perpendicular propagation vectors $\mathbf{k}_\perp$ with different polarities and their decomposition in 2D are shown in white color and the direction of the perpendicular component of the differential drift velocity vector $\mathbf{V}_{d\perp}$ is shown in black in panel (a).

2.6 General Symmetry

In sections 2.4 and 2.5, it was demonstrated that parallel electric fields break the symmetry in the solution of general dispersion relation when each component $\mathbf{k}_\perp$ or $\mathbf{k}_\parallel$ is reversed separately. In this section, it is demonstrated that when both components are reversed at the same time, i.e. when the full 3D vector $\mathbf{k}$ is reversed, the symmetry still holds.

Figure 2.6 demonstrates this property by using numerical solutions of the general dispersion relation, section 2.3. Shown are two cones of constant angles $\alpha = \pm 0.5°$ in the 3D $\mathbf{k}$-space color-coded in the (a) growth rate and (b) phase velocity for the parallel electric field $E_{0\parallel} = 0.565$ mV/m. The propagation wave vector $\mathbf{k}$ and its decomposition are shown in white and the reversed vector $-\mathbf{k}$ and its components are shown in gray.

In the case when the full vector $\mathbf{k}$ is reversed, it points to the surface of a different aspect angle cone. The colors near the tips of the vectors $\mathbf{k}$ and $-\mathbf{k}$ are the same (blue and blue) for the growth rate and opposite (orange and blue) for the phase velocity. In fact, this parity property is valid for any value of the background parallel electric field $E_{0\parallel}$ (not presented here for brevity).

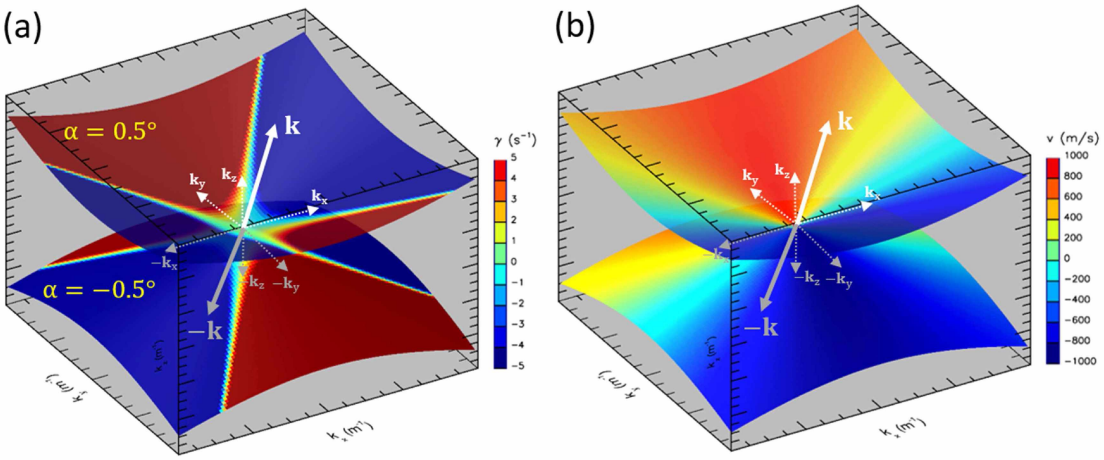

Figure 2.6. (a) Growth rate and (b) phase velocity on the surface of the two aspect angle cones of 0.5° and −0.5° in $\mathbf{k}$-space. The x and y axes are the same as in Figure 2.5. Propagation vectors with different polarity and their decomposition in 3D are shown in white and gray.

The same parity properties for the growth rate and phase velocity are demonstrated below using analytic expressions that are valid in the E region for nearly field-aligned irregularities $k_\parallel \ll k_\perp$ [*Makarevich*, 2016b]. In this case, the dispersion relation in the ion

frame can be written as

$$\omega' - \mathbf{V}_d \cdot \mathbf{k} + (D_i\omega' + iCk_\perp^2)\hat{\psi} r_i^{-1} = 0, \tag{2.3}$$

where $\omega' = \omega - \mathbf{V}_{i0} \cdot \mathbf{k}$ is complex wave frequency in the ion frame, $C \equiv (T_i + T_e)/B/|e|$ is a quantity related to the ion-acoustic speed C_s through $C = C_s^2/\Omega_i$, $D_i \equiv -i\Omega_i^{-1}\omega' + r_i$, and $\hat{\psi} = -r_i r_e(1 + r_e^{-2}\tan^2\alpha)$ is the modified anisotropy factor [*Sahr and Fejer*, 1996]. The exact solution of this quadratic equation is

$$\omega'(\mathbf{k}) = \frac{i\nu_i(1+\hat{\psi})}{2\hat{\psi}} \left[-1 \pm \sqrt{1 - \frac{4\hat{\psi} r_i^{-1}\Omega_i^{-1}}{(1+\hat{\psi})^2}\left(\hat{\psi} r_i^{-1} Ck_\perp^2 - i\mathbf{V}_d \cdot \mathbf{k}\right)} \right]. \tag{2.4}$$

To evaluate the real and imaginary parts, the following standard expression can be used

$$\sqrt{x+iy} = \pm\left(\sqrt{\frac{r+x}{2}} + isgn(y)\sqrt{\frac{r-x}{2}}\right), \qquad r = \sqrt{x^2+y^2}, \tag{2.5}$$

where for our specific square root in Equation (2.4)

$$x = 1 - \frac{4\hat{\psi}^2 r_i^{-2}\Omega_i^{-1} Ck_\perp^2}{(1+\hat{\psi})^2}, \qquad y = \frac{4\hat{\psi} r_i^{-1}\Omega_i^{-1}\mathbf{V}_d \cdot \mathbf{k}}{(1+\hat{\psi})^2}. \tag{2.6}$$

The complex frequency in the neutral frame can be written in terms of x, y, and r as

$$\omega(\mathbf{k}) = \frac{i\nu_i(1+\hat{\psi})}{2\hat{\psi}} \left[-1 \pm \sqrt{\frac{r+x}{2}} \pm isgn(y)\sqrt{\frac{r-x}{2}} \right] + \mathbf{V}_{i0} \cdot \mathbf{k}, \tag{2.7}$$

or, in terms of the growth rate and phase velocity:

$$\gamma = \frac{\nu_i(1+\hat{\psi})}{2\hat{\psi}} \left[-1 \pm \sqrt{\frac{r+x}{2}} \right], \tag{2.8}$$

$$V_{ph} = \frac{\nu_i(1+\hat{\psi})}{2\hat{\psi}k} sgn(y)\sqrt{\frac{r-x}{2}} + \frac{\mathbf{V}_{i0} \cdot \mathbf{k}}{k}. \tag{2.9}$$

From definitions (2.6), the following parity properties are obvious: $x(-\mathbf{k}) = x(\mathbf{k})$, $y(-\mathbf{k}) = -y(\mathbf{k})$ and hence $r(-\mathbf{k}) = r(\mathbf{k})$. Using those and equation (2.8), the growth rate is a symmetric function of $\mathbf{k}$: $\gamma(-\mathbf{k}) = \gamma(\mathbf{k})$. Similarly, the phase velocity is antisymmetric: $V_{ph}(-\mathbf{k}) = -V_{ph}(\mathbf{k})$. Equivalently, these two properties can be combined into a single expression

$$\omega(-\mathbf{k}) = -\omega^*(\mathbf{k}), \tag{2.10}$$

where asterisk represents the complex conjugate.

Overall, it was demonstrated in this section that a symmetry with respect to the reversal of the full wave vector $\mathbf{k}$ holds, even when the symmetry with respect to the component reversal ($\mathbf{k}_\parallel$ or $\mathbf{k}_\perp$) breaks. The numerical demonstration of this result was based on a robust solution of the general cubic dispersion relation and holds for any altitude. The analytic demonstration, on the other hand, is limited to the FBI case for nearly field-aligned irregularities as represented by the quadratic dispersion relation (2.3), and therefore is valid only for the E-region case. Importantly though, no further approximations to solutions (2.4) were needed, e.g. no need to use binomial expansion similar to that in Appendix 2.A. Thus, the analytic demonstration of the parity properties was performed for one limiting case that agreed with more general numerical demonstration.

The property (2.10) has been demonstrated by using an explicit expression for ω' (2.4) that is valid for FBI waves. It is important to note that the same property is valid in a more general case of real-valued waves in a physical medium, since the above Hermite symmetry under the inversion of the wavevector $\mathbf{k}$ is essential to guarantee real-valuedness of physical quantities [J. D. Sahr, personal communication, September 26, 2016].

2.7 Discussion

In this study, we examined solutions of the dispersion relation for the Farley-Buneman instability modified by the component of the background electric field parallel to the magnetic field. Numerical and analytic approaches were used to compare the growth rate and phase velocity at aspect angles of different polarities and to analyze the resulting asymmetries. Analysis of the previously unreported asymmetries represents a new application of the recently developed general formalism for electrostatic plasma instabilities [*Makarevich*, 2016a, b] and the developed analytic expressions provide a complete description of the specific problem of interest. Below we discuss factors that affect the asymmetry in solutions of the FBI dispersion relation, the origins of the background parallel electric field, and the implications for the experimental observations of the small-scale electrojet waves.

2.7.1 Electric Field Control of Asymmetry: Parallel versus Perpendicular Fields

The important new result of the current study is that the growth rate and phase velocity of FBI waves are perfectly symmetric with respect to the aspect angle reversal only for background electric fields $\mathbf{E}_0$ that are perfectly perpendicular to the magnetic field, Figures 2.2a and 2.2e. In case when the background electric field has a component parallel to the magnetic field $\mathbf{E}_{0\parallel}$, the growth rate and phase velocity become asymmetric around zero aspect angle, e.g. $\gamma(-\alpha) \neq \gamma(\alpha)$, Figures 2.2b–d, f–h.

Parallel electric fields have been previously demonstrated to modify numerical solutions to the FBI dispersion relation and the threshold criteria for the onset of the Farley-Buneman instability [*Chaturvedi et al.*, 1987]. In particular, it was demonstrated that, in the presence of parallel electric fields, the growth rate can become positive for nominally subcritical drifts and that the peak growth occurs at nonzero aspect angles [*Chaturvedi et al.*, 1987, Figure 1b]. This led to an important conclusion that obliquely propagating FBI waves can be excited for subcritical drift values. However, symmetry properties of solutions with respect to the aspect angle reversal have not been analyzed. In particular, *Chaturvedi et al.* [1987] have presented their results only for positive aspect angles. *Chaturvedi et al.* [1987] used a particular set of the parallel drift velocity $V_{d\parallel}$ values and for the current study we used the same $V_{d\parallel}$ values which were also converted to corresponding values of the background parallel electric field $E_{0\parallel}$. The maximum value of $V_{d\parallel} = 75\ C_s$ considered by *Chaturvedi et al.* [1987] translated to $E_{0\parallel} = 1.7$ mV/m and for this reason the range of $E_{0\parallel}$ used in

modeling presented in Figures 2.3 and 2.4 was chosen to be 0–1.5 mV/m.

One previous study has demonstrated that the presence of parallel density gradients in the ionosphere can result in asymmetry in the FBI growth rate, without appearing to change the perfect symmetry of the phase velocity [*Bahcivan and Cosgrove*, 2010, Figure 3]. In contrast, the present study has shown that parallel electric fields cause significant asymmetries in the phase velocity as well as in the growth rate.

Both of the above-cited studies that dealt with parallel components have employed numerical solutions to the FBI dispersion relation [*Chaturvedi et al.*, 1987; *Bahcivan and Cosgrove*, 2010]. In contrast, the current study has also derived explicit analytical expressions for the wave frequency in the presence of parallel electric fields and the resulting asymmetry. In order to do that, an approximate solution of the general dispersion relation was used, equation (2.12). This expression has a square root that needed to be expanded in order to extract the real and imaginary parts. In Appendix 2.A, an expansion of the fourth order was used, which gave the most similar form of the results for the asymmetry in the growth rate and phase velocity; compare Equations (2.17) and (2.18). The only difference between the part of the expressions in the square brackets are the numerical coefficients in front of different terms. This indicates that a background parallel electric field affects both real and imaginary parts of the solution to the dispersion relation in a similar manner.

The most important result of the current study is that the asymmetry in both the growth rate and phase velocity has a quasi-linear dependence on the background parallel electric field $E_{0\parallel}$. The dependence appeared to be exactly linear based on the numerical solutions at 110 km, Figure 2.3. Analytic analysis in Appendix 2.A revealed that the linearity or proportionality to the factor $\mathbf{V}_d \cdot \mathbf{k}_\parallel$ and hence to $E_{0\parallel}$ will be observed, as long as higher order terms $\propto \left(\mathbf{V}_d \cdot \mathbf{k}_\parallel\right)^3$ in Equations (2.17) and (2.18) are small.

It was also realized that other factors, notably the propagation direction relative to convection, or the flow angle θ, also affect the asymmetry without necessarily affecting the linearity. This was seen from different slopes for different flow angles in Figure 2.3a. Analytic analysis presented in Appendix 2.A revealed that this dependence is due to the factor $\mathbf{V}_d \cdot \mathbf{k}_\perp = V_d k \cos\theta$, which is related to $\mathbf{E}_{0\perp}$. After this primary flow angle effect has been removed, both the growth rate and phase velocity had a *similar and linear* dependence on $E_{0\parallel}$, Figures 2.3b and 2.3c.

The flow angle or, equivalently, perpendicular electric fields $\mathbf{E}_{0\perp}$ also affected the asymmetry in a more subtle way. That is, the secondary effect of flow angle variation was seen

in the form of a spread in both normalized growth rate and the phase velocity, Figures 2.3b and 2.3c. The spread was relatively small; in terms of slopes it was $\sim 1/3$ for the growth rate and $\sim 1/6$ for the phase velocity. The origin of the spread was the higher order terms $\propto (\mathbf{V}_d \cdot \mathbf{k}_\perp)^2$ in Equations (2.17) and (2.18). A comparison of analytic results obtained using a square root expansion to the fourth order with the more general numerical solutions has demonstrated that the magnitude of the spread was well reproduced, compare black area with the spread of the colored lines in Figures 2.3b and 2.3c. The leading term in the analytic expression for the asymmetry also matched well with the upper limit on the spread in the numerical solutions. We have also conducted an additional analysis involving asymmetry comparisons using the full square root expression (2.12) with numerical solutions of the more general cubic equation and obtained a perfect agreement (not presented here). This implies that if one expands the root of the approximate solution (2.12) using an even larger number of terms, the spread between the numerical and analytic results in Figures 2.3b and 2.3c should match even closer.

Finally, the asymmetry analysis at higher altitudes showed a somewhat different picture. The apparent nonlinearity of the asymmetry at an altitude of 120 km, i.e. in the transitional region between the E and F layers of the ionosphere, was demonstrated in Figures 2.4c and 2.4f. The numerical part of the analysis was based on a robust technique of solving the cubic form of the general dispersion relation developed by *Makarevich* [2016b]. The solution to this general dispersion relation does not use any assumptions based on the altitude. The quadratic FBI dispersion relation, which was used to produce the analytic estimates of the asymmetry in Figures 2.3b and 2.3c, is a limiting case for the general cubic dispersion relation, where the assumptions based on the altitude were applied to reduce the order of the equation from third to second [*Makarevich*, 2016b]. Importantly, the quadratic FBI dispersion relation stops reproducing the results of the general cubic dispersion relation at altitudes above the E region peak [*Makarevich*, 2016b]. Therefore, the nonlinearity of the asymmetry is not due to an insufficient number of terms in the expansion of the square root, but due to the fact that the square root expression (2.12) itself is no longer an approximate solution of the cubic dispersion equation at higher altitudes. Moreover, a general solution can no longer be described by any expansion with progressively smaller terms, similar to that in equation (2.14).

The overall conclusion from this part of the analysis is that the effect of parallel electric fields $E_{0\parallel}$ is linear near the E-region peak, with the higher order terms being negligible. The

effect of perpendicular electric fields $\mathbf{E}_{0\perp}$ is two-fold. The primary effect is a large spread in the growth rate asymmetry due to the flow angle variation, whereas the secondary effect is a smaller spread in both the growth rate and phase velocity. At higher altitudes, the effect is no longer linear with $E_{0\parallel}$, due to a transition to a regime where solutions of the general dispersion relation are no longer described by an expansion similar to a binomial one.

2.7.2 Parallel Electric Field versus Parallel Density Gradient

In this section, the effects of the parallel electric field are considered together with the effects of the parallel electron density gradient. The latter group of effects on 50-m FBI waves were previously considered by *Bahcivan and Cosgrove* [2010], and in the following analysis we attempt to reproduce their results while also addressing the issue of relative importance of these two groups of effects for both 50- and 10-m waves.

Numerical solutions of the general dispersion relation [*Makarevich*, 2016a] were used to produce Figure 2.7. The first row shows the (a) normalized growth rate γ/k and (b) the phase velocity modified by the parallel electric field and density gradient for 50-m waves at the flow angle of 0°. The second row presents the same information but for 10-m waves. In all panels, the color of the lines indicates the magnitude of the parallel electric field, with the legend given in Figure 2.7b. The solid lines represents the gradient-free case, whereas dashed lines show the results for the parallel electron density gradient scale $L_{\parallel} = n/(\nabla_{\parallel} n)$ of 1 km. This gradient scale value was the strongest gradient considered by *Bahcivan and Cosgrove* [2010], while parallel electric field values are the same as those in our previous analyses, e.g. Figure 2.2. A comparison with the results presented by *Bahcivan and Cosgrove* [2010] shows a very good agreement, e.g. compare the dotted dark blue line in the current Figure 2.7a with the inverted dashed line from Figure 3 (first row) of *Bahcivan and Cosgrove* [2010].

The current analysis reveals new features as well. The parallel density gradient modifies the growth rate of 50-m waves much stronger than the parallel background electric field, with the dotted lines in Figure 2.7a being much higher than their solid counterparts. This is clearly not the case however for the phase velocity, with the dotted lines in Figure 2.7b barely deviating from the solid lines which themselves shift noticeably. Interestingly, an increase in the parallel electric field does not shift much positions of the peaks and troughs, but changes significantly their magnitude. The effect of the parallel gradient is significantly weaker for 10-m waves, and the modification is very similar to the one that the parallel electric field produces, Figure 2.7c.

Overall, this analysis shows that relative importance of these two groups of effects on the growth rate changes significantly with the wavelength, with much smaller parallel gradient effects on 10-m waves, and that parallel electric field effects on the phase velocity dominate regardless on the wavelength.

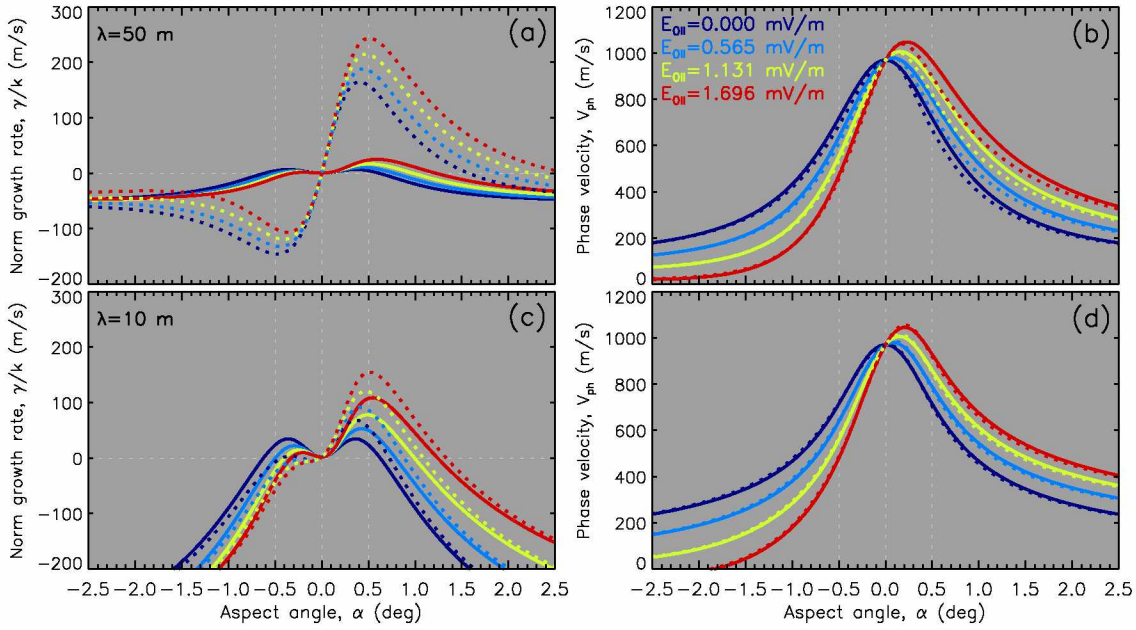

Figure 2.7. Combined effects of the parallel electric field and electron gradient at zero flow angle on the (a) normalized growth rate γ/k and (b) phase velocity of 50-m waves for 4 values of the parallel electric field $E_{0\parallel}$ indicated by the color. The plasma drift speed is $V_E = 1000$ m/s. Results with (without) parallel density gradient of 1-km scale are shown by the dotted (solid) lines. Panels (c) and (d) show results for 10-m waves.

2.7.3 Parallel Electric Fields: Origins and Expected Magnitudes

Essential for the present study is the presence of background parallel electric fields $E_{0\parallel}$. A related issue is that the $E_{0\parallel}$ magnitudes should be large enough for the expected asymmetry effects to be observable experimentally. For example, the phase velocity asymmetries of 30–300 m/s are expected for parallel electric fields of 0.1–1.0 mV/m and for the aspect angle sample points of ±0.5°, Figure 2.3c. An even greater asymmetry is observed at higher altitudes, Figure 2.4e. It is therefore important to understand both the origins of parallel electric fields in the ionosphere and what $E_{0\parallel}$ magnitudes can be reasonably expected at least under some, not-too-exotic conditions.

The nature of the parallel electric fields in the magnetosphere is still an open question,

with formation of auroral arcs in particular often involving substantial changes in the electric potential along the magnetic field [e.g. Chapter 3 of *Paschmann et al.*, 2002]. In the lower ionosphere, the issue is also far from being resolved. An early modeling study by *Nakada* [1987] demonstrated that the parallel electric field in the E region of the ionosphere can arise under the influence of several factors, such as the thickness of current sheets along the magnetic field, reduction of the parallel conductivities, and strong neutral winds in the conjugate hemispheres. According to *Nakada* [1987], a parallel electric field at 110 km can have a magnitude of 0.062 mV/m and can reach the value of 14.4 mV/m at an altitude of 135 km. A comprehensive discussion of two major generation mechanisms for $E_{0\|}$ in the ionosphere has been given more recently by *St.-Maurice et al.* [1996].

The first mechanism, which was originally proposed by *Rietveld et al.* [1991], involves the ambient electric field between the magnetosphere and the ionosphere and a beam of soft electrons accelerated in the lower magnetosphere. The beam electrons collide inelastically with neutrals and stop at the deposition altitude in the upper F region. Due to the fact that the total current divergence has to be zero, the current continuity forces thermal electrons to carry the field-aligned current that was originally carried by the beam electrons. In the region where the beam electrons become collisional and dissipate their current, parallel electric fields are generated that partially cancel the ambient electric field between the deposition altitude and $\sim$ 250 km and amplify the ambient electric filed below 250 km [*Rietveld et al.*, 1991, Figure 12]. Produced parallel electric fields should be intense enough to ensure current continuity. In extreme cases, when the horizontal conductivity is very poor, the parallel field is strong enough so that the thermal electrons carry roughly the same currents as the beam electrons below the dissipation region [*Rietveld et al.*, 1991].

Another generation mechanism was proposed by *St.-Maurice et al.* [1996] which does not depend directly on intense precipitation of beam electrons. Instead, it is powered by intense horizontal conductivity gradients in the presence of a large-scale ambient perpendicular electric field. Conductivity gradients initially cause an accumulation of charge that prevents the original current from being free of divergence at the boundary between two regions with different conductivities. This results in the generation of local electric fields in both the parallel and perpendicular directions. Parallel electric fields will intensify when a considerable jump or a sheer in the ambient perpendicular electric field is added and/or when an instability with a weaker threshold than the ion-acoustic instability is triggered first to modify the electrical conductivity on one side of the gradients [*St.-Maurice et al.*,

1996]. In this mechanism, relatively small (100-m) horizontal gradient scales were found to be essential [*St.-Maurice et al.*, 1996].

In both mechanisms, it was concluded that parallel electric field can reasonably be on the order of 0.1 mV/m in the lower ionosphere and that it can be significantly higher when strong turbulence is produced by the ion-acoustic instability in the nonlinear regime. Both generating mechanisms could also work in tandem, resulting in greater parallel electric fields [*St.-Maurice et al.*, 1996]. The important implication for the current study is that parallel electric fields of 0.1 mV/m can be considered as moderate, while stronger fields up to 1.0 mV/m are possible in cases involving either extremely small gradient scales and/or the ion-acoustic instability operating in the nonlinear regime.

2.7.4 Parallel Electric Fields: Indirect Evidence from Asymmetries

Sahr and Fejer [1996] in their review of electrojet irregularity theory and experiment listed the issue of the parallel electric field measurements among most promising avenues for future studies concluding that "This is a very difficult measurement to make; it should be made". This conclusion remains valid today. Even though direct measurements remain challenging to perform, signatures of parallel electric fields can be observed through indirect evidence such as intense field-aligned currents and horizontal sheers [*St.-Maurice et al.*, 1996]. In the current study, it is demonstrated that asymmetries in the irregularity characteristics with respect to aspect angle reversal can potentially be used as another indirect piece of evidence.

In particular, asymmetry in the Doppler velocity of coherent radar echoes can be potentially used for this purpose or, at the very least, with the predicted features in mind, as described below. Coherent radars within the Super Dual Auroral Radar Network (SuperDARN) measure irregularity phase velocity very accurately (with uncertainty of less than about 1%). Many of the high-southern-latitude SuperDARN radars including radars at the South Pole, McMurdo, Dome Concordia, and Syowa Antarctic stations have aspect angles of different polarity within their E-region fields-of-view (FoVs) [*Makarevich et al.*, 2015; *Forsythe and Makarevich*, 2015]. The phase velocity along the same radar beam can be examined as a function of the aspect angle [*Ogawa et al.*, 1980; *Nielsen*, 1986; *Kustov et al.*, 1994; *Makarevich et al.*, 2006, 2007]. In cases when the plasma drift is uniform in the F region above the radar's FoV and when the elevation angle data are available to ensure the arrival of the signal from the same E-region height, it may be possible to detect the

asymmetry in phase velocity around zero aspect angle.

Several complications need to be addressed in this regard, one of which is the uniformity of the convection velocity $\mathbf{V}_E$ along the radar beam. The best chance to ensure this is offered by modes with high range resolution (e.g. 15-km modes vs more common 45-km modes for SuperDARN). In this case and for typical aspect angle variations with range, the aspect angles of interest $[-0.5°, +0.5°]$ will be spread over $\sim$10 range gates or 150 km. Thus one will need to ensure uniformity of the convection velocity along a distance of 150 km, which is possible to do within 100 m/s. Another complication is the precise aspect angle estimation for each slant range gate. Even if the elevation angle of the signal arrival is available, information about electron densities is required for the raytracing simulations as further elaborated below.

Another experiment that could provide evidence for parallel electric field would require the operation of a HF radar in an alternating frequency mode. Every time a HF radar receives an E region echo with a particular phase velocity, it samples the aspect angle cone of a particular polarity at a particular flow angle, Figure 2.6b. One way to take a measurement of the phase velocity at the opposite aspect angles would be by changing the sounding frequency, which would result in slightly different ray paths sampling the opposite aspect angles. The complication regarding uniformity of the convection flow is much less relevant for this particular experiment. This is because, at these ranges, the radar would sample the same spatial location within $\sim$ 5–10 km [*Chisham et al.*, 2008; *Yeoman et al.*, 2008].

Both experiments proposed above require information on aspect angles. Instead of using geometric aspect angles, i.e. those that do not take into account the electron density of the ionosphere and therefore do not correct for the refraction, the International Reference Ionosphere model can be used to obtain the electron density in the radar's FoV. The modeled densities then could be used in raytracing simulations to estimate the aspect angles at E-region altitudes. The availability of direct and, preferably, multi-point density measurements such as those provided by ionosondes or incoherent scatter radars would also significantly increase the accuracy of the proposed estimates and inferred asymmetries.

The overall conclusion about the observability of the predicted asymmetries with coherent radars is that these effects are more likely to be seen closer to the top of the considered range $E_{0\parallel} = 0.1$–1.0 mV/m, i.e. considering velocity differences of $\sim$ 300 m/s at $\alpha = \pm 0.5°$ and 110 km. Larger aspect angles and/or higher altitudes as well as smaller radar range

resolution and more accurate density measurements can enable effective sampling of the parallel electric fields closer to the middle of this range and perhaps down to the lower end. It is nearly certain though that anything less than $E_{0\parallel} = 0.1$ mV/m will be too small to produce measurable asymmetries.

Finally, parallel electric fields in their AC or wave perturbation form are considered to be essential for generating intense electron heating events in the E region also known as anomalous electron heating [*Schlegel and St.-Maurice*, 1981; *St.-Maurice et al.*, 1981; *Milikh and Dimant*, 2003; *Bahcivan*, 2007; *Bahcivan and Cosgrove*, 2010; *Oppenheim and Dimant*, 2013; *Makarevich et al.*, 2013]. *Bahcivan and Cosgrove* [2010] argued that parallel density gradients can indirectly contribute to this process. In this scenario, parallel density gradients modify the threshold value of the aspect angle in the Farley-Buneman dispersion relation, resulting in a higher threshold electric field for FBI, which in turn intensifies both components of the AC electric fields. The implication of the current study is that the threshold value of the aspect angle can also be modified by the background parallel electric field, and therefore be part of the same mechanism and contribute to the anomalous electron heating.

2.8 Summary and Conclusions

Analysis of the general dispersion relation that describes fundamental ionospheric instabilities including the Farley-Buneman instability focusing on the symmetry properties with respect to a reversal of the wave propagation components parallel and perpendicular to the magnetic field showed the following.

1. The FBI dispersion relation and its solutions for the growth rate and phase velocity are symmetric with respect to the reversal of the parallel propagation component $\mathbf{k}_\parallel$ only in case when the background electric field is perfectly perpendicular to the magnetic field.

2. A background parallel electric field causes asymmetry in solutions of the general dispersion relation in terms of the complex wave frequency ω when one component is reversed and the other component is fixed, i.e. $\omega(\mathbf{k}_\perp, -\mathbf{k}_\parallel) \neq \omega(\mathbf{k}_\perp, \mathbf{k}_\parallel)$ and $\omega(-\mathbf{k}_\perp, \mathbf{k}_\parallel) \neq \omega(\mathbf{k}_\perp, \mathbf{k}_\parallel)$.

3. Near the E-region peak altitude of 110 km, the asymmetry in the growth rate and phase velocity is a linearly increasing function of the background parallel electric field and has a spread in slope due to different perpendicular propagation directions $\mathbf{k}_\perp$, with a nonlinear dependence above 120 km.

4. Analytic solutions to the FBI dispersion relation have a parity property for the complex wave frequency $\omega(-\mathbf{k}) = -\omega^*(\mathbf{k})$ for all values of the parallel electric field, which means that the symmetry with respect to a reversal of the full wave vector $\mathbf{k}$ holds, even when the symmetry with respect to component reversal ($\mathbf{k}_\parallel$ or $\mathbf{k}_\perp$) breaks. The same result was demonstrated numerically using a robust solution of the cubic dispersion relation that holds for any altitude.

5. Moderate-to-strong parallel electric fields of 0.1–1.0 mV/m can result in experimentally measurable differences between the characteristics of plasma waves with parallel propagation components of opposite polarity.

2.9 References

Bahcivan, H. (2007), Plasma wave heating during extreme electric fields in the high-latitude E region, *Geophys. Res. Lett.*, *34*, L15106, doi:10.1029/2006GL029236.

Bahcivan, H., and R. Cosgrove (2010), On the generation of large wave parallel electric fields responsible for electron heating in the high-latitude E region, *J. Geophys. Res.*, *115*(A10), doi:10.1029/2010JA015424.

Buneman, O. (1963), Excitation of field-aligned sound waves by electron streams, *Phys. Rev. Lett.*, *10*, 285–287.

Chaturvedi, P. K., J. D. Huba, S. L. Ossakow, P. Satyanarayana, and J. A. Fedder (1987), Parallel current effects on two-stream electrojet plasma instabilities, *J. Geophys. Res.*, *92*, 8700–8706.

Chisham, G., T. K. Yeoman, and G. J. Sofko (2008), Mapping ionospheric backscatter measured by the SuperDARN HF radars - Part 1: A new empirical virtual height model, *Ann. Geophysicae*, *26*, 823–841.

Ecklund, W. L., B. B. Balsley, and R. A. Greenwald (1975), Crossed beam measurements of the diffuse radar aurora, *J. Geophys. Res.*, *80*, 1805–1809.

Farley, D. T. (1963), A plasma instability resulting in field-aligned irregularities in the ionosphere, *J. Geophys. Res.*, *68*, 6083–6093.

Fejer, B. G., and M. C. Kelley (1980), Ionospheric irregularities, *Geophys. Rev.*, *18*, 401–454.

Forsythe, V. V., and R. A. Makarevich (2015), Dual radar investigation of E region plasma waves in the southern polar cap, *J. Geophys. Res. Space Physics*, *120*(10), 9132–9147, doi:10.1002/2015JA021664.

Foster, J. C., D. Tetenbaum, C. F. del Pozo, J.-P. St-Maurice, and D. R. Moorcroft (1992), Aspect angle variations in intensity, phase velocity and altitude for high-latitude 34 cm *E* region irregularities, *J. Geophys. Res.*, *97*, 8601–8617.

Gorin, J. D., A. V. Koustov, R. A. Makarevich, J.-P. S. Maurice, and S. Nozawa (2012), Velocity of E-region HF echoes under strongly-driven electrojet conditions, *Ann. Geophysicae*, *30*, 235–250, doi:10.5194/angeo-30-235-2012.

Hedin, A. E. (1991), Extension of the MSIS thermospheric model into the middle and lower atmosphere, *J. Geophys. Res.*, *96*, 1159–1172.

Koehler, J. A., G. J. Sofko, and V. Mehta (1985), A statistical study of magnetic aspect effects associated with VHF auroral backscatter, *Radio Sci.*, *20*, 689–695.

Kustov, A. V., M. V. Uspensky, G. J. Sofko, J. A. Koehler, and J. Mu (1994), Aspect angle dependence of the radar aurora Doppler velocity, *J. Geophys. Res.*, *99*, 2131–2144.

Makarevich, R. A. (2016a), Toward an integrated view of ionospheric plasma instabilities: Altitudinal transitions and strong gradient case, *J. Geophys. Res. Space Physics*, *121*, 3634–3647, doi:10.1002/2016JA022515.

Makarevich, R. A. (2016b), Toward an integrated view of ionospheric plasma instabilities: 2. Three inertial modes of a cubic dispersion relation, *J. Geophys. Res. Space Physics*, doi:10.1002/2016JA022864.

Makarevich, R. A., A. Senior, A. V. Koustov, M. V. Uspensky, F. Honary, and P. L. Dyson (2006), A study of aspect angle effects in the *E*-region irregularity velocity using multi-point electric field measurements, *Geophys. Res. Lett.*, *33*, L21102, doi:10.1029/2006GL027740.

Makarevich, R. A., A. V. Koustov, A. Senior, M. Uspensky, F. Honary, and P. L. Dyson (2007), Aspect angle dependence of the E-region irregularity velocity at large flow angles, *J. Geophys. Res.*, *112*, A11303, doi:10.1029/2007JA012342.

Makarevich, R. A., A. V. Koustov, and M. J. Nicolls (2013), Poker Flat Incoherent Scatter Radar observations of anomalous electron heating in the E region, *Ann. Geophysicae*, *31*(7), 1163–1176.

Makarevich, R. A., V. V. Forsythe, and A. C. Kellerman (2015), Electric field control of E region coherent echoes: Evidence from radar observations at the South Pole, *J. Geophys. Res. Space Physics*, *120*, 2148–2165, doi:10.1002/2014JA020844.

Milikh, G. M., and Y. S. Dimant (2003), Model of anomalous electron heating in the E region: 2. Detailed numerical modeling, *J. Geophys. Res.*, *108*, 1351, doi:10.1029/2002JA009527.

Nakada, M. P. (1987), Parallel electric fields from ionospheric winds, *J. Geophys. Res.*, *92*(A10), 11,248–11,252.

Nielsen, E. (1986), Aspect angle dependence of mean Doppler velocities of 1-m auroral plasma waves, *J. Geophys. Res.*, *91*, 10,173–10,177.

Ogawa, T., B. B. Balsley, W. L. Ecklund, D. A. Carter, and P. E. Johnston (1980), Aspect angle dependence of irregularity phase velocities in the auroral electrojet, *Geophys. Res. Lett.*, *7*, 1081–1084.

Oppenheim, M. M., and Y. S. Dimant (2013), Kinetic simulations of 3-D Farley-Buneman turbulence and anomalous electron heating, *J. Geophys. Res.*, *118*, 1306–1318, doi:10.1002/jgra.50196.

Paschmann, G., S. Haaland, and R. Treumann (2002), Auroral Plasma Physics, *Space Sci. Rev.*, *103*(1), 41–92, doi:10.1023/A:1023030716698.

Pfaff, R. F., M. C. Kelley, B. G. Fejer, E. Kudeki, C. W. Carlson, A. Pedersen, and B. Hausler (1984), Electric field and plasma density measurements in the auroral electrojet, *J. Geophys. Res.*, *89*, 236–244.

Rietveld, M. T., P. N. Collis, and J.-P. St.-Maurice (1991), Naturally enhanced ion acoustic waves in the auroral ionosphere observed with the EISCAT 933-MHz radar, *J. Geophys. Res.*, *96*(A11), 19,291–19,305.

Sahr, J., and B. G. Fejer (1996), Auroral electrojet plasma irregularity theory and experiment: A critical review of present understanding and future directions, *J. Geophys. Res.*, *101*, 26,893–26,909.

Schlegel, K., and J.-P. St.-Maurice (1981), Anomalous heating of the polar E region by unstable plasma waves. 1. Observations, *J. Geophys. Res.*, *86*, 1447–1452.

Schunk, R. W., and A. F. Nagy (1978), Electron temperatures in the F region of the ionosphere: Theory and observations, *Rev. Geophys. Space Phys.*, *16*, 355–399.

Schunk, R. W., and A. F. Nagy (1980), Ionospheres of the terrestrial planets, *Rev. Geophys. Space Phys.*, *18*, 813–852.

St.-Maurice, J.-P., K. Schlegel, and P. M. Banks (1981), Anomalous heating of the polar E region by unstable plasma waves. 2. Theory, *J. Geophys. Res.*, *86*, 1447–1452.

St.-Maurice, J.-P., W. Kofman, and D. James (1996), In situ generation of intense parallel electric fields in the lower ionosphere, *J. Geophys. Res.*, pp. 335–356.

Yeoman, T. K., G. Chisham, L. J. Baddeley, R. S. Dhillon, T. J. T. Karhunen, T. R. Robinson, A. Senior, and D. M. Wright (2008), Mapping ionospheric backscatter measured by the SuperDARN HF radars - Part 2: Assessing SuperDARN virtual height models, *Ann. Geophysicae*, *26*, 843–852.

2.A Analytic Evaluation of Asymmetries at Opposite Aspect Angles

In this section, analytic expressions that quantify the asymmetries in the growth rate γ and the phase velocity V_{ph} as functions of the parallel electric field $E_{0\parallel}$ are derived. In this context, the asymmetry is defined as the difference between the solutions for positive and negative parallel component of the wave vector $\mathbf{k}_\parallel$, e.g. the growth rate asymmetry is defined as $\gamma(\mathbf{k}_\parallel) - \gamma(-\mathbf{k}_\parallel)$.

The growth rate and the phase velocity can be obtained from the complex wave frequency $\omega = \omega_r + i\gamma$, which is, in turn, related to the complex quantity D_i through

$$D_i = -i\Omega_i^{-1}(\omega - \mathbf{k}\cdot\mathbf{V}_{i0}) + r_i, \tag{2.11}$$

where r_i is the ratio between the collision frequency of ions with neutrals ν_i and ion gyrofrequency $\Omega_i \equiv |e|B/m_i$ and $\mathbf{V}_{i0}$ is the background drift velocity of ions.

In the E region, an approximate solution of a general dispersion relation is given by equation (17) of *Makarevich* [2016b] which for our gradient-free case reduces to

$$D_i = \frac{r_i}{2\hat{\psi}}\left[\hat{\psi} - 1 + \sqrt{(1+\hat{\psi})^2 - 4i\hat{\psi}r_i^{-1}\hat{W}}\right], \tag{2.12}$$

with $\hat{W} = \Omega_i^{-1}\left(\mathbf{V}_d\cdot\mathbf{k} - i\hat{\psi}r_i^{-1}Ck_\perp^2\right)$. In these notations, $\hat{\psi} = -r_i r_e\left(1 + r_e^{-2}\tan^2\alpha\right)$ is the anisotropy factor, $r_e \equiv \nu_e/\Omega_e$ is the ratio of collision frequency and the gyrofrequency for electrons, $\mathbf{V}_d = \mathbf{V}_{e0} - \mathbf{V}_{i0}$ is the differential plasma drift velocity, $\mathbf{k} = \mathbf{k}_\parallel + \mathbf{k}_\perp$ is the wavevector, and $C \equiv (T_i + T_e)/B/|e|$ is related to the ion-acoustic speed C_s through $C = C_s^2/\Omega_i$.

The square root in Equation (2.12) can be expanded to the fourth order using binomial approximation $\sqrt{1+x} = 1 + x/2 - x^2/8 + x^3/16 - 5x^4/128$

$$\begin{aligned} D_i &= \frac{r_i}{2\hat{\psi}}\left[\hat{\psi} - 1 + (\hat{\psi}+1)\sqrt{1 - \frac{4i\hat{\psi}\hat{W}}{r_i(1+\hat{\psi})^2}}\right] \approx \\ &\approx r_i - \frac{i\hat{W}}{1+\hat{\psi}} + \frac{\hat{\psi}\hat{W}^2}{r_i(1+\hat{\psi})^3} + \frac{2i\hat{\psi}^2\hat{W}^3}{r_i^2(1+\hat{\psi})^5} - \frac{5\hat{\psi}^3\hat{W}^4}{r_i^3(1+\hat{\psi})^7}. \end{aligned} \tag{2.13}$$

Alternatively, the wave frequency ω can be written as

$$\omega = \frac{\Omega_i\hat{W}}{1+\hat{\psi}} + \frac{i\Omega_i\hat{\psi}\hat{W}^2}{r_i(1+\hat{\psi})^3} - \frac{2\Omega_i\hat{\psi}^2\hat{W}^3}{r_i^2(1+\hat{\psi})^5} - \frac{5i\Omega_i\hat{\psi}^3\hat{W}^4}{r_i^3(1+\hat{\psi})^7} + \mathbf{V}_{i0}\cdot\mathbf{k}. \tag{2.14}$$

In order to simplify the derivation, the following notations are introduced: $a \equiv \mathbf{V}_d\cdot\mathbf{k}_\perp$, $b \equiv \mathbf{V}_d\cdot\mathbf{k}_\parallel$, and $c \equiv -i\hat{\psi}r_i^{-1}Ck_\perp^2$. In these notations, $\hat{W} = \Omega_i^{-1}(a+b+c)$ and Equation

(2.14) is rewritten as

$$\omega = \frac{a+b+c}{1+\hat{\psi}} + \frac{i\hat{\psi}(a+b+c)^2}{\nu_i(1+\hat{\psi})^3} - \frac{2\hat{\psi}^2(a+b+c)^3}{\nu_i^2(1+\hat{\psi})^5} - \frac{5i\hat{\psi}^3(a+b+c)^4}{\nu_i^3(1+\hat{\psi})^7} + \mathbf{V}_{i0}\cdot\mathbf{k}. \quad (2.15)$$

For the evaluation of the asymmetry $\omega(\mathbf{k}_\parallel) - \omega(-\mathbf{k}_\parallel)$, it is useful to note that only the term b changes sign with the reversal of $\mathbf{k}_\parallel$. With that, the asymmetry in the wave frequency takes the form

$$\begin{aligned}\omega(\mathbf{k}_\parallel) - \omega(-\mathbf{k}_\parallel) = \frac{2b}{1+\hat{\psi}}\Bigg[1 + \frac{2i\hat{\psi}(a+c)}{\nu_i(1+\hat{\psi})^2} - \frac{2\hat{\psi}^2(b^2+3a^2+3c^2+6ac)}{\nu_i^2(1+\hat{\psi})^4} - \\ - \frac{20i\hat{\psi}^3(a^3+ab^2+b^2c+c^3+3a^2c+3ac^2)}{\nu_i^3(1+\hat{\psi})^6}\Bigg] + 2\mathbf{V}_{i0}\cdot\mathbf{k}_\parallel.\end{aligned} \quad (2.16)$$

Extracting the imaginary part of the wave frequency ω and substituting back the definitions of a, b and c, the asymmetry in the growth rate γ is expressed as

$$\begin{aligned}\gamma(\mathbf{k}_\parallel) - \gamma(-\mathbf{k}_\parallel) = \\ \frac{4\hat{\psi}\mathbf{V}_d\cdot\mathbf{k}_\perp\mathbf{V}_d\cdot\mathbf{k}_\parallel}{\nu_i(1+\hat{\psi})^3}\left[1 + \frac{6\hat{\psi}^2 r_i^{-1}Ck_\perp^2}{\nu_i(1+\hat{\psi})^2} - \frac{10\hat{\psi}^2\left((\mathbf{V}_d\cdot\mathbf{k}_\perp)^2 + (\mathbf{V}_d\cdot\mathbf{k}_\parallel)^2 - 3\hat{\psi}^2 r_i^{-2}C^2k_\perp^4\right)}{\nu_i^2(1+\hat{\psi})^4}\right].\end{aligned} \quad (2.17)$$

The asymmetry in the phase velocity is found by extracting the real part of the asymmetry in ω, neglecting the fourth order terms, and and dividing by k

$$\begin{aligned}V_{ph}(\mathbf{k}_\parallel) - V_{ph}(-\mathbf{k}_\parallel) = \\ \frac{2\mathbf{V}_{i0}\cdot\mathbf{k}_\parallel}{k} + \frac{2\mathbf{V}_d\cdot\mathbf{k}_\parallel}{k(1+\hat{\psi})}\left[1 + \frac{2\hat{\psi}^2 r_i^{-1}Ck_\perp^2}{\nu_i(1+\hat{\psi})^2} - \frac{2\hat{\psi}^2\left((\mathbf{V}_d\cdot\mathbf{k}_\parallel)^2 + 3(\mathbf{V}_d\cdot\mathbf{k}_\perp)^2 - 3\hat{\psi}^2 r_i^{-2}C^2k_\perp^4\right)}{\nu_i^2(1+\hat{\psi})^4}\right].\end{aligned} \quad (2.18)$$

The two asymmetry expressions (2.17) and (2.18) are nicely similar in their form, with terms in brackets only differing in integer coefficients. For both, the leading term in brackets is simply one. The second leading term is positive and larger for the growth rate by the exact factor of 3. The growth rate asymmetry is proportional to two factors $\mathbf{V}_d\cdot\mathbf{k}_\perp$ and $\mathbf{V}_d\cdot\mathbf{k}_\parallel$, while the phase velocity is proportional to $\mathbf{V}_d\cdot\mathbf{k}_\parallel$ and, in the neutral frame, shifted by a similar factor involving the ion velocity $\mathbf{V}_{i0}$. Since both $V_{i0\parallel}$ and $V_{d\parallel}$ are proportional

to the parallel electric field $E_{0\parallel}$, both dependencies are linear with $E_{0\parallel}$ to the second order. The growth rate asymmetry can be normalized by the common factor $\mathbf{V}_d \cdot \mathbf{k}_\perp = V_d k_\perp \cos\theta$, to reduce the dependence on the flow angle θ, whereas the phase velocity asymmetry does not need this additional normalization. The last term in brackets in both (2.17) and (2.18) contain terms $(\mathbf{V}_d \cdot \mathbf{k}_\perp)^2$ and $\left(\mathbf{V}_d \cdot \mathbf{k}_\parallel\right)^2$ which respectively introduce additional spread due to the flow angle variation and nonlinearity with $E_{0\parallel}$, but their contribution is relatively small due to the smallness of the factor $\hat{\psi}^2$. The contribution and effects of these terms in the total asymmetries are further examined in section 2.4 where the results are also compared with those produced using numerical solutions of the more general cubic dispersion relation.

Acknowledgements

This work was supported by National Science Foundation grants PLR-1139806 and PLR-1443504. The MSISE-90 model is available from the Goddard Space Flight Center Space Physics Data Facility OMNIWeb interface at http://omniweb.gsfc.nasa.gov/. The authors are grateful for discussions with J.-P. St.-Maurice, J. Sahr, and P. Delamere.

Chapter 3
Observational Techniques and Models

In this chapter, the primary observational technique used in the experimental part of this body of work is introduced, as well as computational models that complemented the primary technique. The network of coherent HF radars, SuperDARN, is introduced in Section 3.1, where a general overview of SuperDARN is presented, followed by technical aspects of operation, derivation of spectral parameters, and data post-processing techniques. The "Map Potential" technique, used for production of the ionospheric convection patterns is also discussed. In addition, the raytracing technique and the virtual height model are introduced to better understand the geometry of the region from where radars receive the backscatter. Sections 3.2 introduces the Defence Meteorological Space Program (DMSP) satellites that have an Ion Drift Meter (IDM) sensor onboard used in this research to provide an additional estimate of the plasma convection component. The International Reference Ionosphere (IRI) and the Mass Spectrometer and Incoherent Scatter (MSIS) models that are used in this research to estimate the concentrations of plasma and neutral particles are introduced in Sections 3.3 and 3.4, respectively.

3.1 Super Dual Auroral Radar Network

3.1.1 General Overview

The Super Dual Auroral Network (SuperDARN) is a network of similar ground-based radars that cover a wide range of latitudes in the northern and southern hemispheres. The network was designed with a primary scientific aim of monitoring the global dynamical processes in the ionosphere, most notably the plasma convection.

A typical SuperDARN radar comprises a main array of 16 log-periodic antennas which transmits and receives radio signals in the high frequency (HF) range from 8 to 20 MHz and a secondary interferometer array of 4 antennas that can be used to determine the elevation angle of the backscattered signal. The radar beam of the main array steers electronically by changing the phase of the signal between the antennas, thus performing a scan in the azimuthal extent of about 52°. The transmitted pulse length controls the range resolution and allows to sample the ionosphere along the line-of-sight of each steering position in the range extent from 180 km to more than 3000 km; in the common mode of operation the range resolution is 45 km.

Figure 3.1 illustrates the main principles behind the SuperDARN operations. Shown is

the field-of-view (FoV) of the first SuperDARN radar that was deployed in October 1983 at Goose Bay, Canada [*Greenwald et al.*, 1985].

Soon after the Goose Bay radar started its operation, it was recognized that in order to determine the full two-dimensional velocity vector, the second radar is required to overlook the same FoV from a different direction. This is because each radar measures only one component of the plasma drift velocity along its line-of-sight (LOS) or LOS velocity. Consequently, in October 1989 the second radar was deployed in Schefferville, Canada. Together with the radar at Goose Bay it provided a stereoscopic capability of observation. Using the standard SuperDARN three-letter radar codes [*Chisham et al.*, 2007], the radar at Goose Bay is referred to as GBR. Combining LOS velocities measured by GBR and Schefferville (orange and green vectors in Figure 3.1), the full two-dimensional velocity vector (black vector in Figure 3.1) can be found using the so called "Merge" technique [*Hanuise et al.*, 1993]. This technique combines two LOS velocity measurements from the same location into a single 2D Merge vector, that is formed from the intersection of 2 lines orthogonal to the LOS vectors (see Figure 3.1). Using this technique, *Hanuise et al.* [1993] reported the first observation of the instantaneous two-dimensional flows using GBR and Schefferville radars. Their work led to the concept of SuperDARN, where the radars in the network operate in pairs with common viewing area. The Doppler information from backscatter received by all radars can be combined to produce a two-dimensional plasma velocity field within the maps of plasma convection [*Greenwald et al.*, 1995]. Thus, every other subsequent SuperDARN radar followed the original design and modes of operation of GBR and Schefferville, with a few relatively minor modifications introduced more recently which still did not change the basic concept.

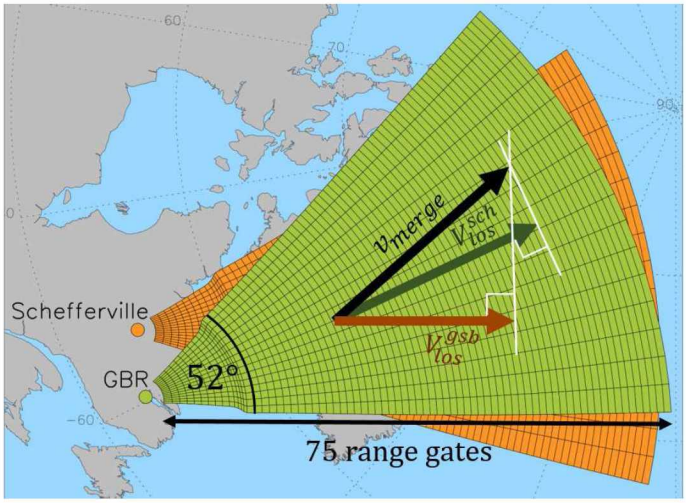

Figure 3.1. Fields-of-view and principle of the velocity Merge technique of the first two SuperDARN radars in Goose Bay and Schefferville.

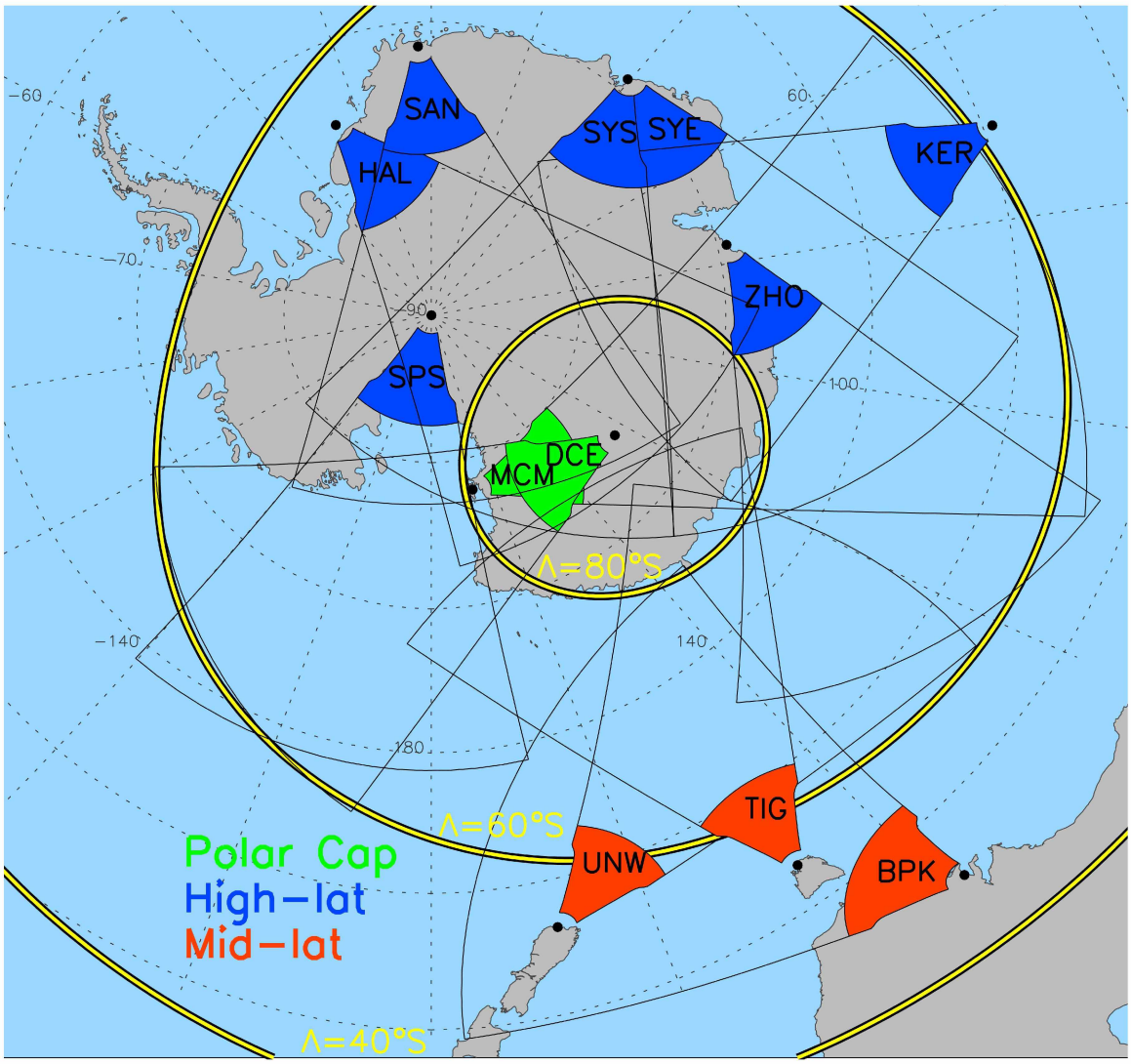

Figure 3.2. Fields-of-view of the SuperDARN radars in the southern hemisphere. The standard 3-letter code is given for each radar within its short-range FoV that refers to the *E*-region backscatter.

Today, SuperDARN is operated by an international consortium comprising researchers from 10 nations: Australia, Canada, China, France, Italy, Japan, Norway, South Africa, the United Kingdom and the United States. The network has 22 operational radars in the northern hemisphere and 12 radars in the southern hemisphere. Figure 3.2 shows the coverage of the southern hemisphere, where the *F*-region FoVs of the radars are shown with thin black lines and the *E*-region FoVs are filled with colors that correspond to the geomagnetic location of the radars. Yellow lines show 3 nominal boundaries between the

polar cap, the high-latitude, the mid-latitude, and the equatorial regions, that correspond to MLATs of 80°S, 60°S, and 40°S respectively. The two radars that are located in the magnetic polar cap, McMurdo (MCM) and Dome Concordia East (DCE), are shown in green. Seven radars located in the high-latitude region, South Pole Station (SPS), Halley (HAL), Sanae (SAN) , Syowa South (SYS), Syowa East (SYE), Kerguelen (KER), and Zhongshan (ZHO), are shown in blue. Three mid-latitude radars, TIGER Unwin (UNW), TIGER Tasmania (TIG), and TIGER Buckland Park (BPK), are shown in red.

SuperDARN has been operational for over 20 years and has proved to be highly successful for studying a wide range of ionospheric and magnetospheric phenomena. It has been used for studying dynamics and structure of global convection, magnetohydrodynamic waves, substorms, gravity waves, high-latitude plasma structures [*Chisham et al.*, 2007]. In this body of research, the SuperDARN radars are used to study irregularities in the E-region of the ionosphere.

3.1.2 Measured Spectral Parameters

The backscattered signals received by the radars are sampled and processed to produce multi-lag complex autocorrelation functions (ACF) as a function of range. The ACFs are fitted to standard functions in order to estimate the following backscatter parameters: the spectral power, the LOS Doppler velocity, and the width of the power spectrum, or, simply, the spectral width. These parameters are calculated for each range gate from where the radar received backscatter [*Hanuise et al.*, 1993].

SuperDARN radars employ multiple-pulse sequence to simultaneously determine the range and Doppler velocity of targets, the ionospheric irregularities [*Greenwald et al.*, 1985; *Hanuise et al.*, 1993; *Ponomarenko and Waters*, 2006]. The main reason for using the multiple pulses instead of using a single pulse is in the nature of the ionospheric irregularities that can move with velocities up to 4 km/s and are spread over ranges for as much as 4500 km. Long interpulse period with pulse repetition frequency (PRF) less than 33.3 Hz is used to avoid ambiguities in range, and short interpulse period with PRF greater than 320 Hz is used to avoid ambiguities in the Doppler velocity [*Ribeiro et al.*, 2013]. The radars periodically emit pulses that are separated unevenly in time by integer multipliers of an elementary lag time $\tau_0 = 1.5$–2.4 ms.

A transmitted signal has a form $T(t) = A\sin(\omega t + \Phi_0)$, where A is the envelope of the transmitted waveform, ω is the carrier frequency, Φ_0 is a constant phase angle, and t

represents time. A received signal $R(t) = B\sin((\omega + \omega_d)t + \Phi_1)$ has an envelope of the received signal B, a Doppler shift ω_d caused by a moving target, and a random phase Φ_1. The received signal is digitized and down converted to obtain the baseband signal by multiplying this received sinal by the sine (in-phase) and cosine (quadrature) of the carrier frequency, and passing it through a low-pass-filter. The result has a form $R(t) = R_i(t) + iR_q(t) = 1/2B\cos(\omega_d t + \Phi_1) + i1/2B\sin(\omega_d t + \Phi_1) = 1/2Be^{i(\omega_d t + \Phi_1)}$. The ACF is then formed by convolution of this received complex signal at time t with the same signal at time $t + \tau$, and can be expressed as $\mathrm{ACF}(\tau) =< R(t)R^*(t + \tau) >$, where $<>$ denotes convolution and $*$ corresponds to the complex conjugate [*Ribeiro et al.*, 2013].

Figure 3.3 shows an example of real and imaginary parts of ACF, its phase and power, as a function of the lag number j. The phase coherent receiver directly samples the voltage of the returned signals that is in phase (V_R), and the voltage out of phase (V_I) with the receiver, from a fixed range and for each pulse of the sequence. These two voltages together form a two-component complex signal. For each range gate and for each multipulse sequence one can represent the ACF for the j-th lag in terms of amplitude P_j (Figure 3.3a) and phase ϕ_j (Figure 3.3b), for a simple case when the ACF can be characterized by one particular Doppler shift frequency ω;

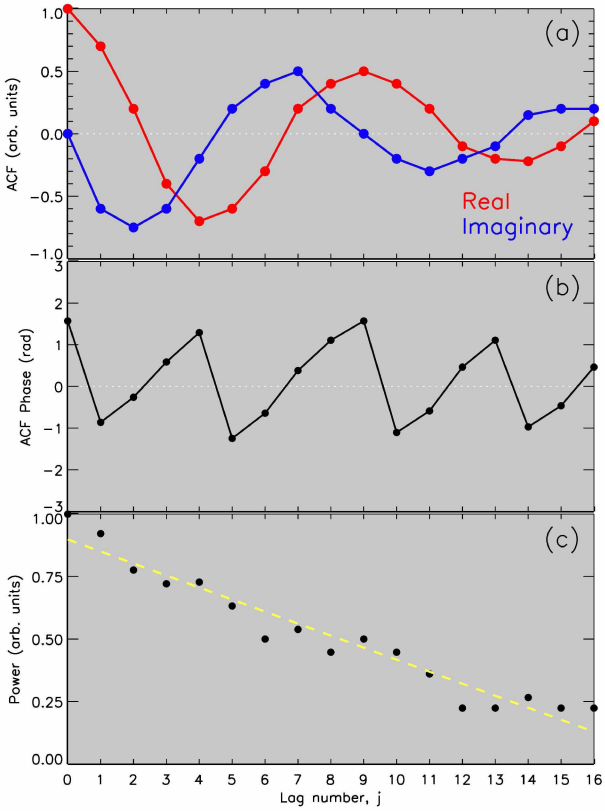

Figure 3.3. Example of ACF variation with lag number

$$R_j = P_j e^{i\phi_j} \tag{3.1}$$

ACFs calculated from all the sequences $R(\tau)$ are then integrated in order to minimize interference and increase gain. The model functions are fit to integrated ACFs in order to resolve Doppler velocity (V), spectral width (W), and backscatter power (signal-to-noise

ratio, SNR). The phase varies linearly with lag only between $-\pi$ and $+\pi$, with ambiguities occurring at every multiple of 2π, creating a sawtooth feature in Figure 3.3b. The power amplitude $P(\tau) = (\Re\{R(\tau)\}^2 + \Im\{R(\tau)\}^2)^{-1/2}$ is shown in Figure 3.3c, where the yellow dashed line shows the linear square fit.

The Doppler shift can be extracted from the systematic variation of phase with lag, where the phase ϕ at lag τ is an arctangent of the ratio of $\Re\{R(\tau)\}$ to $\Im\{R(\tau)\}$. Namely, the Doppler velocity V can be calculated as

$$V = \frac{\lambda}{4\pi}\frac{\partial\phi}{\partial\tau}, \tag{3.2}$$

where λ is radar wavelength, and

$$\phi = \arctan\frac{\Re\{R(\tau)\}}{\Im\{R(\tau)\}}. \tag{3.3}$$

The $\partial\phi/\partial\tau$ term can be found by using a fitting procedure FITACF that is similar to the least square fit. SNR is calculated using fitted lag zero power ($y-$intercept of fitted line in Figure 3.3c) as

$$\text{SNR} = 10\log_{10}(R_0/N). \tag{3.4}$$

The spectral width is a width of a model spectrum at a half-power level that can be calculated as

$$W = \frac{\lambda}{2\pi t_d}, \tag{3.5}$$

where t_d is the decay time of the signal that can be estimated by the slope for the linear log-power fit.

3.1.3 Derived Parameters

Figure 3.4 shows range-time-intensity (RTI) plots for the three parameters defined above. Each panel shows how a parameter changes with time and range for a particular beam; this presentation is a standard way to look at the SuperDARN data. Time resolution of a RTI plot is usually 1 min, since it is the time of one full scan of the entire FoV. The range resolution is 45 km in common mode. In special modes the gate length can be 15 or 30 km. Each plot cell corresponds to a particular time and a range gate and is color-coded according to the magnitude of the received parameters: (a) Doppler velocity, (b) power

and (c) spectral width, with color bars shown on the right. Grey color refers to the lack of backscatter or to the data eliminated after the post-processing algorithm described in the next section. Figure 3.4 shows the backscatter received on beam 7 of the MCM radar during the 24-hour period on April 7, 2013.

In Figure 3.4, a range gate of 765 km is marked with a white dotted line. This boundary is typically used to separate the backscatter received from the E- and F-regions. However, it is incorrect to think that if the backscatter is detected below that line then it is definitely originated from the E-region. For example, from 5 to 9 UT the backscatter was received at close range gates, but it still considered to be the F-region backscatter, because it is a part of the F-region band. In this context, "the F-region band" means the backscatter that occupies a certain ranges between 540–1440 km, with some variation in range boundaries that change during the day. The E-region backscatter also appears as an isolated band at the close ranges (180–720 km) with a gap separating it from the F-region. During the entire day, the F-region band was present, however, near magnetic midnight starting from 17 UT (MLT $\approx$ UT+7 at MCM) the F-region band disappeared and the E-region band appeared. These features show that a range of 765 km can be considered as the furthest range at which E-region backscatter can be observed and that undesirable contamination by F-region echoes near this range can be reduced by carefully examining RTI plots and limiting the periods of observations to only those where the backscatter is predominantly of the E-region origin, e.g. at 17–21 UT on April 7, 2013, shown in Figure 3.4. This method is implemented later in Chapters 4 and 5. The velocities inside of the band change polarity during the day since the radar's FoV rotates with the Earth probing the global ionospheric convection from different directions. Rapid velocity variation in the F-region band indicates that the global convection is very dynamic.

3.1.4 Data Post-Processing

SuperDARN radars measure the Doppler frequency shift of HF signals scattered by decameter-scale irregularities in the electron density. However, in many cases the ionospheric returns are contaminated by scatter from the ground or sea surface. The standard SuperDARN criteria of low velocity and low spectral width to exclude the ground and sea scatter from the radar datasets are:

$$|(|V| - \triangle V)| < 30 \text{ m/s}, \tag{3.6}$$

$$|(W - \triangle W)| < 35 \text{ m/s}, \tag{3.7}$$

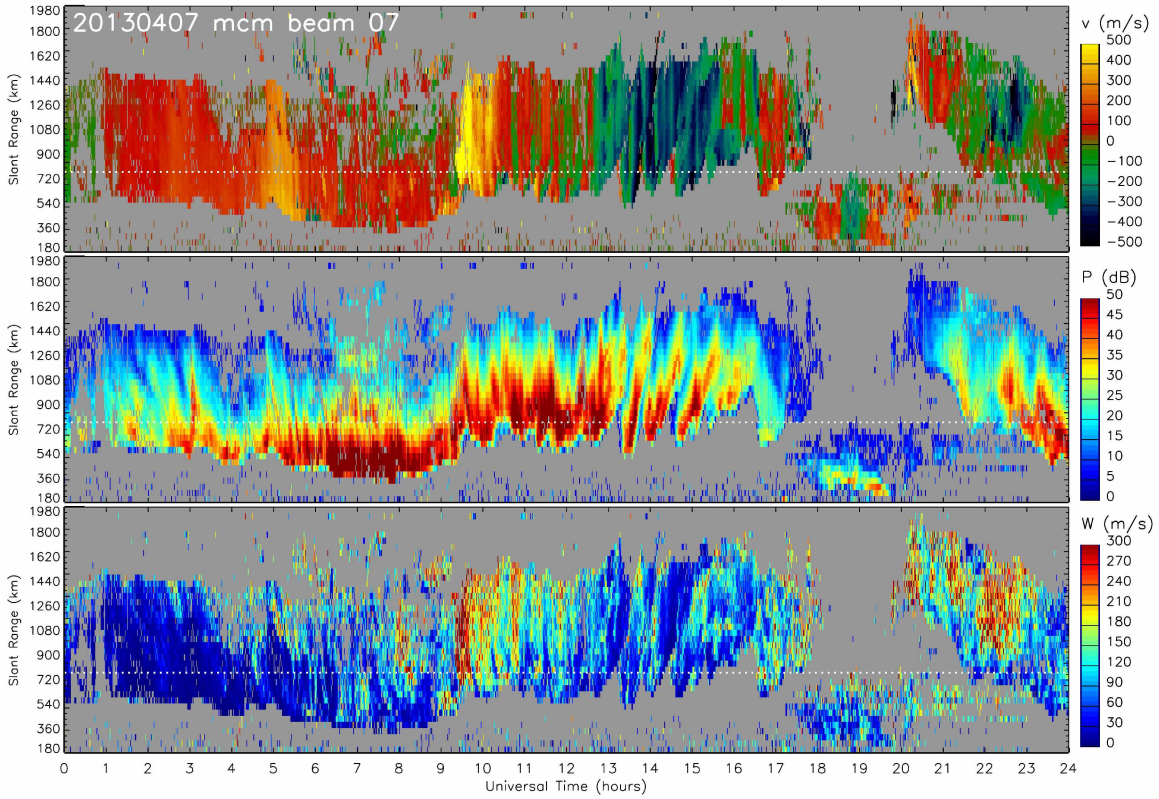

Figure 3.4. Range-time-intensity plots of the basic SuperDARN backscatter parameters: (a) Doppler line-of-sight velocity, (b) power, and (c) spectral width observed in beam 7 of McMurdo radar on April 07, 2013.

where $\triangle V$ and $\triangle W$ are the uncertainties in the fitted Doppler velocity and spectral width, respectively. The same criteria have been used in this body of work. In this research the large spectral width ($W > 500$ m/s) and low power (SNR < 3 dB) echoes were also eliminated from the dataset. These criteria have been adopted in a number of previous studies of E-region irregularities [*Carter and Makarevich*, 2010; *Carter et al.*, 2012; *Makarevitch et al.*, 2002; *Makarevich et al.*, 2012, 2015], since they have been demonstrated to result in a dataset that consisted of echoes that were predominantly of E-region origin.

3.1.5 Ionospheric Convection

The primary objective of the SuperDARN network is to study the global configuration and dynamics of plasma convection in the high-latitude ionosphere. The plasma convection represents an important diagnostic of energy transfer from the solar wind into the magnetosphere and ionosphere. Ionospheric irregularities in the F-region are moving with ambient

plasma at the $\mathbf{E} \times \mathbf{B}$ convection velocity. All SuperDARN radars measure Doppler LOS velocity of those irregularities, creating sets of 2D LOS vector fields.

In all SuperDARN-based techniques of plasma convection measurements, individual LOS velocity measurements are combined to produce a global-scale view of the ionospheric plasma motions, for example, using the Merge technique described in Section 3.1.1. However, this technique can be applied only to paired radars, but not to a single radar. *Ruohoniemi and Baker* [1998] have developed a new technique called "Map Potential" which finds the function for the electrostatic potential Φ that fits best to all LOS velocity measurements. The LOS velocities are combined in the global equal-area grid cells and then the gridded velocity data are fitted using the following model of electrostatic potential Φ

$$\Phi(\theta, \phi) = \sum_{l=0}^{L} \sum_{m=0}^{\min(l,M)} (A_{lm} \cos m\phi + B_{lm} \sin m\phi) P_l^m(\cos\theta), \tag{3.8}$$

where the P_l^m are the associated Legendre functions. The spherical coordinates θ and ϕ correspond to the polar (or colatitudinal) and azimuthal (or longitudinal) coordinates, respectively. Integers L and M determine the resolution in the fitting and the coefficients of the expansion A_{lm} and B_{lm} express the physical content of the solution. As Map Potential technique is applied to the available SuperDARN data within the specific time interval, the locations with no data are supplemented by modeled velocities based on the IMF conditions [*Ruohoniemi and Greenwald*, 1995, 2005]. A set of coefficients is obtained from the fit that describe the instantaneous convection pattern.

Once the electrostatic potential function is known, it is possible to determine the global plasma convection velocity through the relationships

$$\mathbf{E} = -\nabla\Phi, \tag{3.9}$$

$$\mathbf{v} = \frac{\mathbf{E} \times \mathbf{B}}{B^2}. \tag{3.10}$$

Namely, the 2D velocity vector $\mathbf{v}$ is the "fitted velocity" at a particular location (θ, ϕ), which, together with all other locations, gives the global plasma convection pattern.

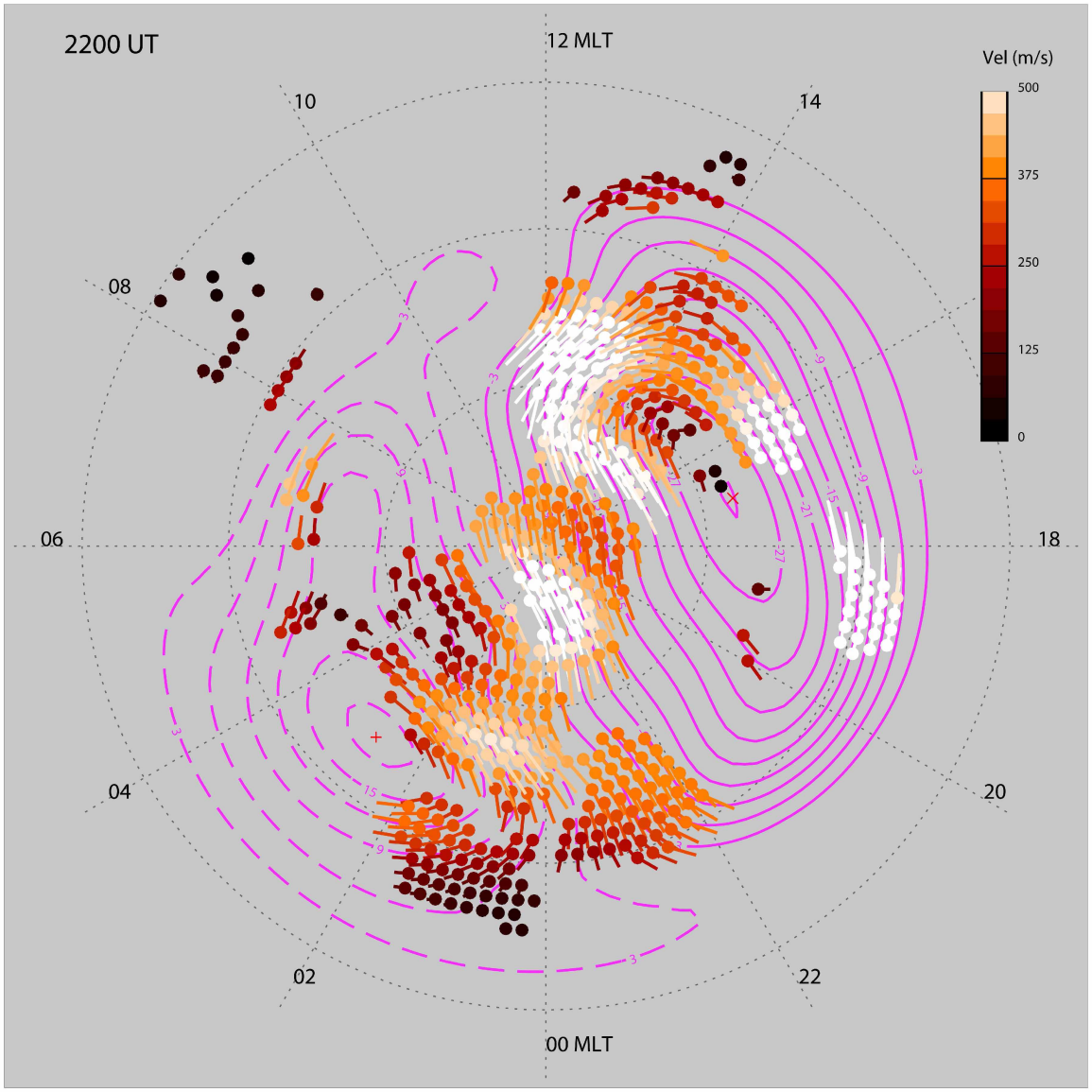

Figure 3.5. 10-min average of global convection in the southern hemisphere on February 13, 2013, 22:00–22:10 UT.

Figure 3.5 shows the 10-min averaged convection map obtained using the Map Potential algorithm on February 13, 2013 at 22:00−22:10 UT. The orientation of the map is such that the magnetic midnight (midday) is at the bottom (top) and the magnetic coordinate grid is shown by grey lines with MLATs shown every 10°. The magnitude of the fitted velocity vectors is shown by color-coded circles with the color bar shown on the right. The direction of the fitted vectors is shown by straight lines whose length also indicates the magnitude of the plasma velocity. The equipotential lines (dashed for positive and solid for negative)

are shown in pink. Electrostatic potential contours also represent flow streamlines in the ionosphere. In this example, the convection pattern consists of two convection cells with antisunward flow across the polar cap that returns to the dayside via sunward flow on the dawn and dusk flanks. This convection pattern is very similar to the schematic two-cell pattern shown in Figure 1.5.

3.1.6 Raytracing

In this research we used a version of standard raytracing tools based on numerical solutions of the Hamiltonian ray path equations [*Haselgrove*, 1963; *Jones and Stephenson*, 1975] that allows to consider arbitrary density distributions in order to model the propagation of the radar signal. This tool is used in Chapter 4 to estimate the aspect angle of the backscatter for different elevation angles at a fixed height, and to pinpoint the vertical positions where the orthogonality with the magnetic field is met. Without the presence of the magnetic field in the collisionless plasma, the refraction of the electromagnetic wave that travels through it can be described by the Snell's law at each layer of the plasma with a different electron concentration. In the presence of the magnetic field, the expression for the refractive index was first derived by Lorentz to explain the passage of light through crystals, and further modified by Appleton and Hartree to describe the refraction of the radio signal propagating through the isotropic ionosphere [*Budden*, 1985]. A set of differential equations that describes the ray path in the collisional anisotropic plasma with continuously varying refractive index in three dimensions [*Haselgrove*, 1955] were used to develop a computational program that integrates the ray path through the ionosphere for a given location and frequency of the transmitter, elevation angle, and electron density distribution [*Jones and Stephenson*, 1975].

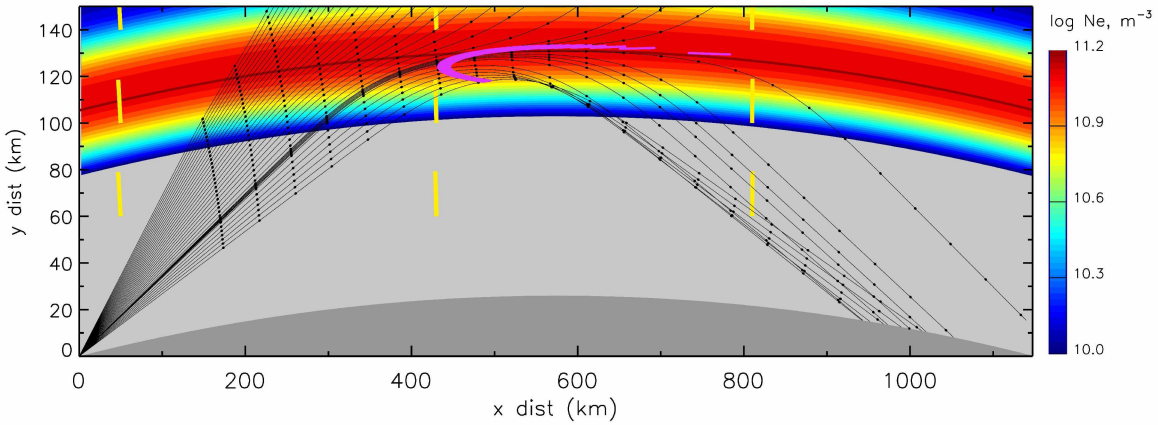

Figure 3.6. Raytracing simulation of 10-MHz radio signal propagation path through the ionosphere that has a Gaussian density profile shown with color contours. The magnetic field direction is shown in yellow, and the orthogonality area is shown in pink. The black lines show the rays from HF radio transmitter that is located in the bottom-left corner.

Figure 3.6 shows how a 10-MHz radio signal from beam 7 of MCM would propagate in the modeled altitude-stratified Gaussian E-layer. The Gaussian layer has a peak altitude of 110 km, peak E-region density of 1.2×10^5 cm^3, and layer thickness factor of 20 km. The color contours show the electron density with color bar shown on the right. Yellow vertical lines represent the magnetic field in that region based on the AACGM coordinate system with 2010 coefficients. Since MCM is located in the polar cap, the magnetic field there is almost vertical. Thirty five rays with initial elevation angles from 10° to 30° are shown with solid black lines. Six additional rays are plotted near the elevation angle of 19° to increase the resolution in this region. The small circles along the rays represent the radar range gates starting from 180 km separated by 45 km. In order to detect the backscatter from the field-aligned irregularities, the radar beam should enter the aspect angle cone almost perpendicularly to the magnetic field. Evaluating the angle between the magnetic field and the ray path, the areas of orthogonality can be found. Pink line shows the region where the aspect angle is less than 0.5°, and, thus, this is the orthogonality region from where the backscatter will most likely be received.

3.1.7 Virtual Height Model

One way to obtain the altitude information in the absence of reliable interferometer measurements is to use the virtual height model that describes the most probable altitude from where the HF radar signal is scattered. *Chisham et al.* [2008] developed an empirical virtual height model of the backscatter targets by studying the elevation angles of the arrived signals from a 5-year dataset of the SuperDARN Saskatoon radar.

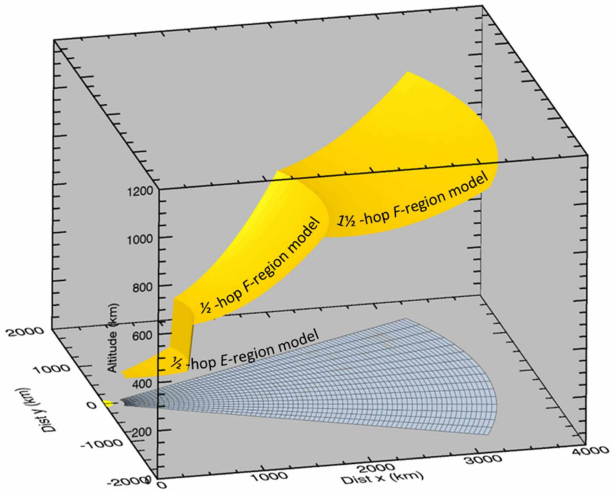

Figure 3.7. 3D view of the virtual height model for a SuperDARN radar.

Figure 3.7 shows a 3D view of a SuperDARN FoV based on the virtual height model. The projection of a FoV is shown in blue and the virtual height surface is shown in yellow. There are three distinct virtual height regions that were modeled as a quadratic polynomial fitted to the virtual height distribution:

$$h(r) = A + Br + Cr^2, \tag{3.11}$$

where r is slant range distance, and the coefficients A, B and C are shown in the Table 3.1 below.

Table 3.1. Coefficients for 3 quadratic polynomials that describe 3 regions of the virtual height model.

Backscatter Type	A	B	C
$\frac{1}{2}$-hop E-region	108.974	0.0191271	6.68283×10^{-5}
$\frac{1}{2}$-hop F-region	384.416	-0.178640	1.81405×10^{-4}
$1\frac{1}{2}$-hop F-region	1098.28	-0.354557	9.39961×10^{-5}

$\frac{1}{2}$-hop E-region is below 790 km range, $\frac{1}{2}$-hop E-region is between 790 km and 2130 km range, and $1\frac{1}{2}$-hop F-region is above 2130 km. The height of the surface is determined by Equation (3.11) with slant range distance along the direction of 16 beams. The transition between $\frac{1}{2}$-hop E-region and $\frac{1}{2}$-hop F-region propagation modes is not well described by

the model, this is why the sharp jump or discontinuity is visible in this transitional region. This model was used in this research to provide additional support for the choice of the boundary between E- and F-region echoes.

3.2 Defense Meteorological Satellite Program

Another observational technique that can provide information about the convection plasma flow in the F-region is the Defense Meteorological Satellite Program (DMSP). In this research, DMSP satellite data were used to determine if the convection velocity component was high enough for FBI to be operational (see Section 4.3). DMSP satellites circle the Earth at an altitude of ~ 850 km in a near-polar, Sun-synchronous low-Earth orbit. Satellites are three-axis stabilized and provide precision pointing to support a number of mission sensors [*Rich and Hairston*, 1994]. The sensor that is used in this research is Ion Drift Meter (IDM). IDM is a Faraday cup looking into the direction of the spacecraft's travel [*Pokhotelov et al.*, 2008]. As the ions enter the cup, if there is any cross-track velocity, there will be an imbalance on the number of ions (current measured) hitting one plate of the cup versus the other. By measuring the differences in the current and knowing the geometry of the IDM, the cross track velocities are calculated. The spacecraft velocity (generally about 7.5 km/s) is always larger than the cross track ion velocities and the limit on the measurable cross track velocities is ± 3.0 km/s [*Pokhotelov et al.*, 2008]. Currently there are 6 DMSP satellites in orbit named F15, F16, F17, F18, F20. The path of DMSP F17 relative to the southern polar cap on February 02, 2013 is shown in Figure 3.8. The yellow lines show the locations with MLAT of 80°S, 60°S and 40°S; same as in Figure 3.2. The cross-track ion drift is shown in red with positive (negative) direction to the right (left) of the path.

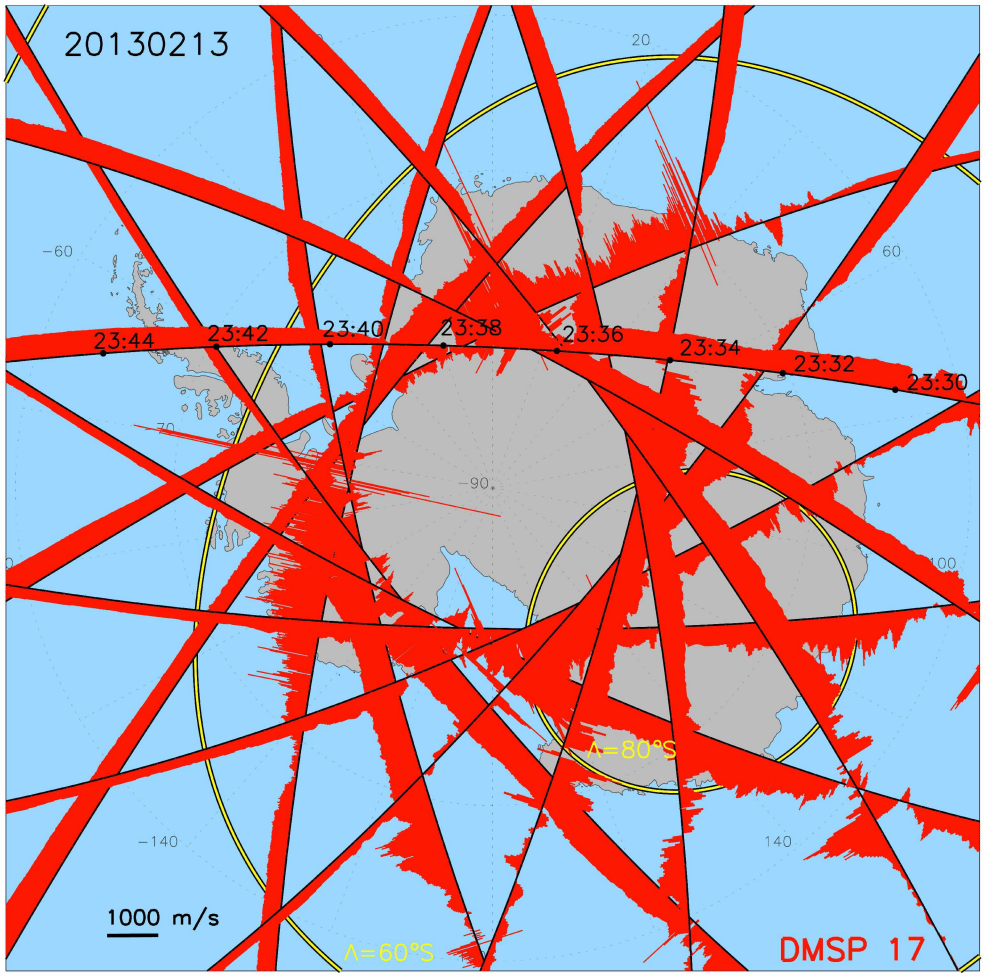

Figure 3.8. DMSP F17 satellite 24-h path with the horizontal ion drift velocity.

Figure 3.8 shows that IDM data are regularly available in the southern polar cap, the inner yellow circle. This provides a complementary dataset to SuperDARN measurements, which is particularly useful in cases of low-to-no backscatter occurrence at the locations of interest.

3.3 International Reference Ionosphere Model

The International Reference Ionosphere (IRI) is a standard model for estimation of the electron density in the ionosphere commonly used for raytracing simulation and calculation of the aspect angles [e.g. *Uspensky et al.*, 1994; *Koustov et al.*, 2001]. In this research, IRI is used to obtain the electron density profile at a particular radar location in order to model the ray path propagation and find the areas where the radar signal reaches the orthogonality with the magnetic field (see Section 4.6).

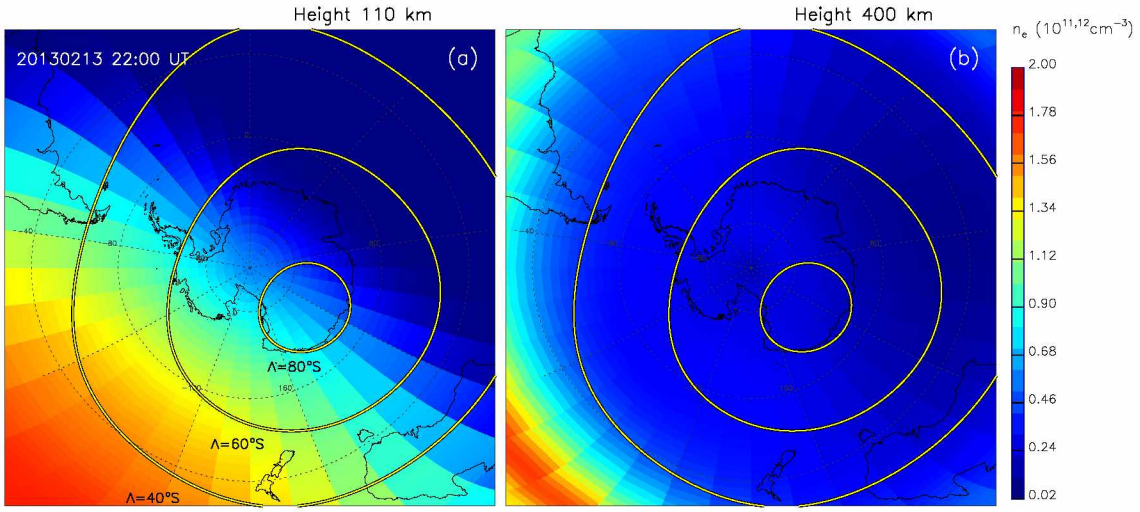

Figure 3.9. Electron density obtained from the IRI 2012 model for February 13, 2013 for heights of (a) 110 and (b) 400 km.

IRI is an empirical data-based model of ionospheric parameters in the altitude range 50–2000 km. The modeled parameters include the electron density, electron temperature, ion composition (percentage of O^+, H^+, He^+, N^+, NO^+, O_2^+ , and Cluster ions), ion temperature, ionospheric electron content up to a specified upper height limit, ion drift at magnetic equator, spread-F occurrence probability, and auroral boundaries. These parameters are given as functions of height, latitude, longitude, time of day (LT or UT) , and date. Required model drivers are solar indices (13-month running mean of sunspot number; daily, yearly, and 81-day averages of the solar radio flux at 10.7 cm wavelength), ionospheric index (13-months running mean of Global Ionosphere index IG), magnetic indices (daily and 3-h Ap) and COSPAR International Reference Atmosphere (CIRA) neutral densities and temperature [*Bilitza et al.*, 2014]. The IRI model was created using the data from the worldwide network of ionosondes, incoherent scatter radars (Jicamarca, Arecibo, Millstone

Hill, Malvern, St. Santin), the ISIS and Alouette topside sounders, and in situ instruments on several satellites and rockets.

Figure 3.9 shows the electron density for the southern hemisphere obtained from the IRI model for (a) E- and (b) F-region heights for February 13, 2013, 22 UT. The IRI model was run for heights of 110 km and 400 km for geographic grid with 2° latitudinal and 10° longitudinal resolution. The electron density was determined for each grid cell and color-coded, with color bar shown on the right. This plot demonstrates how the E-region electron density distribution differs from the F-region distribution. Relative to the Figure 3.9, the electron density in the E-region has a diagonal symmetry (follows the terminator) whereas the F-region density has more radial symmetry with higher density being closer to the equator.

3.4 Mass Spectrometer and Incoherent Scatter Model

The Mass Spectrometer and Incoherent Scatter (MSIS) is an empirical model of the Earth's neutral atmosphere that describes the neutral temperature and densities from ground to thermospheric heights. For this research we use the density of the neutral species O, O_2, and N_2 and the temperature of the neutrals from MSIS in order to estimate the collisional frequency of electrons and ions with neutrals using a set of standard empirical equations [*Schunk and Nagy*, 1978, 1980].

A primary use of MSIS is to predict the satellite orbital decay due to atmospheric drag. This model taking into account data derived from space shuttle flights and incoherent scatter radar results. The inputs are similar to the IRI model inputs and the outputs are the density of neutral species (He, O, O_2, N, N_2, Ag, H) and the neutral temperature. Figure 3.10 shows the results of MSIS-E-90 model for the southern hemisphere for a similar grid and time as in Figure 3.9. Panels (a, b) displays the total number density of the neutrals and panels (c, d) displays the neutral temperature. First (second) column corresponds to the E-region (F-region) height of 110 km (400 km). Again, as in the case of the electron density from IRI, the results for different heights vary significantly. SuperDARN radars sample both E-region heights in the close-range gates and F-region heights in the far-range gates. As demonstrated in Figures 3.9 and 3.10, the parameters that describe the ionosphere can be significantly different for these two heights, which results in the different irregularity formation mechanisms in the E- and F-regions.

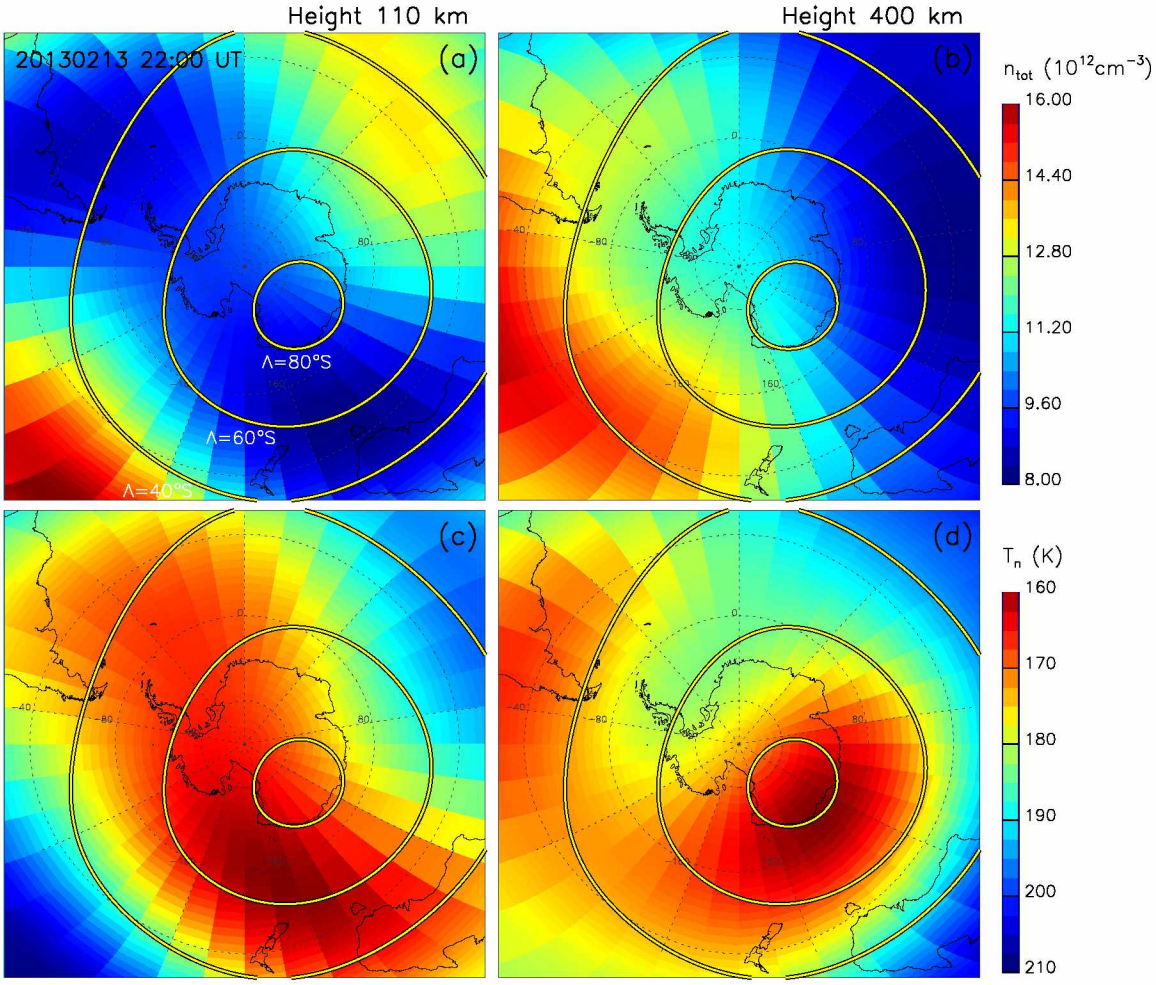

Figure 3.10. Total number density of neutral molecules O, O_2, N_2 (a,b) and temperature of neutrals (c,d) obtained by MSIS-E-90 model for February 13, 2013 for heights of 110 (a,c) and 400 km (b,d).

3.5 References

Bilitza, D., D. Altadill, Y. Zhang, C. Mertens, V. Truhlik, P. Richards, L.-M. McKinnell, and B. Reinisch (2014), The International Reference Ionosphere 2012 - a model of international collaboration, *J. Space Weather Space Clim.*, *4*, doi:10.1051/swsc/2014004.

Budden, K. G. (1985), *The propagation of radio waves: the theory of radio waves of low power in the ionosphere and magnetosphere*, Cambridge University Press.

Carter, B. A., and R. A. Makarevich (2010), On the diurnal variation of the E-region coherent HF echo occurrence, *J. Atmos. Sol. Terr. Phys.*, *72*, 570–582, doi:10.1016/j.jastp.2010.02.004.

Carter, B. A., R. A. Makarevich, J. C. Devlin, and A. J. McDonald (2012), Coincident multi-point observations of the E- and F-region decametre-scale plasma waves at high latitudes, *J. Atmos. Sol. Terr. Phys.*, *80*, 323–335.

Chisham, G., T. K. Yeoman, and G. J. Sofko (2008), Mapping ionospheric backscatter measured by the SuperDARN HF radars - Part 1: A new empirical virtual height model, *Ann. Geophysicae*, *26*, 823–841.

Chisham, G., et al. (2007), A decade of the Super Dual Auroral Radar Network (SuperDARN): scientific achievements, new techniques and future directions, *Surveys in Geophysics*, *28*, 33–109, doi:10.1007/s10712-007-9017-8.

Greenwald, R. A., K. B. Baker, R. A. Hutchins, and C. Hanuise (1985), An HF phased-array radar for studying small-scale structure in the high-latitude ionosphere, *Radio Sci.*, *20*, 63–79.

Greenwald, R. A., et al. (1995), DARN/SuperDARN: A global view of the dynamics of high-latitude convection, *Space Sci. Rev.*, *71*, 763–796.

Hanuise, C., C. Senior, J.-C. Cerisier, J.-P. Villain, R. A. Greenwald, J. M. Ruohoniemi, and K. B. Baker (1993), Instantaneous mapping of high-latitude convection with coherent HF radars, *J. Geophys. Res.*, pp. 17,387–17,400.

Haselgrove, J. (1955), Ray theory and a new method for ray tracing, in physics of the ionosphere, *Conference on the Physics of the Ionosphere, Proc. Phys. Soc. London*, *23*, 355–364.

Haselgrove, J. (1963), The hamiltonian ray path equations, *J. Atmos. Terr. Phys.*, *25*, 397–399.

Jones, R. M., and J. J. Stephenson (1975), A versatile three dimensional ray tracing computer program for radio waves in the ionosphere, *OT Report 75-76, US Dep. of Comm., Washington, DC, USA*.

Koustov, A. V., K. Igarashi, D. André, K. Ohtaka, N. Sato, H. Yamagishi, and A. Yukimatu (2001), Observations of 50- and 12-MHz auroral coherent echoes at the Antarctic Syowa station, *J. Geophys. Res.*, *106*, 12,875–12,887.

Makarevich, R. A., A. V. Koustov, and B. A. Carter (2012), Interplanetary magnetic field control and magnetic conjugacy of auroral E region backscatter, *Geophys. Res. Lett.*, *117*, A01309, doi:10.1029/2011JA016943.

Makarevich, R. A., V. V. Forsythe, and A. C. Kellerman (2015), Electric field control of E region coherent echoes: Evidence from radar observations at the South Pole, *J. Geophys. Res. Space Physics*, *120*, 2148–2165, doi:10.1002/2014JA020844.

Makarevitch, R. A., A. V. Koustov, G. J. Sofko, D. André, and T. Ogawa (2002), Multifrequency measurements of HF Doppler velocity in the auroral E region, *J. Geophys. Res.*, *107*, 1212, doi:10.1029/2001JA000268.

Pokhotelov, D., C. N. Mitchell, P. S. J. Spencer, M. R. Hairston, and R. A. Heelis (2008), Ionospheric storm time dynamics as seen by GPS tomography and in situ spacecraft observations, *J. Geophys. Res.*, *113*, doi:10.1029/2008JA013109.

Ponomarenko, P. V., and C. L. Waters (2006), Spectral width of SuperDARN echoes: Measurement, use and physical interpretation, *Ann. Geophysicae*, *24*, 115–128.

Ribeiro, A. J., J. M. Ruohoniemi, P. V. Ponomarenko, L. B. N. Clausen, J. B. H. Baker, R. A. Greenwald, and K. Oksavik (2013), A comparison of SuperDARN ACF fitting methods, *Radio Sci.*, *48*, 274–282.

Rich, F. J., and M. Hairston (1994), Large-scale convection patterns observed by DMSP, *J. Geophys. Res.*, *99*, 3827–3844.

Ruohoniemi, J. M., and K. B. Baker (1998), Large-scale imaging of high-latitude convection with Super Dual Auroral Radar Network HF radar observations, *J. Geophys. Res.*, *103*, 20,797–20,811.

Ruohoniemi, J. M., and R. A. Greenwald (1995), Observations of IMF and seasonal effects in high-latitude convection, *Geophys. Res. Lett.*, *9*, 1121–1124.

Ruohoniemi, J. M., and R. A. Greenwald (2005), Dependencies of high-latitude plasma convection: Consideration of interplanetary magnetic field, seasonal, and universal time factors in statistical patterns, *J. Geophys. Res.*, *110*, A09204, doi:10.1029/2004JA010815.

Schunk, R. W., and A. F. Nagy (1978), Electron temperatures in the F region of the ionosphere: Theory and observations, *Rev. Geophys. Space Phys.*, *16*, 355–399.

Schunk, R. W., and A. F. Nagy (1980), Ionospheres of the terrestrial planets, *Rev. Geophys. Space Phys.*, *18*, 813–852.

Uspensky, M. V., A. V. Kustov, G. J. Sofko, J. A. Koehler, J.-P. Villain, C. Hanuise, J. M. Ruohoniemi, and P. J. S. Williams (1994), Ionospheric refraction effects in slant range profiles of auroral HF coherent echoes, *Radio Sci.*, *29*, 503–517.

Chapter 4

Dual Radar Investigation of *E*-Region Plasma Waves in the Southern Polar Cap [I]

4.1 Abstract

Origins and characteristics of small-scale plasma irregularities in the polar ionosphere are investigated using a dual radar setup in which the E region is probed from opposite directions by two Super Dual Auroral Radar Network (SuperDARN) facilities at the McMurdo and Dome Concordia Antarctic stations. In certain time intervals, velocity agreement is observed when velocities are compared at the same physical location in the horizontal plane. Such an agreement is widely expected if velocity at a given location is largely controlled by the convection electric field. In other cases, however, velocity agreement is unexpectedly observed when measurements are considered at the same slant range (distance along the radar beam) for both radars. This implies that it is not the electric field at a given location that is a controlling factor. Raytracing results show that the same range agreement may be explained for certain E-region density conditions when echo altitude increases with radar range. Backscatter observations under generally unfavorable conditions for irregularity generation and the critical role of propagation conditions in the polar cap are discussed. The observed E-region velocity in the polar cap is demonstrated to depend indirectly on the plasma density distribution, which is important for establishing the fundamental dependence on the convection electric field.

[I]Published as: Forsythe, V. V., and R. A. Makarevich (2015), Dual radar investigation of E region plasma waves in the southern polar cap, *J. Geophys. Res. Space Physics*, *120*, 9132-9147, doi:10.1002/2015JA021664.

4.2 Introduction

The high-latitude ionosphere is a highly structured medium with plasma waves or irregularities generated by various plasma instabilities. In the central E region (100–120 km), the two primary structuring mechanisms at small scales (< 100 m in wavelength) are the Farley-Buneman instability (FBI) and the gradient-drift instability (GDI) [*Fejer and Kelley*, 1980]. Much experimental effort has been dedicated to observations of coherent radar backscatter from auroral E-region irregularities, also known as the radar aurora. A particular focus has been on studies of fundamental dependencies of irregularity characteristics using progressively more advanced radar setups [see reviews by *Haldoupis*, 1989; *Sahr and Fejer*, 1996; *Makarevich*, 2009].

Dual radars operating as a stereoscopic system offer distinct advantages over single-radar setups, including measurements of both horizontal components of irregularity phase velocity $\mathbf{V}_{\rm irr}$ rather than the single line-of-sight (LOS) component $V_{\rm irr}^{\rm LOS}$. Several such systems operating at very high frequencies (VHF, 30–300 MHz) have been used, including the Scandinavian Twin Auroral Radar Experiment (STARE) [*Greenwald et al.*, 1978]. In combination with measurements of the plasma convection velocity $\mathbf{V}_E = \mathbf{E} \times \mathbf{B}/B^2$ by the European Incoherent Scatter (EISCAT) radar facility in the STARE's field-of-view (FoV), this enabled a discovery of the non-trivial dependence $\mathbf{V}_{\rm irr}(\mathbf{V}_E)$ or, equivalently, $V_{\rm irr}^{\rm LOS}(V_E, \theta)$, where θ is the flow angle, i.e. angle between the wave propagation vector and $\mathbf{V}_E$ [*Nielsen and Schlegel*, 1983; *Nielsen et al.*, 2002]. In contrast with a simple cosine dependence found in the F region, $V_{\rm irr}^{\rm LOS} = V_E \cos\theta$, the E-region velocity at small flow angles was found to be limited by the ion-acoustic speed $C_s < V_E$ [*Nielsen and Schlegel*, 1983].

The dual radar idea extended to high frequencies (HF, 3–30 MHz) gave rise to the Super Dual Radar Auroral Network (SuperDARN) [*Greenwald et al.*, 1995], an array of over 30 radars that observe both E- and F-region irregularities and monitor global plasma convection pattern in both hemispheres. Even though dual nature of SuperDARN mostly applies to the F region, new results on E-region irregularities were also obtained using HF-VHF radar combinations [*Koustov et al.*, 2001, 2002; *Makarevitch et al.*, 2001] and closely-spaced pairs of HF radars [*Milan and Lester*, 1999; *Makarevich*, 2008; *Carter and Makarevich*, 2009]. In contrast with earlier VHF studies, velocity behavior was found to differ for different HF echo populations ranging from cosine-like dependence $V_{\rm irr}^{\rm LOS} \propto \cos\theta$ to constancy with the flow angle $V_{\rm irr}^{\rm LOS} \approx const$ [*Makarevich*, 2008, 2010].

In comparison with auroral studies, radar echoes from the polar E region have received much less attention despite several important differences. These are expected because of the potentially weaker role of plasma density gradients [*Hanuise*, 1983; *Carter et al.*, 2012] and the potentially stronger role of ionospheric refraction [*Kustov et al.*, 1994, 1996]. Both of these arise because the magnetic field is almost vertical in the polar cap. In this geometry, a radio beam can propagate long distances without changing its altitude or orientation with respect to the magnetic field refracting by the same amount as the Earth's curvature. This is a case of the so called *Pedersen ray* or *Pedersen mode* propagation [*Davies*, 1990]. If enough refraction is not achieved, no backscatter is expected because of the high aspect sensitivity of E-region echoes, with both power and velocity quickly decreasing with an increasing aspect angle α (angle between the wave propagation direction and the perpendicular to the magnetic field). In other words, the radar ray needs to be orthogonal with the magnetic field (the orthogonality condition). For that to happen in the polar cap, refraction needs to be particularly strong, which means that the aspect conditions in the polar cap are highly unfavorable. Despite that, E-region radar returns from these high latitudes are not uncommon [*Kustov et al.*, 1996; *Carter et al.*, 2012]. This raised an important question of whether aspect angles can be actually reduced from their nominally-large values (i.e. assuming no refraction) and orthogonality achieved under some propagation conditions in the polar cap.

Stereoscopic radar observations of the polar E region are yet to be explored in addressing these issues, as well as in clarifying aspects of irregularity generation that are common to both auroral and polar regions. The common issues related to velocity can be illustrated in terms of expected dependencies of irregularity velocity $V_{\rm irr}^{\rm LOS}$ upon five independent variables. These are background convection speed V_E, flow angle θ, aspect angle α, height h, and radar frequency $f_{\rm rad}$ [e.g. *Schlegel*, 1996]. If two HF radars operate at the same frequency and probe the E region from two opposite directions, three of these variables $(V_E, \theta, f_{\rm rad})$ would be the same for both radars. This would then theoretically allow one to study the velocity dependence on the two remaining variables of α and h, without other competing effects. The recent deployment of two SuperDARN radars at the McMurdo and Dome Concordia Antarctic stations created a stereoscopic system covering a significant portion of the polar cap, with the added advantage of two oppositely directed beams.

The aim of the present study is to investigate formation of the E-region backscatter using this new dual HF radar setup. The specific objectives are to (1) explore velocity observations

with two radars probing the E region from opposite directions in the polar cap, (2) clarify roles of convection velocity versus height and aspect variations in controlling the phase velocity, and (3) analyze differences between auroral and polar irregularity characteristics and the possible implications for the role of refraction, aspect sensitivity, and generating mechanisms.

4.3 Experiment Configuration and Data Processing

In this study, we employed the data collected by two SuperDARN radars located at the McMurdo and Dome Concordia Antarctic stations. Using the standard SuperDARN three-letter radar codes, these radars are referred to as MCM and DCE (Dome C East). MCM and DCE are similar technically and operationally to other radars in the network [*Greenwald et al.*, 1995; *Chisham et al.*, 2007]. The estimates of the Doppler velocity, power, and spectral width of the ionospheric echoes are obtained from the 17-lag autocorrelation function measured by each radar. Both the MCM and DCE radars have 16 azimuthal beam directions separated by $\sim 3.3^\circ$ that form a $\sim 52^\circ$ field-of-view (FoV). For each beam, the radars sample 75 range gates, separated by 45-km gate length with the first range gate at 180 km. The radars complete one full scan in 1 min. For the data set considered in this study, MCM was using either two frequencies of 10 and 12 MHz simultaneously or a single frequency of 10 MHz, while DCE was alternating between these two frequencies every other scan. Only the data at 10 MHz were used in this study.

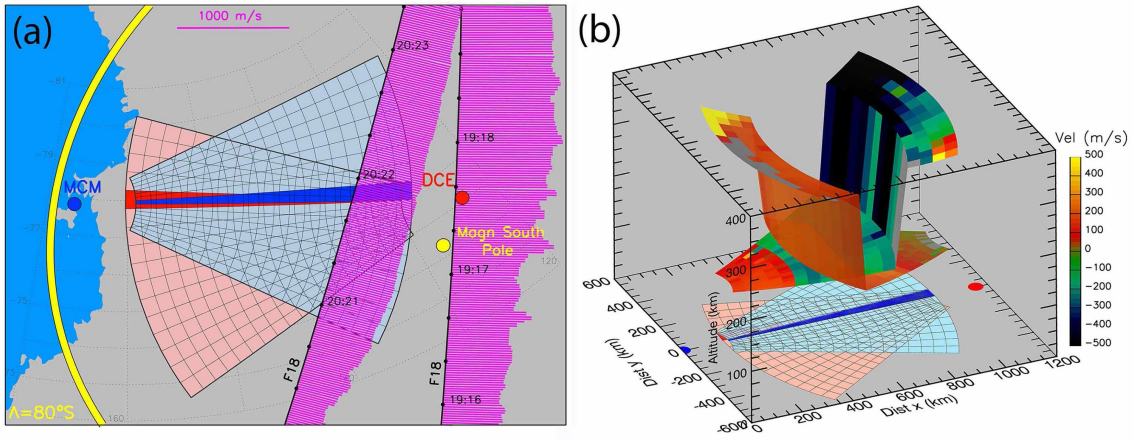

Figure 4.1. (a) The SuperDARN McMurdo (MCM) and Dome C East (DCE) radars locations and footprints (ranges 180–945 km). Beam 7 MCM (11 DCE) is marked with blue (red) color. Magnetic south pole and 80°S magnetic latitude are shown in yellow. Also shown are the cross-track ion drift velocities for two Defense Meteorological Satellite Program passes on February 16, 2014, 1900–2200 UT. (b) Field-of-view plot of the average velocity observed on February 16, 2014, 2000–2100 UT. The 3D location of each cell is plotted according to the SuperDARN virtual height model. Each radar cell is color-coded in average velocity according to the color bar shown on the right.

The dual radar experimental setup is illustrated in Figure 4.1. Panel (a) presents a geographic map view that shows locations and footprints of both radars. Shown are the

nominal edges for all beams and range gates up to 990 km that form a grid of beam-range cells (radar cells). The MCM radar site is located at 77.88°S, 166.73°E and DCE at 75.09°S, 123.35°E in geographic coordinates. Based on the altitude-adjusted corrected geomagnetic (AACGM) coordinate system with 2010 coefficients [*Shepherd*, 2014], the FoVs of both radars are located within the polar cap. This is illustrated by the yellow line and the circle in Figure 4.1a that show the locations with a magnetic latitude (MLAT) of 80°S and 90°S (i.e. south magnetic pole), respectively. The MCM beam 7 (highlighted with blue in Figure 4.1) and the DCE beam 11 (highlighted with red) are the most aligned beams, and the analysis in this paper focused on this pair of aligned beams.

Figure 4.1a also presents the cross-track ion drift velocities measured during two passes of the Defense Meteorological Satellite Program (DMSP) with the ion drift meter instrument [*Rich and Hairston*, 1994] near MCM and DCE for one event considered in this study (February 16, 2014, 1900–2200 UT). These measurements show relatively uniform convection flows, with cross-track components exceeding 500 m/s. This means that the convection velocity exceeded a threshold required for FBI to be operational during a significant portion of this event.

The expected altitude profile of measurements is represented by the surface plot of Figure 4.1b. The altitude of each beam-range cell is plotted according to the virtual height model [*Chisham et al.*, 2008] and color coded in average Doppler velocity for a representative interval on February 16, 2014 (2000–2100 UT). The $x - y$ plane also shows the radars' footprints. The virtual height model involves an empirical expression for the height as a function of the radar range from which the radar signal will most likely be scattered. The model does not describe a transition between different propagation modes, e.g. between E- and F-region backscatter. This is why a sharp jump or discontinuity is visible between the E and F regions in the virtual height behavior in Figure 4.1b. A range gate 14 or the range of 810 km is where the E/F region transition most often occurs, according to the model. Figure 4.1b shows that this is also approximately the case for MCM and DCE observations, based on the sharp increase in the observed velocities between range gates 13 and 15 (where the color changes from green to dark blue for the left radar). In practice, the transition in altitude between the E and F regions will not be as sharp and in the following analysis the range and the virtual height information is used to provide context for observations. The focus of this study is on dual radar observations of the E region, with the common ranges of 180–990 km, Figure 4.1. The data from those near-range gates were analysed in the current

study.

MCM has been in continuous operations since 2010, while DCE radar started its operations in January 2013. The first two full years of data when both radars were operating simultaneously were considered to identify and analyze four events of interest, which matched the following criteria. The main criterion for the event selection was the continuous (minimum of 4 hours) and simultaneous observation of clearly-defined E-region backscatter by both radars. That is, both radars needed to observe an E-region echo band that was clearly distinguishable from the F-region backscatter on range-time-intensity plots. The dates of the identified events were (in the YYYYMMDD format): 20130213 (18–21 UT), 20131008 (20–23 UT), 20140128 (15–22 UT), 20140216 (19–22 UT). The data were processed using standard SuperDARN criteria to eliminate the ground scatter. Ionospheric echoes with low signal-to-noise ratio $P < 3$ dB and large spectral width $W > 500$ m/s were also excluded from the data set to reduce undesirable contamination by noise and interference.

4.4 Dual Radar Observations of Polar *E*-Region Echoes

The Doppler velocity and spectral width are examined first to determine where, within the MCM and DCE short-range FoV ($r < 990$ km), the E- and F-region backscatter was observed. Figure 4.2 shows the velocity and width parameters in the form of fan plots for selected 10-min intervals during one event on February 16, 2014. Each row represents one 10-min frame, with the time of each frame indicated in the top-left corner of each row. The 10-min average (a) MCM and (b) DCE velocities are shown by the color of each radar cell, with the color bar given to the right of Figure 4.2. Figures 4.2c and 4.2d have the same format and show average spectral width.

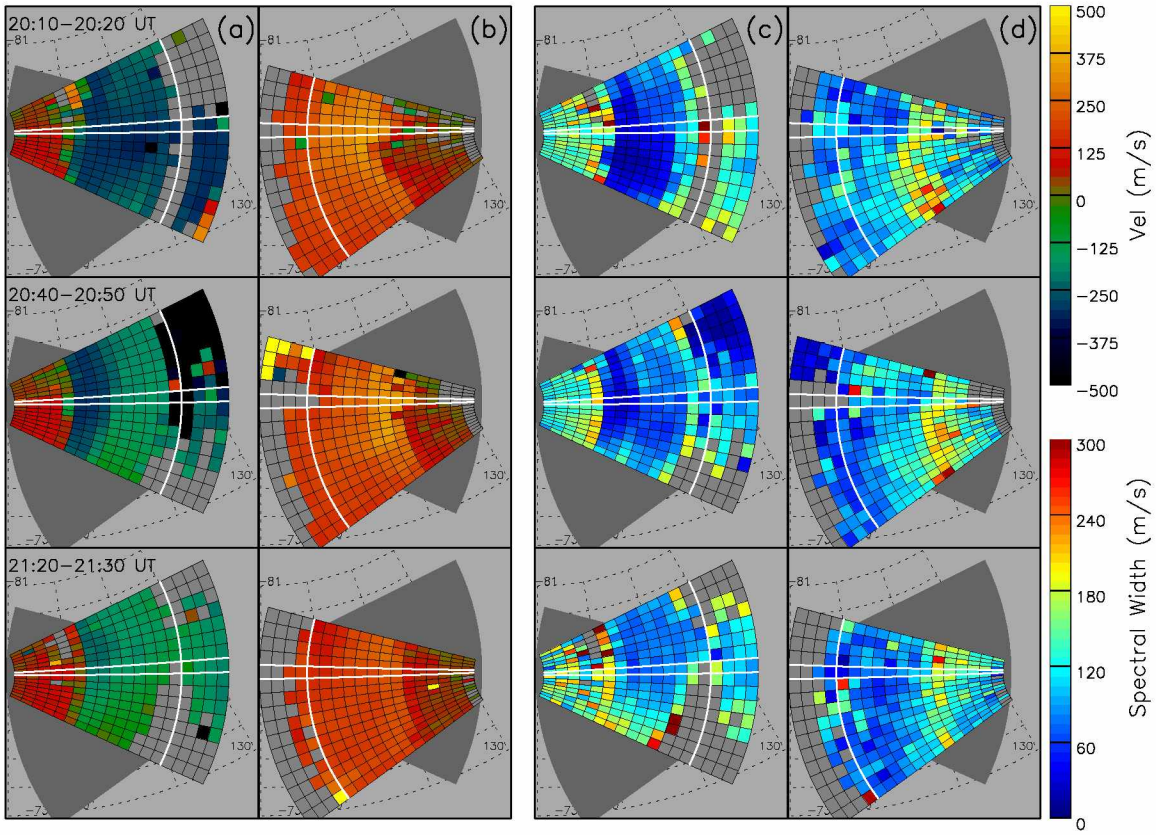

Figure 4.2. Doppler velocity and spectral width observed by MCM and DCE on February 16, 2014. First two columns show velocity data for (a) MCM and (b) DCE for 3 selected 10-min intervals with UT marked in the top-left corner of each row. Also shown are spectral widths for (c) MCM and (d) DCE in the same UT intervals. Beam 7 MCM (11 DCE) and a nominal boundary between the E and F regions are marked with white lines.

From Figure 4.2, both E- and F-region echoes were present during this event. The nominal boundary between the E- and F-region backscatter at 810 km is marked with a

white circular line. MCM observed a separation of echoes near this nominal boundary as a gap in the first frame and as a sharp increase in velocity magnitude in the second frame (green-to-black transition in the leftmost beams). This separation is much less obvious in DCE velocities, with no gap at 810 km and high-velocity echoes (yellow cells) observed only in the 3 rightmost beams in the second frame. Figure 4.2c and 4.2d show that both high and low spectral widths were observed during the event. The low-width echoes are observed in the same locations as the high-velocity echoes for both radars. Both radars also observed low-velocity, high-width echoes in the first five range gates. For MCM observations, velocity polarity was opposite to those of both "main" E region and F-region backscatter (red colors versus blue in Figure 4.2a). These features match well characteristics of the High Aspect angle Irregularity Region (HAIR) echoes [*Milan et al.*, 2004; *Drexler and St.-Maurice*, 2005].

The main E-region band of echoes can be identified in Figure 4.2 as those echoes that were observed between HAIR echoes and the F-region backscatter. Their velocities were relatively high in magnitude (250–400 m/s) and their widths were low (0–60 m/s). These are typical features of the E-region backscatter observed by SuperDARN [e.g. *Makarevich*, 2008, 2010]. From hereafter this band is referred to as "the E-region band" or, simply, "the band".

A gradual narrowing of the E-region band is observed from the first to the third frame. For example, MCM blue cells (< -300 m/s velocity) occupy the entire E region band in the first frame, while in the second frame they occupy only 3 range gates. The center of the band in range moved towards the radar from the first to the third frame. Importantly, this was observed for both radars, i.e. the E-region band observed by MCM moved closer to MCM, while the E-region band observed by DCE moved closer to DCE.

The following analysis focuses on velocity observations from aligned beams (7 MCM, 11 DCE) that are marked with white straight lines in Figure 4.2. In these velocity comparisons, the polarity of the velocity observed by MCM was reversed so that both parameters are positive in this presentation. A comparison of the MCM and DCE velocities is performed using two different approaches as described below.

The first approach involves a velocity comparison at the same horizontal locations, based on the standard mapping illustrated in Figure 4.1. For example, velocity measurements are compared between MCM range 405 km and DCE range 810 km. Thus in this approach a comparison of coincident measurements in the horizontal plane is conducted since these ranges refer to the same geographic location, but not necessarily the same altitude. The

velocity agreement at the same location is expected if the observed velocity is mostly controlled by the convection electric field.

In the second approach, velocities are compared between the same ranges for both radars. For example, MCM range 405 km is compared to DCE range 405 km. The agreement at the same range for both radars may be observed if velocity variations are strongly controlled by the altitude through its dependence on the range. In the following text, these two approaches are referred to as the *same-location* approach/comparison and the *same-range* approach/comparison, respectively.

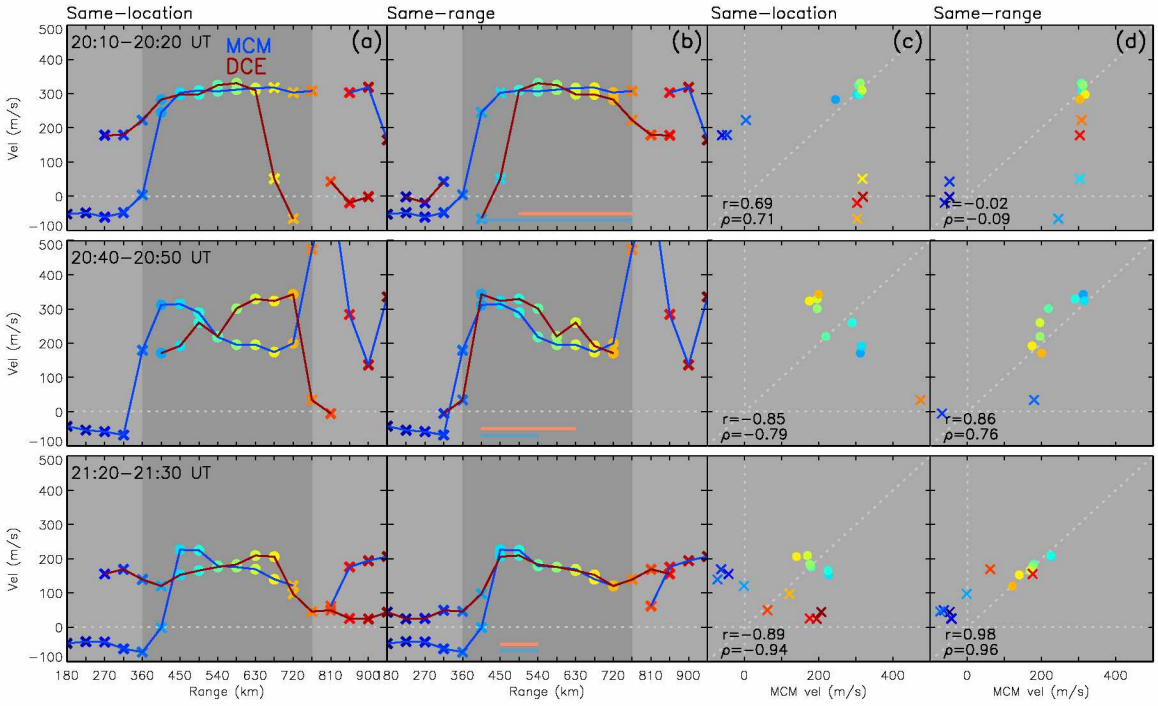

Figure 4.3. Velocity-range profiles in MCM beam 7 and DCE beam 11 using the same (a) location and (b) range approaches (see text for details). Each measurement is color-coded in range. Light blue and pink horizontal stripes in panel (b) show the MCM and DCE echo bands, respectively. Also shown are comparisons between MCM and DCE velocities at the same (c) locations and (d) ranges. Points that were included (excluded) in the correlation analysis are shown by circles (crosses). The values of linear correlation r and rank correlation ρ are shown in the bottom-left corner of panels (c) and (d). Three rows refer to the same UT intervals as in Figure 4.2.

Figure 4.3 presents results of velocity comparisons using both of these approaches for the same 10-min frames as those in Figure 4.2. The left two columns show velocity-range profiles using the same (a) location and (b) range approaches. The right two columns of Figure

4.3 show point-by-point velocity comparisons at the same (c) locations and (d) ranges. In both cases, a single point in Figures 4.3c or d is obtained by taking two velocity values from Figures 4.3a or b at the same x value. In Figures 4.3a and b, the solid blue (red) line shows the MCM (DCE) velocity range profile. Each point corresponds to measurements at one range gate and is color coded in the x value. Each point is also symbol-coded depending on whether the point is classified as an E-region echo for both radars or not, as described below. The color- and symbol-coding schemes are the same for Figures 4.3a and 4.3c to facilitate comparisons between these two presentations. Similarly, the coding schemes are the same for Figures 4.3b and 4.3d.

From Figure 4.1b, measurements refer to the E region for both MCM and DCE measurements only between ranges 360 and 810 km. These ranges are highlighted with dark grey background in Figures 4.3a and b and used in point classification. To further reduce HAIR contribution (that sometimes extended beyond 360 km), both velocities had to be greater than 100 m/s in magnitude. These two criteria were applied to separate the points into two groups: (1) when both radars sampled E region (showed as circles) and (2) when one radar sampled either HAIR or the F region (crosses). The first group only was then considered in the velocity correlation analysis, with both the linear correlation r and rank correlation ρ coefficients calculated and given in the bottom-left corner of each scatter plot.

Figure 4.3 shows that, at the start of the event, the E-region velocities exhibited some agreement between the same locations ($r = 0.69$, $\rho = 0.71$) and no agreement between the same ranges (-0.02, -0.09). By the third time frame, this changed into strong disagreement between the same locations (-0.89, -0.94) and very strong agreement between the same ranges (0.98, 0.96). The same feature of the same-location disagreement/same-range agreement is also present in the velocity profile plots for the second and third frames. Thus velocity profiles in the E-region ranges (dark gray color) resemble each other in Figure 4.3b. In the third frame they are almost identical. In contrast, in Figure 4.3a, they are a reflection of each other.

Another important feature in Figure 4.3 is that strengthening of the same-range agreement later in the event was associated with the E-region velocity profile becoming more narrow, less flat, and peaking at closer ranges. In order to further quantify this feature, the range extent of the E-region echo band near its peak was estimated as follows. The E-region velocity peak was found for each frame and the first range gates on both sides with velocities below 60% of this peak were taken as boundaries of this peak region. In the

following analysis, both the range with peak velocity and distance between these boundaries are considered. For brevity, these two parameters are referred to as the "band range" and the "band width". Figure 4.3 presents this information with two horizontal stripes at the bottom of column (b): blue for MCM and pink for DCE. Using this presentation, the above feature is clearly seen. For example, in the first frame, the MCM band was 8-gate wide with its center at 585 km and in the last frame it is only 2-gate wide centered at 495 km. The DCE band undergoes a similar transformation.

More insights into the nature of the transition between the two agreement cases and accompanying changes in the E-region band characteristics can be obtained by examining the E-region echo populations. A traditional way of doing this is by using the Watermann scatter plots [*Watermann et al.*, 1989]. Figure 4.4 shows the scatter plots of spectral width versus velocity for (a) MCM and (b) DCE. The same 10-min intervals are considered here as in Figures 4.2 and 4.3, with all individual 1-min measurements shown and color-coded in MCM range using the same color scheme as in Figure 4.3.

The HAIR echoes are also evident in Figure 4.4. These low-velocity echoes are represented by the dark blue points (short ranges). Their widths also have a relatively large spread in the vertical direction. Dark red points on MCM plots are most likely F-region echoes since they were detected at further ranges. It is interesting however, that they do not appear to differ significantly from the rest of non-HAIR echoes in the first frame, except for somewhat larger widths. The echoes at middle ranges (light blue to yellow) have velocities that are just below the nominal ion-acoustic speed ($C_s \approx 350$ m/s) in the first frame, but as the time progresses this population shifts towards lower velocities. It also splits into two different groups (light blue and green-yellow) that are inclined in opposite directions vertically (in this plot format). For example, the green-yellow population is inclined to the right, which means that as velocity increases the spectral width increases as well. This is in contrast with the first frame where the entire non-HAIR population was vertically straight. The point clustering in the DCE data is less clear, but separation between HAIR and non-HAIR echoes is still evident, as well as changes in the non-HAIR population with time. In particular, a general shift in the mid-range echoes towards lower velocities is similar to the MCM case. This shift for both MCM and DCE is consistent with a decrease in the cross-track component from the first to the second pass of DMSP, Figure 4.1a, although it is unknown whether this decrease was monotonic in time.

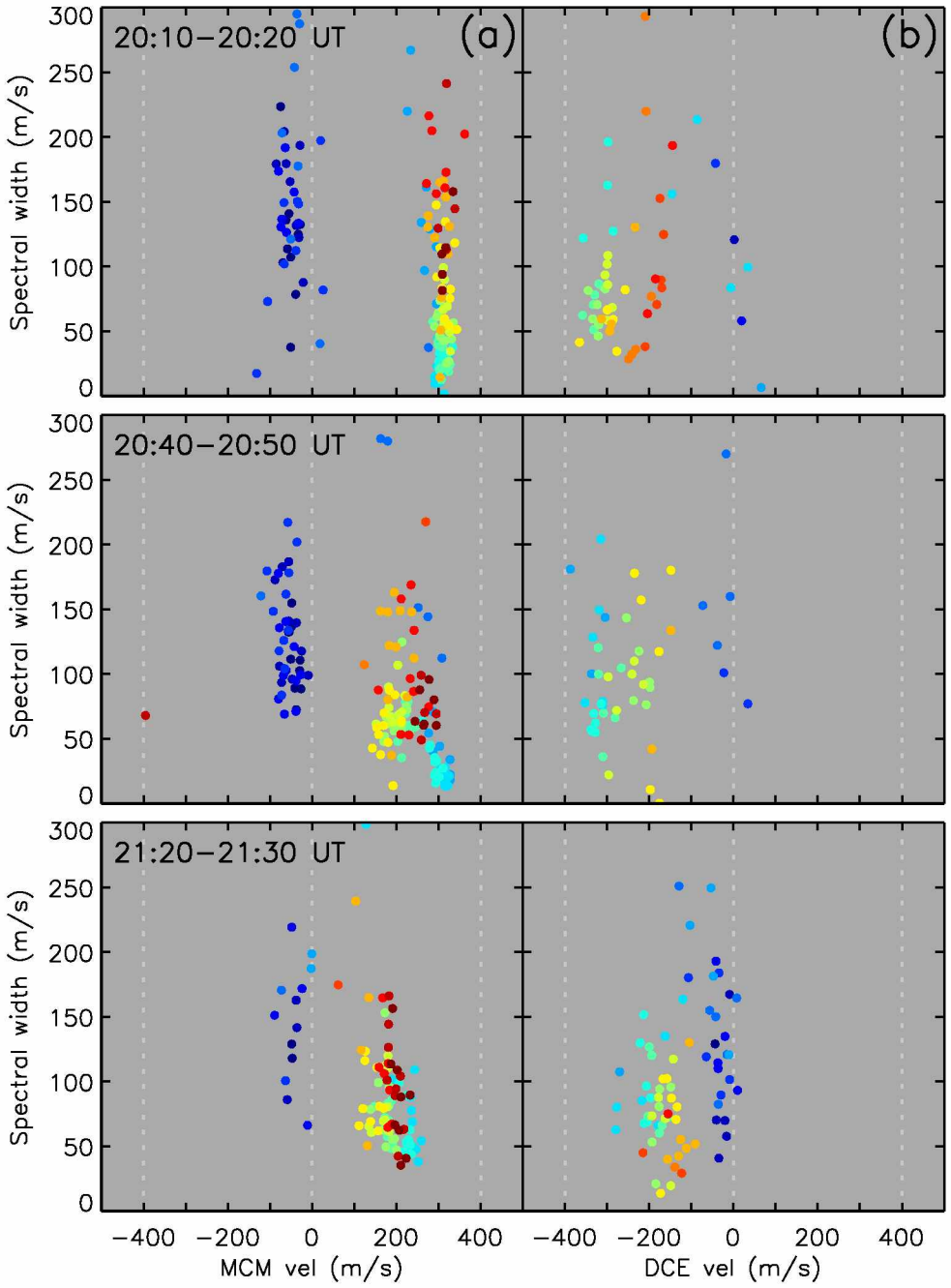

Figure 4.4. Scatter plots of spectral width versus (a) MCM and (b) DCE velocity during 3 selected intervals on February 16, 2014. The points are color-coded in range, with the same color scale as that in Figure 4.3. Three rows refer to the same UT intervals as in Figures 4.2 and 4.3.

4.5 Velocity and Band Characteristic Analysis for All Events

In the previous section, the evolution of the E-region irregularity characteristics was presented using selected time frames. Details of the estimates for derived parameters such as the E-region band width, the range position, and the velocity correlations were also presented. In this section, these derived parameters are further analyzed for the entire event on February 16, 2014 as well as for all 4 events considered together.

Figure 4.5 shows time variations of the E-region band (a) width and (b) range for MCM (blue) and DCE (red). Uncertainties for the band width (in number of gates) were taken to be $2 - (\Delta V_1 + \Delta V_2)/\Delta V_0$, where $\Delta V_{1,2}$ are the observed magnitudes of velocity jumps on the band edges and $\Delta V_0 = 300$ m/s. For cases with $\Delta V_1 + \Delta V_2 > \Delta V_0$, the uncertainty was taken to be 2 gates. In this way, the largest uncertainty is 2 gates or 90 km, and a velocity-range profile that is more similar to a step function would have the smaller uncertainty. These uncertainties are shown by the bars in Figure 4.5a. Figure 4.5b also shows the echo bands themselves by light blue and pink vertical stripes. This information is the same as that given by the horizontal stripes in Figure 4.3. Figure 4.5 also shows time variations of the (c) linear and (d) rank correlation coefficients. Black (white) lines show the velocity correlations between the same locations (ranges). All data points in panels (a) and (b) are slightly shifted (MCM to the left and DCE to the right) in time to prevent overlapping of the error bars and vertical stripes. The black data points in panels (c) and (d) are similarly shifted to the right.

The same general trend that was noticed before for the three frames presented in Figures 4.2 and 4.3 is more evident here. Namely, both radars observe decreases in both the band width and the band range with time, Figures 4.5a and b. At the same time, agreement measures show a transition between time periods when both correlation coefficients were quite variable (before 2030 UT) and time periods when a strong agreement was observed between the same ranges (after 2030 UT). During this later interval, velocities taken at the same ranges were strongly correlated, while velocities taken at the same locations were strongly anticorrelated.

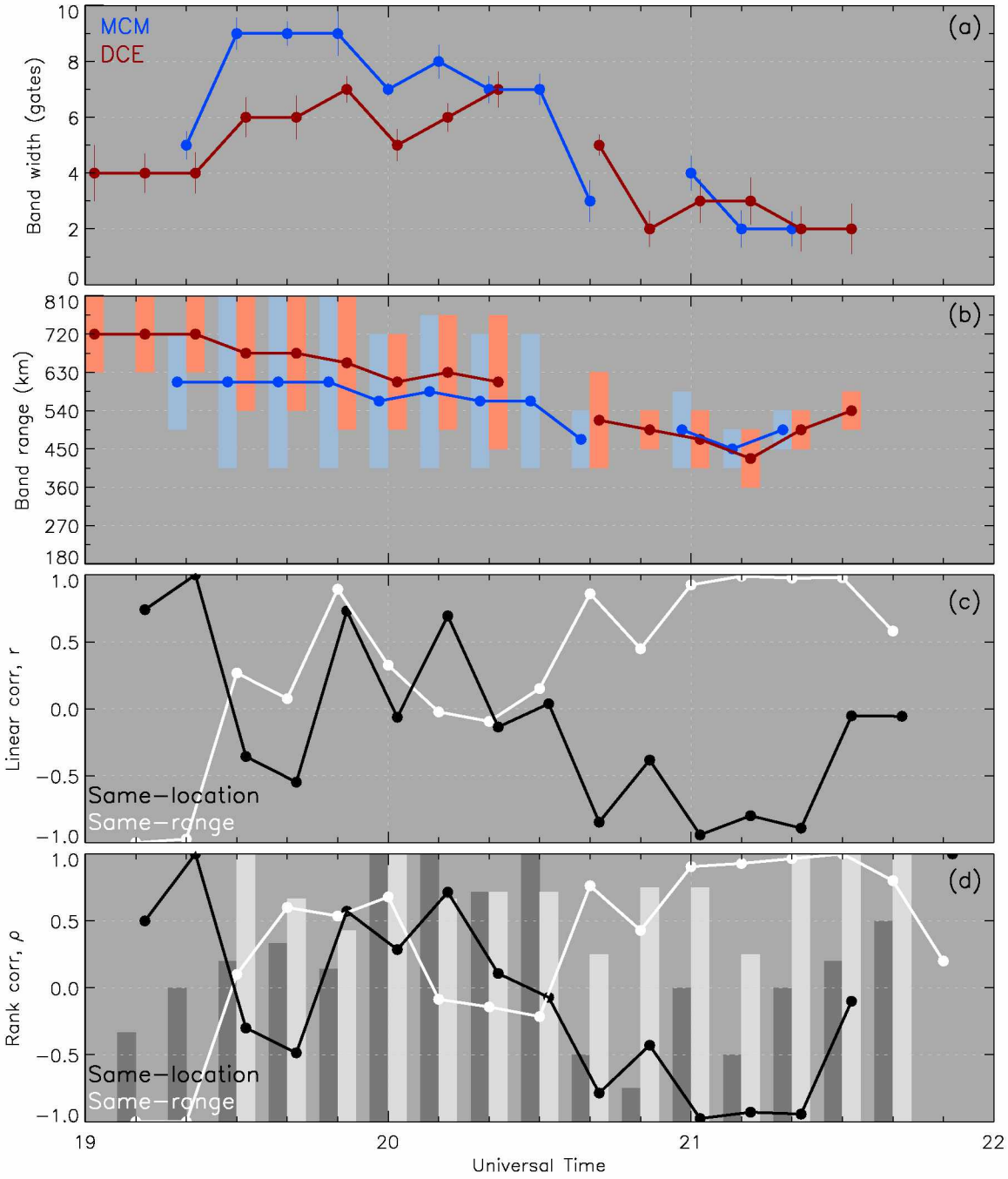

Figure 4.5. Time variation of the band (a) width and (b) range for MCM (blue) and DCE (red) on February 16, 2014, 19–22 UT. The uncertainties are shown as thin vertical lines. Figure 4.5b also shows the extent of the MCM (DCE) band by the light blue (red) bars. Also shown are time variations of the (c) linear r and (d) rank ρ correlation coefficients. The wide vertical stripes in Figures 4.5c and d show fractions of velocity measurements that agreed within uncertainty. Black (white) color represents correlations between the same locations (ranges).

Similar features are observed for the fraction of velocity measurements that agreed within the uncertainty shown by the wide vertical stripes. Before 2030 UT, there was no clear relationship between the black and white stripes. After 2030 UT, however, the white bars are higher than the black ones. This indicates that more velocities agreed between the same ranges. Thus results of the analysis using fractions of points that agreed within uncertainty agree well with those of the correlation analysis.

The event on February 16, 2014 was the only event out of all four that exhibited this clear transition from a wide band centered at mid-ranges to a narrow band that was located at shorter ranges, Figure 4.5a and b. Each event of other three fell into one of these two categories. The 1st event had a wide band, while the 2nd and 3rd events had a narrow band at shorter ranges. Nevertheless, the same analysis was conducted, with results presented in Figure 4.6.

Shown are scatter plots of the linear correlation coefficient r versus the band (a) width and (b) range for the 16 February 2014 event. Figures 4.6c and d present the same information but for the rank correlations ρ. As in Figure 4.5, the black (white) color represents the correlations between the same locations (ranges). The uncertainty in range is taken to be fixed at 2 range gates. Figures 4.6e–h are the same as Figures 4.6a–d, but they include data points from all four events. Linear fits in all panels are given by heavy lines.

All black lines have positive slopes indicating that the agreement between the same locations becomes stronger (more positive) with increasing band width and range. In contrast, the agreement between the same ranges becomes stronger when both band width and range decrease. The uncertainties in these slopes were also estimated and in all cases they were small enough for the slopes to be considered positive or negative within uncertainty. Thus the trend noticed in the 16 February 2014 event is consistent with the overall trend observed for all 4 events combined. The same result was also obtained by using the fractions of points that agreed within uncertainty (rather than r and ρ coefficients). One can conclude that the same-range agreement is observed when the E-region echo band is narrower and located at closer ranges. Importantly and unexpectedly, this is seen for both radars. That is, the MCM band moves closer to MCM, *at the same time* as the DCE band moves closer to DCE. A possible explanation for this and other observed features is offered next.

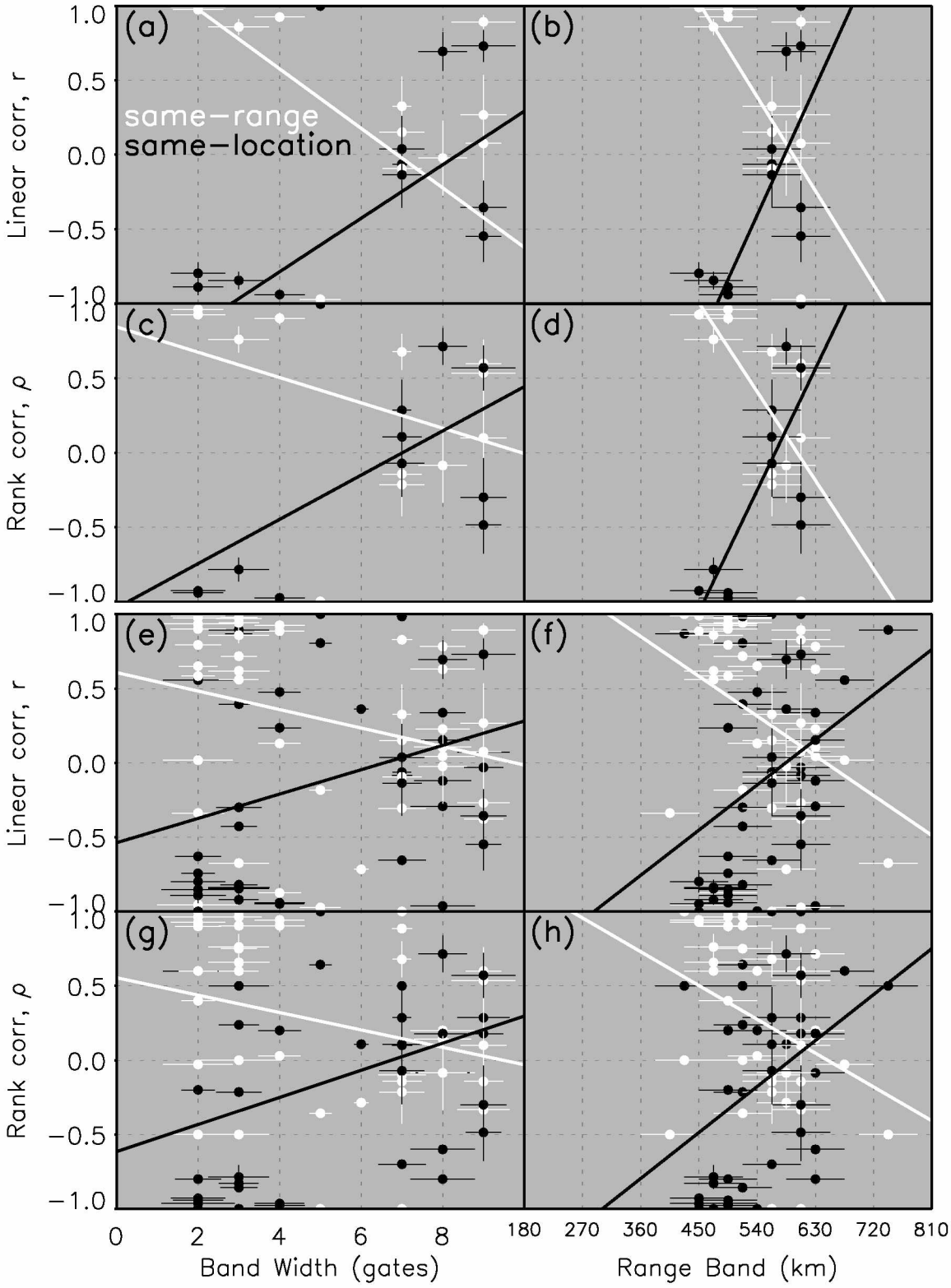

Figure 4.6. Linear correlation coefficient r versus the MCM band (a) range and (b) width on February 16, 2014. Linear fits are given by solid lines. The white (black) color represents the same-range (same-location) approach. Also shown are rank correlation coefficient ρ versus the MCM band (c) range and (d) width. Panels (e)–(h) show the same as panels (a)–(d), but for all four events.

4.6 HF Radio Propagation in the Southern Polar Cap

In order to obtain further insight into the origins and characteristics of short-range ionospheric echoes observed with the MCM-DCE dual radar combination, raytracing simulations were conducted for several sets of electron density conditions. Raytracing simulations are routinely used in studies of HF radio propagation in the ionosphere including the polar cap [e.g. *Warrington et al.*, 2012]. They are also used in conjunction with SuperDARN observations for pinpointing vertical positions of backscatter [*Koustov et al.*, 2007], interpreting echo occurrence patterns [*de Larquier et al.*, 2013], and evaluating radar's technical capabilities [*Ponomarenko et al.*, 2009; *McDonald et al.*, 2013]. We employed a version of standard raytracing tools based on numerical solutions of the Hamiltonian ray path equations [*Haselgrove*, 1963; *Jones and Stephenson*, 1975] that allows the consideration of arbitrary density distributions. Figure 4.7 shows results of these simulations for aligned MCM-DCE beams using (a) IRI model densities on February 16, 2014, 2000 UT, (b) altitude-stratified Gaussian E layer, and (c) tilted Gaussian E layer. Rays within the typical range of elevation angles for SuperDARN measurements of 10°–30° were found under the assumption of ordinary mode propagation. In both Figures 4.7b and 4.7c, the same peak altitude h0E of 110 km, peak E-region density NmE of $1.2{\times}10^5$ cm^{-3}, and layer thickness factor of 20 km were used. In Figure 4.7c, a tilt of 5 km across $\Delta x = 1150$ km was used, i.e. h0E linearly increases from 110 km at $x = 0$ km to 115 km at $x = 1150$ km. The insert in each panel shows the aspect angle α variation with range at an altitude of 105 km. These points were obtained by plotting α values on ray paths that were closest to 105 km and within 5 km; a small jump in α is sometimes observed due to a finite elevation resolution when a jump between adjacent rays occurs. A reference height of 105 km was used for this presentation since it was close to the height with $\alpha \approx 0$ in case (b); at 110 km, the α variation with range was very similar but shifted from zero.

Figure 4.7a shows that no orthogonality is reached anywhere in the E region, with typical aspect angles α of 6°–20° for MCM and similarly-large α for DCE. No E-region irregularities are expected to be generated by FBI or GDI in the linear regime at such large aspect angles. Figure 4.7b shows a crescent-shaped area (pink) where orthogonality is reached for MCM observations in the E region at a slant range of 450 km and beyond. To keep the diagram readable, the orthogonality area is not shown for DCE, but it was very similar to that for MCM only reflected about $x = 550$ km. The orthogonality area is quite extended in the x-distance and slant range, with minimal changes in the altitude of the top

part of the crescent. This case represents a clear example of the Pedersen ray propagation, where one ray does not change its altitude and orientation with vertically-oriented magnetic field throughout much of the simulation domain.

Moreover, we found that very similar features were present in a large number of other sets of density conditions (not presented here). This included IRI densities scaled up by a factor of 2–4 and most other altitude-stratified layers, i.e. those with larger NmE values and various thickness factors. Thus for most strong E layers, the Pedersen propagation mode was present and resulted in a crescent-shaped area of $\alpha < 0.5°$ whose top part was extended and relatively flat. It is really this top part that was located within the central E region (100–120 km) where strong density perturbations are expected. The bottom, descending part (below 100 km in altitude) is where orthogonality is reached but density perturbations are usually much smaller [e.g. *Pfaff et al.*, 1984].

The aspect angle variation with range at a given altitude was also minimal for these cases, similar to what is shown in the insert in Figure 4.7b, where it was near zero above the range of 450 km. Under these conditions, the observed velocity is expected to be controlled mostly by the convection velocity $\mathbf{V}_E$ variations, section 4.2, and for spatially uniform $\mathbf{V}_E$, a flat velocity profile is expected at ranges of 450 km and above. At ranges of 405 km and below, the aspect angles rise quickly in magnitude and the observed velocities are expected to be much reduced. Thus the Pedersen propagation case shown in Figure 4.7b corresponds well to the observed velocity variation with range shown in the first row of Figure 4.3a. In a more general case of spatially non-uniform $\mathbf{V}_E = (V_E, \theta)$, velocity will be higher for larger V_E and/or smaller θ, but for each pair of range values it will be the same and hence a velocity agreement will be seen at the same locations.

Figure 4.7c presents an example of a relatively small (and presumably less frequently seen) subset of strong E layer conditions without the Pedersen mode. In this case, the layer is slightly tilted. Even though a similar crescent-shaped area is present, its top is less extended and not flat. Instead, its altitude gradually increases with range, or with x-distance. The increase is small but noticeable, in particular for ranges of interest above 450 km. One might think that a crescent in case (c) is simply shifted up to ~ 110 km from case (b), but it is more than that. It is also slightly tilted so that an increase continues beyond $x = 600$ km, however slowly. This can be seen perhaps more clearly as a slow but noticeable change in α with range (insert in panel c). Rather than being nearly constant as in Figure 4.7b starting from 450 km in range, aspect angle is monotonically increasing

(ignoring jumps between rays due to finite elevation resolution).

In this propagation mode and under uniform $\mathbf{V}_E$ conditions, the observed velocity variation with range is mostly controlled by this quasi-steady change in the aspect angle. Velocity is expected to be at maximum at $\alpha = 0$ and to decrease on both sides, quickly towards smaller ranges and more gradually towards larger ranges. Thus this is representative of MCM velocity profiles shown in the second and third rows of Figure 4.3. For DCE, α variation with range is also monotonic, except that at lower x values < 450 km (larger DCE ranges) α starts to approach zero again. This is actually consistent with a slight increase in DCE velocity in Figure 4.3b (third frame) at ranges 720–810 km. One can conclude therefore that this propagation mode can explain both the "reflection" feature and the same-location agreement observed in Figures 4.3 (second and third frames). In short, velocity variation with range that is flat (tilted) corresponds to a flat (tilted) irregularity layer, where by "irregularity layer" we mean the locations where orthogonality is reached in the central E region (100–120 km). Raytracing simulations also suggest that a flat (tilted) irregularity layer is produced by a flat (tilted) density layer.

4.7 Discussion

This study represents the first investigation of E-region coherent backscatter from the southern polar cap using a dual HF radar setup. Moreover, a novel aspect of this study is that both radars observe the same locations from two opposite directions, which provides an excellent opportunity to examine relative importance of different factors in controlling irregularity characteristics. In particular, it is expected that the convection electric fields or, equivalently, the convection velocity $\mathbf{V}_E$ will be the same at the same location and the ratio of the Doppler velocities measured by two radars will be close to 1 if other factors are approximately the same. Amongst these the aspect angle and height variations are most important factors to consider, with both being strongly dependent on ionospheric propagation conditions. In the polar cap, it is mostly spatial distribution of background electron density that determines propagation modes since the magnetic field is almost vertical.

Geometric aspect angles (i.e. assuming straight-line propagation) for the E-region observations in the polar cap are very large. If the plasma density and the associated refraction are small, a radar ray will not reach orthogonality with the magnetic field (aspect angles still large) and no backscatter will be observed. For strong E layers, on the other hand, a Pedersen propagation mode is possible where a radar ray will travel long distances across the polar cap without changing its perpendicular orientation with respect to the magnetic field and backscatter will be observed in large spatial areas. It is this "all or nothing" aspect of E-region observations in the polar cap and the associated convolution of radio- and plasma-physical factors that makes analysis task particularly challenging and insightful at the same time. Below we further detail some of these challenges and insights.

4.7.1 Plasma Density Conditions: Normal versus Strong E Layers

A common set of assumptions about E-region irregularities is that they occur in a relatively narrow altitudinal layer centered near 110 km, propagate at small aspect angles α, and therefore would be observed in a radar's FoV as a band near a line of constant $\alpha = 0$ at 110 km [e.g. *Koustov et al.*, 2001]. Radar observations in the auroral E region are generally consistent with this idea, particularly for radars where aspect angle conditions are quite favorable (a case of small geometric aspect angles) [e.g. *Koustov et al.*, 2001; *Makarevich*, 2010]. In this case orthogonality with the magnetic field is achieved for most density conditions. When density is low, refraction is negligible and aspect angles are close to geometric ones. Stronger density will simply result in locations with small α moving

closer to the radar in range because of stronger refraction. One can illustrate this feature by comparing aspect angle behavior between inserts in Figures 4.7a and b, where the aspect angle curve for MCM (dark red) moves towards shorter ranges between Figure 4.7a and Figure 4.7b, at least in the part that has similar α values (strongly-negative).

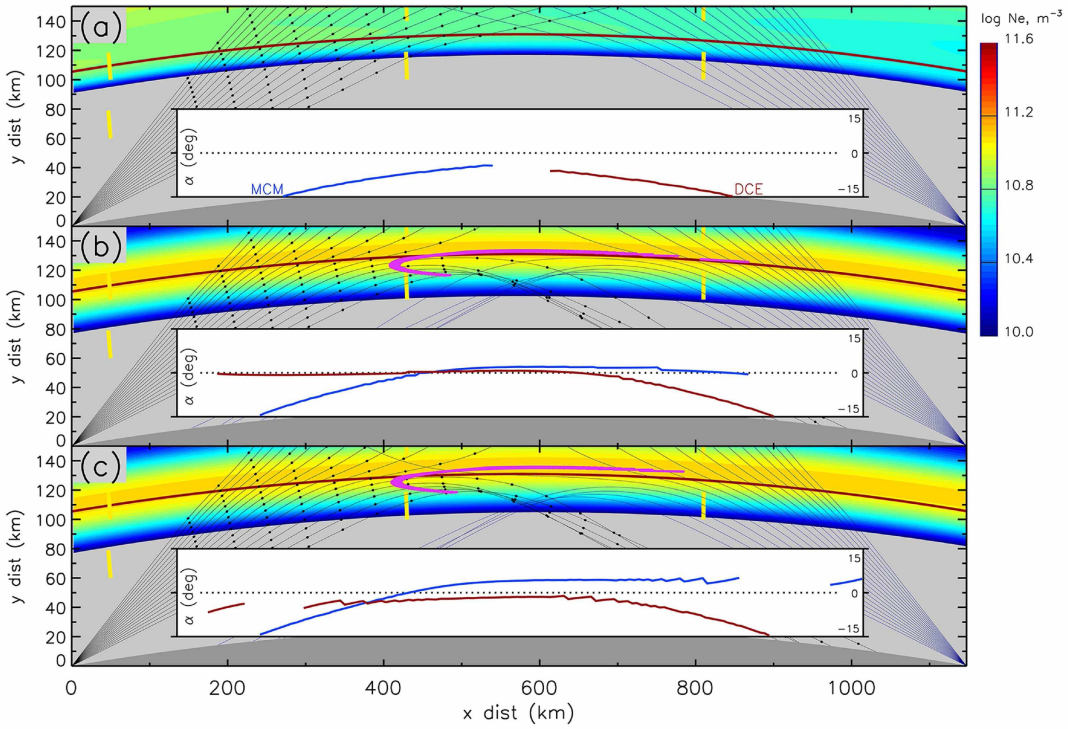

Figure 4.7. Raytracing simulation results for (a) IRI electron densities, (b) altitude-stratified Gaussian E layer, and (c) tilted Gaussian E layer. The background contours show the electron density in logarithmic scale. The heavy red line shows a constant reference height of 105 km. Also shown are the ray paths for MCM beam 7 (black thin lines) and DCE beam 11 (dark blue), with black dots indicating the start of range gates for MCM. The yellow lines show representative magnetic field directions. The pink lines show the locations where the MCM aspect angle $\mid \alpha \mid < 0.5°$. The insert in each panel shows the aspect angle variation with range at 105 km in altitude. Higher ray resolution was used for aspect angle analysis.

The important difference with the above-described auroral backscatter case is that, for the polar cap backscatter, it was only the case of a relatively strong E layer of Figure 4.7b that produced locations with $\alpha \approx 0$ (pink area). In the absence of such a strong layer, i.e. under "normal" or IRI-produced density conditions, no locations with $\alpha \approx 0$ were seen in raytracing results, Figure 4.7a. This points towards stronger role of density conditions as compared with most auroral observations.

Using notations introduced in section 4.2, irregularity velocity can be described as $V_{\rm irr}(V_E, \theta, \alpha, h, f_{\rm rad})$. The above argument leads to the treatment of the aspect angle variable α as an implicit function of the electron density N_e. The strong role of N_e in the E-region velocity observations in the polar cap occurs through this implicit control of α.

4.7.2 Plasma Density Conditions: Stratified versus Tilted Layers

A closely related issue is that of the dependence on the height h. As discussed above, previous studies often utilized the assumption about a fixed altitude or narrow altitudinal range and attributed velocity variations with range to aspect angle variations with distance at that altitude [*Koustov et al.*, 2001, 2002; *Makarevich*, 2010]. This is a reasonable assumption in the auroral region, based on in situ observations of density perturbations [*Pfaff et al.*, 1984] and the fact that radar rays are mostly inclined and hence pass through this irregularity layer and achieve orthogonality with inclined magnetic field lines in the narrow band of ranges. In other words, in the auroral region the irregularity layer sampled by the radar is narrow in range and fixed in height.

The important new result of the current study is that, in the polar cap, the sampled irregularity layer can be reasonably flat in height and extended in range, Figure 4.7b. This is achieved for strong and altitude-stratified E layers that produce Pedersen mode propagation. The strongest evidence for this interpretation was observations of flat and extended high-velocity echo bands by both MCM and DCE, Figures 4.2 and 4.3. Another important new result was that the Pedersen mode was present for an unexpectedly large subset of strong density conditions.

One example where it was not present was a tilted E layer, Figure 4.7c. In this case, the area of orthogonality was more similar to what is normally observed in the auroral region, with aspect angle monotonically changing at a given altitude. In this case, a radar also samples progressively larger altitudes or progressively larger aspect angles if the same altitude is considered, once zero aspect is achieved. In this case, the echo band is narrow in range, also similar to the auroral region. Thus the two cases of the stratified and tilted layers would respectively refer to the two cases of constant and monotonically increasing height h. Moreover, the aspect angle α will behave in exactly the same way: as a constant in one case and monotonically changing in magnitude in the other case.

Ionospheric layer tilts have been extensively discussed in previous studies, mostly in context of long-range radio propagation experiments [*Stein*, 1958; *Huang and Reinisch*, 2006]

and observations with coherent radars at lower VHF and HF [*Moorcroft*, 1989; *Uspensky et al.*, 1993, 1994]. *E*-layer tilts of 4°–5° over 50–100 km have been estimated by *Moorcroft* [1989] using previously-published data sets collected by an ISR system at Chatanika, Alaska and the S3-2 satellite [*de la Beaujardire and Vondrak*, 1982; *Vondrak and Rich*, 1982]. Using top values in these ranges, this translates to $\sim$ 10 km over 100 km, which means that our model tilt of 5 km over 1150 km is smaller by a factor of 5. This is likely to be more appropriate in the polar region, where precipitation effects (that may cause tilts) are less pronounced. One should also bear in mind that a specific tilt value or even its spatial uniformity are not that important. What is more significant is that tilted layers at various spatial scales/tilt magnitudes can create substantial deviations from the stratified ionosphere. This effectively eliminates the Pedersen mode propagation and results in monotonically changing aspect angle and height with range. Real tilts are likely to be smaller in spatial scale, but their combined effects will be similar to those modeled.

Tilted layers are often treated as a means to achieve orthogonality for *E*-region observations at large geometric aspect angles [e.g. *Moorcroft*, 1989]. This is a certain possibility for HF and even lower VHF (30–140 MHz) observations [*Uspensky et al.*, 1993], but probably not at UHF, where real aspect angles are large under realistic density conditions [*Jackel et al.*, 1997]. The current study demonstrated that tilted layers are not necessarily needed to achieve orthogonality using HF systems in the polar cap and, in fact, aspect conditions are more favorable for stratified layers since orthogonality is achieved in a larger number of range gates. Large geometric aspect angles become small after refraction is taken into account, with no need for additional bending due to the tilt.

4.7.3 Echo Bands and Spectral Populations

The final group of issues concerns irregularity spectral characteristics and possible differences between the auroral and polar *E*-region irregularities. An important observation in this context was that the evolution in echo band characteristics was associated with distinct changes in echo populations, Figure 4.4. In particular, velocities of the MCM high-velocity population were all close to each other in a wide band case (first frame), with lower and more scattered velocities seen with narrowing of the band (second and third frames). Changes in velocities were also accompanied by changes in spectral width, Figure 4.4. In the second frame, lower ranges within the *E*-region band (light blue points) showed a decreasing width with increasing velocity, while for larger ranges (green and yellow) width was increasing

with velocity. For the first group of points, the $W - V$ trend fits the idea of both velocity and width being related through the ion-acoustic speed as $V^2 + W^2 = C_s^2$ [*Hamza and St.-Maurice*, 1993], for the FBI waves. A narrow range of MCM velocities near nominal C_s in the first frame in Figure 4.4 also suggests that these were FBI waves. In addition, DMSP measurements of the convection velocity component also indicated that FBI was operational during a significant portion of the event, since the cross-track velocities exceeded nominal C_s during both passes near the MCM-DCE FoV, Figure 4.1a.

A clear clustering of MCM velocities near zero and 320 m/s in the first frame of Figure 4.4 is perhaps most significant in context of differences between irregularity generation between auroral and polar latitudes. While these two populations are well known for auroral observations [e.g. *Milan and Lester*, 1999; *Makarevich*, 2008], the important difference is that this low-velocity population in our case were HAIR echoes at very short ranges. This suggests that both were of the FBI origin: the high-velocity echoes were observed at small aspect angles, while HAIR echoes were FBI waves with attenuated velocities at large aspect angles [*Milan et al.*, 2004]. This provides some support to the view that, in the polar cap, unfavorable gradient orientations can result in no echoes produced by GDI [*Hanuise*, 1983]. This is somewhat contrary to previous studies in the northern polar cap that reported significant presence of low-velocity HF echoes [*Carter et al.*, 2012] and their VHF counterparts, Type II echoes [*Kustov et al.*, 1994].

The current observations also indicate that no low-velocity (and non-HAIR) echoes were observed only for wide echo bands. In the narrow-band case, the high-velocity echo population splits into two groups, with the second group (green and yellow points in Figure 4.4) showing lower velocities around 200 km and slightly higher widths. The auroral echoes with these characteristics have been interpreted as GDI waves [*Milan and Lester*, 1999] or gradient-destabilized FBI waves [*Milan and Lester*, 2001]. In this context it makes sense that a second group appears in the narrow-band/tilted-layer case since it is the tilted ionosphere that has larger along-the-beam gradients in density, section 4.6. Ultimately, it is the plasma density gradients that cause greater refraction and reduce effects of the Pedersen propagation. Thus large-scale characteristics of E-region backscatter (e.g. echo band width) may be more closely related to small-scale echo characteristics (e.g. echo velocity and width) than perhaps previously thought.

4.8 Summary and Conclusions

Dual HF radar observations of plasma irregularities in the polar E region indicate the following:

1. E-region coherent backscatter from the polar cap is a recurring observational feature seen simultaneously by both radars, despite highly unfavorable aspect conditions. E-region echoes occur in bands of variable range extent and position when E-region ionization levels are particularly strong. Analysis of irregularity velocities observed by two radars probing the E region from opposite directions confirm expectations based on previous radar investigations at auroral latitudes that E-region velocity depends on plasma convection velocity, aspect angle, and height of the scattering volume. At the same time, radar observations and raytracing simulations reveal that relative importance of these factors depends strongly on propagation/density conditions in the polar cap.

2. Velocities observed by two radars exhibit considerable agreement in the following two cases. In the first case, comparisons are conducted for the radar ranges that refer to the same physical location, but not necessarily the same altitude. The same-location agreement occurs when both radars observe wide echo bands, with strong and altitude-stratified E layers likely being responsible. In this case, the Pedersen mode dominates propagation within the polar E-region ionosphere producing extended areas within which ray paths are orthogonal to the magnetic field and from which E-region backscatter is received. With both aspect angle and height being constant, velocity variations are mostly controlled by those of the convection electric field, as expected. However, in other cases, strong velocity agreement is unexpectedly observed when velocities are taken at the same range for both radars. The same-range agreement occurs for narrow bands, with raytracing results suggesting that tilted layers are responsible. In that case, aspect angle and height change monotonically with range and control velocity behavior. Tilted layers are not necessary, however, and, in fact, somewhat detrimental for achieving orthogonality in strong E layers.

3. Polar E-region echoes are largely similar to their auroral counterparts in their spectral characteristics and echo populations, with both high-velocity echoes near nominal ion-acoustic speed and low-velocity echoes near zero velocity observed. However, in some cases the low-velocity echoes were only observed at high aspect angles, implying that one echo population is possibly missing as compared with auroral observations. These low-velocity, small-aspect echoes have been often attributed to the gradient-drift instability in previous studies. The observations provide indirect support to the view that unfavorable gradient

orientations in the polar cap may be responsible for absence of GDI waves.

Acknowledgements

This work was supported by National Science Foundation grants ANT-1139806 and AGS-1341902. SuperDARN data are freely available through the SuperDARN website at Virginia Polytechnic Institute and State University http://vt.superdarn.org/. The International Reference Ionosphere model is sponsored by the Committee on Space Research (COSPAR) and the International Union of Radio Science (URSI). Fortran source code for IRI 2007 is freely available for download from the Community Coordinated Modeling Center (CCMC) at http://ccmc.gsfc.nasa.gov/. The authors thank W. A. Bristow for providing the original Fortran source code for raytracing simulations. The developed Interactive Data Language raytracing code is available from the corresponding author.

4.9 References

Carter, B. A., and R. A. Makarevich (2009), E-region decameter-scale plasma waves observed by the dual TIGER HF radars, *Ann. Geophysicae*, *27*, 261–278.

Carter, B. A., R. A. Makarevich, J. C. Devlin, and A. J. McDonald (2012), Coincident multi-point observations of the E- and F-region decametre-scale plasma waves at high latitudes, *J. Atmos. Sol. Terr. Phys.*, *80*, 323–335.

Chisham, G., T. K. Yeoman, and G. J. Sofko (2008), Mapping ionospheric backscatter measured by the SuperDARN HF radars - Part 1: A new empirical virtual height model, *Ann. Geophysicae*, *26*, 823–841.

Chisham, G., et al. (2007), A decade of the Super Dual Auroral Radar Network (SuperDARN): scientific achievements, new techniques and future directions, *Surveys in Geophysics*, *28*, 33–109, doi:10.1007/s10712-007-9017-8.

Davies, K. (1990), *Ionospheric Radio*, IEE Electromagnetic Waves Series 31, Peter Peregrinus Ltd., London.

de la Beaujardire, O., and R. Vondrak (1982), Chatanika Radar observations of the electrostatic potential distribution of an auroral arc, *J. Geophys. Res.*, *87*(A2), 797–809.

de Larquier, S., P. Ponomarenko, A. J. Ribeiro, J. M. Ruohoniemi, J. B. H. Baker, K. T. Sterne, and M. Lester (2013), On the spatial distribution of decameter-scale subauroral ionospheric irregularities observed by SuperDARN radars, *J. Geophys. Res.*, *118*, 5244–5254, doi:10.1002/jgra.50475.

Drexler, J., and J.-P. St.-Maurice (2005), A possible origin for large aspect angle HAIR echoes seen by SuperDARN radars in the E region, *Ann. Geophysicae*, *23*, 767–772.

Fejer, B. G., and M. C. Kelley (1980), Ionospheric irregularities, *Geophys. Rev.*, *18*, 401–454.

Greenwald, R. A., W. Weiss, E. Nielsen, and N. R. Thomson (1978), STARE: A new radar auroral backscatter in Northern Scandinavia, *Radio Sci.*, *13*, 1021–1029.

Greenwald, R. A., et al. (1995), DARN/SuperDARN: A global view of the dynamics of high-latitude convection, *Space Sci. Rev.*, *71*, 763–796.

Haldoupis, C. (1989), A review on radio studies of auroral E region ionospheric irregularities, *Ann. Geophysicae*, *7*, 239–258.

Hamza, A. M., and J.-P. St.-Maurice (1993), A turbulent theoretical framework for the study of current-driven E region irregularities at high latitudes: Basic derivation and application to gradient-free situations, *J. Geophys. Res.*, *98*, 11,587–11,599.

Hanuise, C. (1983), High latitude ionospheric irregularities, *Radio Sci.*, *18*, 1093–1121.

Haselgrove, J. (1963), The hamiltonian ray path equations, *J. Atmos. Terr. Phys.*, *25*, 397–399.

Huang, X., and B. W. Reinisch (2006), Real-time HF ray tracing through a tilted ionosphere, *Radio Sci.*, *41*, RS5S47, doi:10.1029/2005RS003378.

Jackel, B., D. Moorcroft, and K. Schlegel (1997), Characteristics of very large aspect angle E-region coherent echoes at 933 MHz, *Ann. Geophysicae*, *15*, 54–62.

Jones, R. M., and J. J. Stephenson (1975), A versatile three dimensional ray tracing computer program for radio waves in the ionosphere, *OT Report 75-76, US Dep. of Comm., Washington, DC, USA*.

Koustov, A. V., K. Igarashi, D. André, K. Ohtaka, N. Sato, H. Yamagishi, and A. Yukimatu (2001), Observations of 50- and 12-MHz auroral coherent echoes at the Antarctic Syowa station, *J. Geophys. Res.*, *106*, 12,875–12,887.

Koustov, A. V., D. W. Danskin, M. V. Uspensky, T. Ogawa, P. Janhunen, N. Nishitani, S. Nozawa, M. Lester, and S. Milan (2002), Velocities of auroral coherent echoes at 12 and 144 MHz, *Ann. Geophysicae*, *20*, 1647–1662.

Koustov, A. V., D. André, E. Turunen, T. Raito, and S. E. Milan (2007), Heights of SuperDARN F region echoes estimated from the analysis of HF radio wave propagation, *Ann. Geophysicae*, *25*, 1987–1994, doi:10.5194/angeo-25-1987-2007.

Kustov, A. V., J. A. Koehler, G. J. Sofko, D. W. Danskin, and M. J. McKibben (1994), Observations of 50-MHz type-II coherent echoes from within the polar cap, *Ann. Geophysicae*, *12*(8), 765–774.

Kustov, A. V., J. A. Koehler, G. J. Sofko, and D. W. Danskin (1996), The SAPPHIRE-North radar experiment: Observations of discrete and diffuse echoes, *J. Geophys. Res.*, *101*, 7973–7986.

Makarevich, R. A. (2008), HF radar observations of high-velocity *E*-region echoes from the eastward auroral electrojet, *J. Geophys. Res.*, *113*, A09321, doi:10.1029/2008JA013204.

Makarevich, R. A. (2009), Coherent radar measurements of the Doppler velocity in the auroral E region, *Radio Science Bulletin*, *327*, 33–46.

Makarevich, R. A. (2010), On the occurrence of high-velocity E-region echoes in Super-DARN observations, *J. Geophys. Res.*, *115*, A07302, doi:10.1029/2009JA014698.

Makarevitch, R. A., T. Ogawa, K. Igarashi, A. V. Koustov, N. Sato, K. Ohtaka, H. Yamagishi, and A. Yukimatu (2001), On the power-velocity relationship for 12- and 50-MHz auroral coherent echoes, *J. Geophys. Res.*, *106*, 15,455–15,470.

McDonald, A. J., J. Whittington, S. de Larquier, E. Custovic, T. A. Kane, and J. C. Devlin (2013), Elevation angle-of-arrival determination for a standard and a modified superDARN HF radar layout, *Radio Sci.*, *48*, 709–721, doi:10.1002/2013RS005157.

Milan, S. E., and M. Lester (1999), Spectral and flow angle characteristics of backscatter from decametre irregularities in the auroral electrojets, *Adv. Space Res.*, *23*, 1773–1776.

Milan, S. E., and M. Lester (2001), A classification of spectral populations observed in HF radar backscatter from the E region auroral electrojets, *Ann. Geophysicae*, *19*, 189–204.

Milan, S. E., M. Lester, T. K. Yeoman, T. R. Robinson, M. V. Uspensky, and J.-P. Villain (2004), HF radar observations of high-aspect angle backscatter from the E region, *Ann. Geophysicae*, *22*, 829–847.

Moorcroft, D. R. (1989), Reflection and refraction by tilted layers: An explanation for VHF auroral backscatter at large aspect angles, *Geophys. Res. Lett.*, *16*(3), 235–238.

Nielsen, E., and K. Schlegel (1983), A first comparison of STARE and EISCAT electron drift velocity measurements, *J. Geophys. Res.*, *88*, 5745–5750.

Nielsen, E., C. F. del Pozo, and P. J. S. Williams (2002), VHF coherent radar signals from the E region ionosphere and the relationship to electron drift velocity and ion acoustic velocity, *J. Geophys. Res.*, *107*, 1012, doi:10.1029/2001JA900111.

Pfaff, R. F., M. C. Kelley, B. G. Fejer, E. Kudeki, C. W. Carlson, A. Pedersen, and B. Hausler (1984), Electric field and plasma density measurements in the auroral electrojet, *J. Geophys. Res.*, *89*, 236–244.

Ponomarenko, P. V., J.-P. St-Maurice, C. L. Waters, R. G. Gillies, and A. V. Koustov (2009), Refractive index effects on the scatter volume location and Doppler velocity estimates of ionospheric HF backscatter echoes, *Ann. Geophysicae*, *27*, 4207–4219, doi:10.5194/angeo-27-4207-2009.

Rich, F. J., and M. Hairston (1994), Large-scale convection patterns observed by DMSP, *J. Geophys. Res.*, *99*, 3827–3844.

Sahr, J., and B. G. Fejer (1996), Auroral electrojet plasma irregularity theory and experiment: A critical review of present understanding and future directions, *J. Geophys. Res.*, *101*, 26,893–26,909.

Schlegel, K. (1996), Coherent backscatter from ionospheric E-region plasma irregularities, *J. Atmos. Terr. Phys.*, *58*, 933–941.

Shepherd, S. G. (2014), Altitude-adjusted corrected geomagnetic coordinates: Definition and functional approximations, *J. Geophys. Res.*, *119*(9), 7501–7521, doi:10.1002/2014JA020264.

Stein, S. (1958), The role of ionospheric-layer tilts in long-range high-frequency radio propagation, *J. Geophys. Res.*, *63*, 217–241.

Uspensky, M., A. Kustov, and P. Williams (1993), The amplitude of auroral backscatter - III. Effect of tilted ionospheric layer, *Planet. Space Sci.*, *55*(10), 1383–1392.

Uspensky, M. V., A. V. Kustov, G. J. Sofko, J. A. Koehler, J.-P. Villain, C. Hanuise, J. M. Ruohoniemi, and P. J. S. Williams (1994), Ionospheric refraction effects in slant range profiles of auroral HF coherent echoes, *Radio Sci.*, *29*, 503–517.

Vondrak, R. R., and F. J. Rich (1982), Simultaneous Chatanika radar and S3-2 satellite measurements of ionospheric electrodynamics in the diffuse aurora, *J. Geophys. Res.*, *87*, 6173–6185.

Warrington, E. M., N. Y. Zaalov, J. S. Naylor, and A. J. Stocker (2012), HF propagation modeling within the polar ionosphere, *Radio Sci.*, *47*, RS0L13, doi:10.1029/2011RS004909.

Watermann, J., A. G. McNamara, G. J. Sofko, and J. A. Koehler (1989), Distribution of mean Doppler shift, spectral width and skewness of coherent 50-MHz auroral radar backscatter, *J. Geophys. Res.*, *94*, 6979–6985.

Chapter 5

Global View of the *E*-Region Irregularity and Convection Velocities in the High-Latitude Southern Hemisphere [I]

5.1 Abstract

Occurrence of the E-region plasma irregularities is investigated using two Super Dual Auroral Radar Network (SuperDARN) South Pole (SPS) and Zhongshan (ZHO) radars that sample the same magnetic latitude deep within the high-latitude plasma convection pattern but from two opposite directions. It is shown that the SPS and ZHO velocity distributions and their variations with the magnetic local time are different, with each distribution being asymmetric, i.e. a particular velocity polarity is predominant. This asymmetry in the E-region velocity distribution is associated with the bump-on-tail of the distribution near the nominal ion-acoustic speed C_s that is most likely due to the Farley-Buneman instability (FBI) echoes or an inflection point of the distribution below nominal C_s that is most likely due to the gradient-drift instability echoes. In contrast, the distribution of the convection velocity component was found to be symmetric, i.e. with no bump-on-tail or an inflection point, but with a bias (i.e. uniform shift) toward a particular polarity. It is demonstrated that the asymmetry in the convection pattern between the eastward and westward zonal component is unexpectedly strong, with the westward zonal component being predominant, especially at lower latitudes, while also exhibiting a strong IMF B_y dependence. The observations are consistent with the notion that the asymmetry in the E-region velocity distribution is highly sensitive to the bias in the convection component caused by the zonal convection component asymmetry and that the bump-on-tail or inflection point features may also depend on the irregularity height and the presence of strong density gradients modifying the FBI threshold value.

[I]Published as: Forsythe V.V, and R.A Makarevich (2017), Global view of the E-region irregularity and convection velocities in the high-latitude southern hemisphere, *J. Geophys. Res. Space Physics*, *122*, doi:10.1002/2016JA023711.

5.2 Introduction

The interaction between the Interplanetary Magnetic Field (IMF) and the Earth's magnetosphere creates the convection electric field that drives the motion of the ions and electrons in the F-region of the high-latitude ionosphere. In the E-region, the ions are collisional and the electrons are magnetized and therefore they exhibit different motions, creating ionospheric currents or electrojets. The differential motion between the ions and the electrons also triggers plasma instabilities in the E-region, including the Farley-Buneman instability (FBI) [*Farley*, 1963; *Buneman*, 1963].

Coherent scatter radars can receive echoes from the ionospheric density irregularities generated by FBI and those echoes can be identified by their narrow power spectra that are centered near the nominal ion-acoustic speed C_s [e.g. *Fejer and Kelley*, 1980]. Over the last 50 years, numerous studies involved coherent radar observations of E-region plasma waves to advance our understanding of their formation, occurrence trends, and control by the plasma convection. The current study contributes to this effort by employing the Super Dual Auroral Radar Network (SuperDARN) radars at the South Pole and Zhongshan Antarctic stations to investigate E-region plasma irregularities in the context of coincident and simultaneous observations of the F-region plasma convection derived from the entire SuperDARN array in the southern hemisphere. The below introduction first outlines the gaps that still exist in our understanding of E-region plasma irregularities in the context of previous studies and experimental approaches employed, which is followed by the formulation of the current approach, an overall aim, and specific objectives of the current study that address these gaps.

Arguably, the most important piece of knowledge about E-region irregularities is their control by the background plasma convection. The occurrence of echoes of likely FBI origin depends on the radar's orientation relative to the convection velocity $\mathbf{V}_E = \mathbf{E} \times \mathbf{B}/B^2$ and, in the auroral region, it generally increases for the radars that are oriented more parallel to the magnetic L shell [*Makarevich*, 2008]. The line-of-sight (l-o-s) phase velocity of the FBI irregularities depends on the convection speed V_E and the angle between the wave vector and the plasma flow, called the flow angle θ [*Nielsen and Schlegel*, 1983]. At small flow angles, the phase velocity of FBI echoes is usually less than $V_E \cos\theta$ and is saturated near C_s [*Nielsen and Schlegel*, 1983, 1985; *Makarevich et al.*, 2007]. However, some studies have demonstrated the unusual noncosine behaviour with the flow angle [*Nielsen et al.*, 2002] or even a cosine dependence $C_s \cos\theta$ [*Bahcivan et al.*, 2005].

The diurnal variation of the E-region radar aurora has been traditionally discussed in context of the eastward and westward electrojets. Radar echoes from the eastward electrojet were reported to have significantly greater mean Doppler velocity [*Haldoupis and Sofko*, 1976] and power [*Moorcroft and Ruohoniemi*, 1987] than echoes from the westward electrojet. *Haldoupis et al.* [1984] also reported that the westward electrojet had more "atypical" spectra associated with strong anisotropy in the electrojet current, while *Moorcroft and Tsunoda* [1978] noticed the presence of double-peak spectra in the eastward electrojet. These differences were attributed to the differences between the two electrojets [e.g. *Haldoupis et al.*, 1984], such as the height of the current center and the electrojet control by the conductance and electric field [*Kamide and Brekke*, 1977]. A statistical study of the distant C_s echoes observed by a HF radar showed noticeable differences between occurrences of echoes with velocity of different polarities and a prominent seasonal variation [*Lacroix and Moorcroft*, 2001]. Few previous studies have analyzed, however, the coincident and simultaneous data on the convection electric field, the factor that largely controls the E-region irregularity occurrence and characteristics as described above, and the asymmetry between the characteristics of echoes from different magnetic local time (MLT) sectors has not been investigated in context of the asymmetry in the convection itself.

Despite extensive statistical studies of the high-latitude convection pattern [*Ruohoniemi and Greenwald*, 1995, 2005; *Haaland et al.*, 2007; *Pettigrew et al.*, 2010], the asymmetry of the convection pattern and its IMF control have been only partially investigated [*Hepner and Maynard*, 1987]. *Ruohoniemi and Greenwald* [1996] have concluded that the dusk cell is usually larger in terms of its spatial extent and potential variation, but no quantitative measures of the asymmetry have been developed and neither asymmetry variation with latitude nor dependence on IMF have been analyzed. The convection asymmetry is a critical factor in the E-region irregularity observations, since asymmetric convection should cause the predominance of the FBI echoes of a particular velocity polarity and hence asymmetry in the E-region velocity distribution. Moreover, previous studies have shown that plasma convection exhibits a strong variation with season [*Ruohoniemi and Greenwald*, 1995, 2005; *Pettigrew et al.*, 2010], which should be reflected in the strong seasonal variation of the polarity of FBI echoes. This hypothesis is a subject of the current study.

Extensive data on both the E-region irregularities and the plasma convection at high latitudes are provided by the SuperDARN. The location of radars is dictated by the need to maximize the coverage of the high-latitude F-region. Most radars are located therefore at

the magnetic latitudes (MLATs) of 60°–65°, with predominantly poleward look directions. For this reason, their short-range fields-of-view (FoVs), where radars probe the E-region, do not typically have high-quality coincident F-region measurements. Recent deployment of the SuperDARN South Pole radar that samples locations deep within the typical convection pattern and at small flow angles has enabled further studies of the FBI echoes and their control by the convection component. Using this radar, *Makarevich et al.* [2015] demonstrated that during one month of February 2013, the occurrence of the FBI echoes with negative velocities was greater than that of the positive FBI echoes, and that this occurrence was strongly controlled by the convection component. Following the same idea, one expects that a radar with the E-region FoV at the same MLAT, but with an opposite orientation, would observe similar numbers of the FBI echoes but with predominantly positive velocities. In the current study, it is demonstrated that this expectation is only partially met and that the convection control is not the only factor that must be considered.

In the current study, a pair of SuperDARN radars is employed that probe the E-region along similar magnetic parallel from the westward and eastward directions and are located deep within the convection pattern, which enables an accurate, coincident, and simultaneous observation of the convection component above the E-region FoVs. The aim of the present study is to investigate to what extent the asymmetry in the occurrence of the E-region FBI echoes with different velocity polarities is caused by the asymmetry in the convection pattern. The specific objectives are to (1) investigate the asymmetry of the E-region velocity distribution and identify responsible plasma instabilities, (2) develop quantitative measures of the asymmetry in the plasma convection and analyze its variation with MLAT and IMF, and (3) evaluate the extent of the control of the asymmetry in the E-region velocity by the asymmetry in the plasma convection.

5.3 Experimental Setup

In this study we utilized the data collected by 10 SuperDARN radars in the southern hemisphere. These radars are referred to by their standard 3-letter codes: South Pole Station (SPS), McMurdo (MCM), Halley (HAL), Dome C East (DCE), Sanae (SAN), Zhongshan (ZHO), Syowa East (SYE), Kerguelen (KER), TIGER Unwin (UNW), and TIGER Bruny Island (TIG). All SuperDARN radars are similar technically and operationally [*Greenwald et al.*, 1995; *Chisham et al.*, 2007] and each radar measures Doppler velocity, power, and spectral width of ionospheric echoes obtained from the autocorrelation function using typically a seven- or eight-pulse sequence [*Ribeiro et al.*, 2013]. Each radar has 16 azimuthal beam directions separated by 3.24° (in case of radar transmission frequency of 12.5 MHz) that form a ∼52° footprint or FoV. The radar samples 75–100 range gates with 45-km resolution, starting at 180 km from the radar. One full scan through 16 beams takes 1 min. The data were not restricted in frequency for this study, ranging between 10 and 13 MHz. The typical frequencies were ∼ 12.5 MHz for SPS and ∼ 10.3 MHz for ZHO. All SuperDARN radars measure F-region velocity of the plasma convection at the range gates 765–3555 km. The Doppler velocity data from those range gates are combined in a standard SuperDARN algorithm to produce electrostatic potential and convection patterns using the map potential technique [*Ruohoniemi and Baker*, 1998]. The convection velocity $\mathbf{V}_E$ can be estimated from the convection pattern solution anywhere inside the zero potential boundary and is more accurate in the locations with high occurrence of the F-region echoes.

Figure 5.1 shows an example of the plasma convection pattern obtained using the map potential technique for a 10-min interval starting at 19:50 Universal Time (UT) on February 13, 2013. Color contours indicate the magnitude and sign of the potential, with the dashed (solid) lines representing positive (negative) equipotential contours. The boundary of the potential map is at 60°S based on altitude-adjusted corrected geomagnetic (AACGM) coordinate system with 2010 coefficients [*Shepherd*, 2014], with the top of the figure corresponding to magnetic noon and bottom to magnetic midnight.

The nominal range boundary between the E- and F-regions is different for different radars [*Makarevich*, 2010]. The present study focuses on observations of the E-region velocities with the SPS and ZHO radars that have their E-region FoVs deep within the convection pattern. These short-range FoVs are shown by small fan-shaped areas for SPS (blue) and ZHO (yellow). For SPS, the range boundary was found to be at 765 km, while for ZHO it is 405 km, based on examination of the range-time-intensity plots for SPS and ZHO.

This can be seen in the different sizes of the E-region FoVs of SPS and ZHO in Figure 5.1. The boundary was selected so that the bulk of the F-region backscatter is excluded, while the bulk of the E-region backscatter is retained. The major reason why the boundary is different for SPS and ZHO is high sensitivity of aspect angle conditions in the transitional region between the E- and F-regions to small changes in MLAT, radar orientation, and plasma density conditions.

Figure 5.1 also illustrates how SPS (blue) and ZHO (yellow) sample the E-region at different MLT sectors. SPS and ZHO appear to be located far away from each other based on the their geographic latitudes (89.99°S and 69.38°S, respectively). The difference in MLAT is, however, only 0.6°, with both radars sampling essentially the same MLAT. SPS and ZHO also have opposite orientations, which allows them to probe the E-region along the same magnetic L shell but from opposite directions.

SPS was deployed in January 2013 and ZHO started its operation in January 2010. The present study considers 11 full months of data collected from February to December 2013. Both ZHO and SPS were operating continuously during this 11-month period, with the exception of June for ZHO that had some data gaps. Again, the SPS and ZHO radar frequency was not restricted, ranging between 10 and 13 MHz. Ground scatter was excluded using the standard SuperDARN criteria of low velocity and low spectral width ($|(|V| - \triangle V)| < 30$ m/s, $|(W - \triangle W)| < 35$ m/s) and further cleaned, by excluding isolated interference and other spurious echoes with low signal-to-noise ratio (SNR) $P < 3$ dB, large spectral width $W > 500$ m/s, and very large Doppler velocity $V > 2000$ m/s. This approach was adapted from the previous SPS study by *Makarevich et al.* [2015].

In addition, IMF measurements, taken from the high-resolution OMNI database were used in this study in Section 5.6. All OMNI data are time-shifted from the spacecraft location to Earth's bow shock nose. The same IMF data were also used in the map potential technique [*Ruohoniemi and Baker*, 1998].

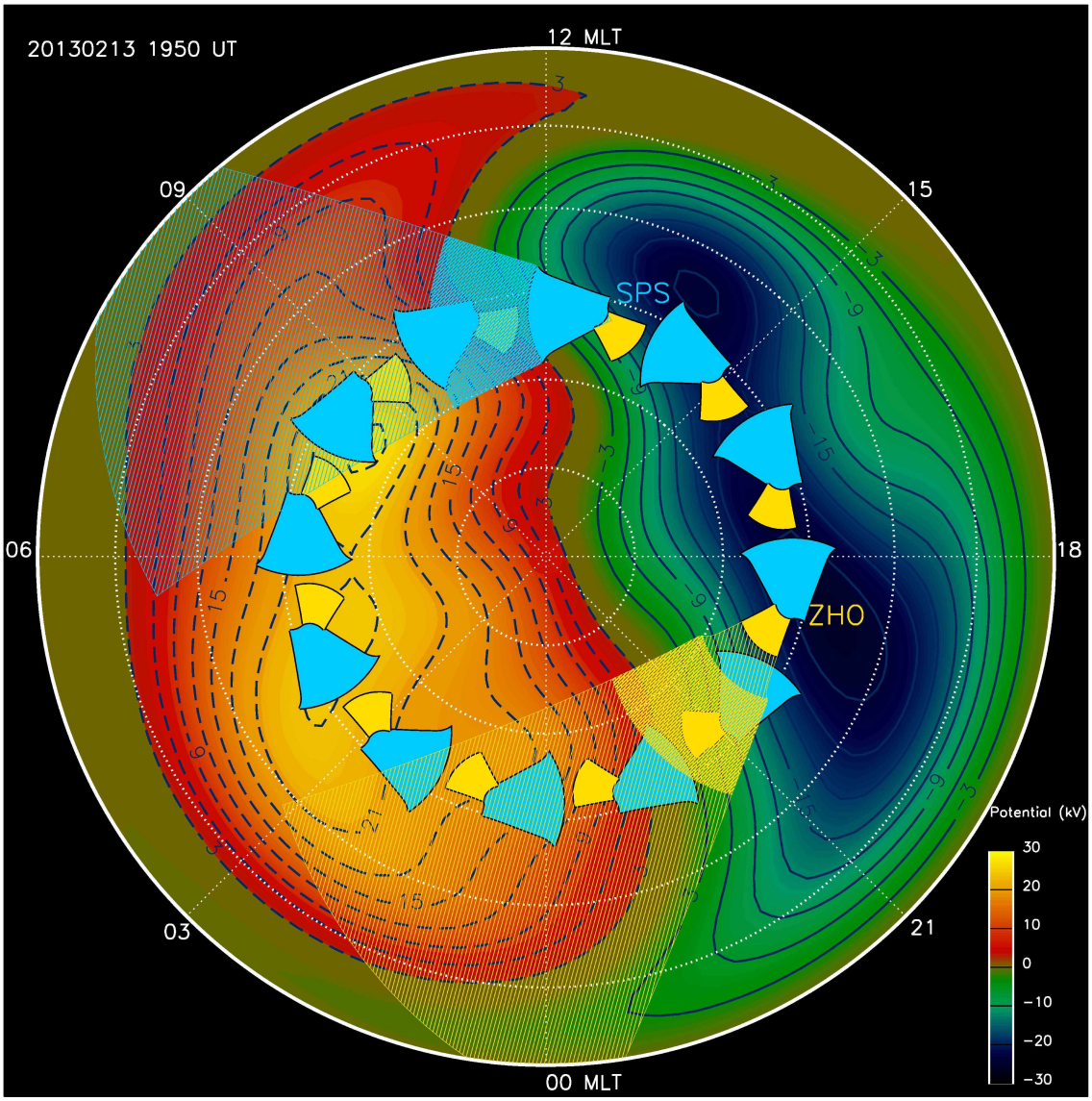

Figure 5.1. Experimental setup showing two Super Dual Auroral Radar Network (SuperDARN) radars at the South Pole (SPS) and Zhongshan (ZHO) stations that sample different magnetic local time (MLT) sectors in the short ranges as represented by 12 small fan-shaped areas filled with the solid blue and yellow color, respectively. Long-range FoV of SPS and ZHO for 2 MLT positions are shown as areas filled with lines. The F-region plasma convection on February 13, 2013, 19:50 UT from the SuperDARN map potential technique is shown in color. The lowest magnetic latitude (MLAT) is 60°S.

5.4 E-Region and Convection Component Velocity Distributions

The E-region velocity and convection component distributions are analyzed first using similar approach as that in *Makarevich et al.* [2015], but for the entire 11-months dataset and for both SPS and ZHO. Figure 5.2 shows the point occurrence of (a) E-region velocities, (b) convection component deduced from the map potential technique and projected to the central beam of the E-region FoV, and (c) F-region l-o-s velocities for SPS for February 2013. Figures 5.2d–5.2f show the same analysis for ZHO. The point occurrence for the E- and F-regions is shown binned in MLT using 10-min bins and in velocity using 25-m/s bins. The velocity distribution, normalized to the peak value in the bottom-right corner, is shown as the thick white line. The UT–MLT conversion is performed using the radar location for E-region velocity panels, center of the E-region FoV in case of the convection component panels, and separately for each range in case of l-o-s F-region panels. The peak value is more than 2 times higher for SPS than for ZHO due to the different E/F-region boundaries described in Section 5.3. The dip near the peak of the velocity distribution is due to the eliminated ground scatter.

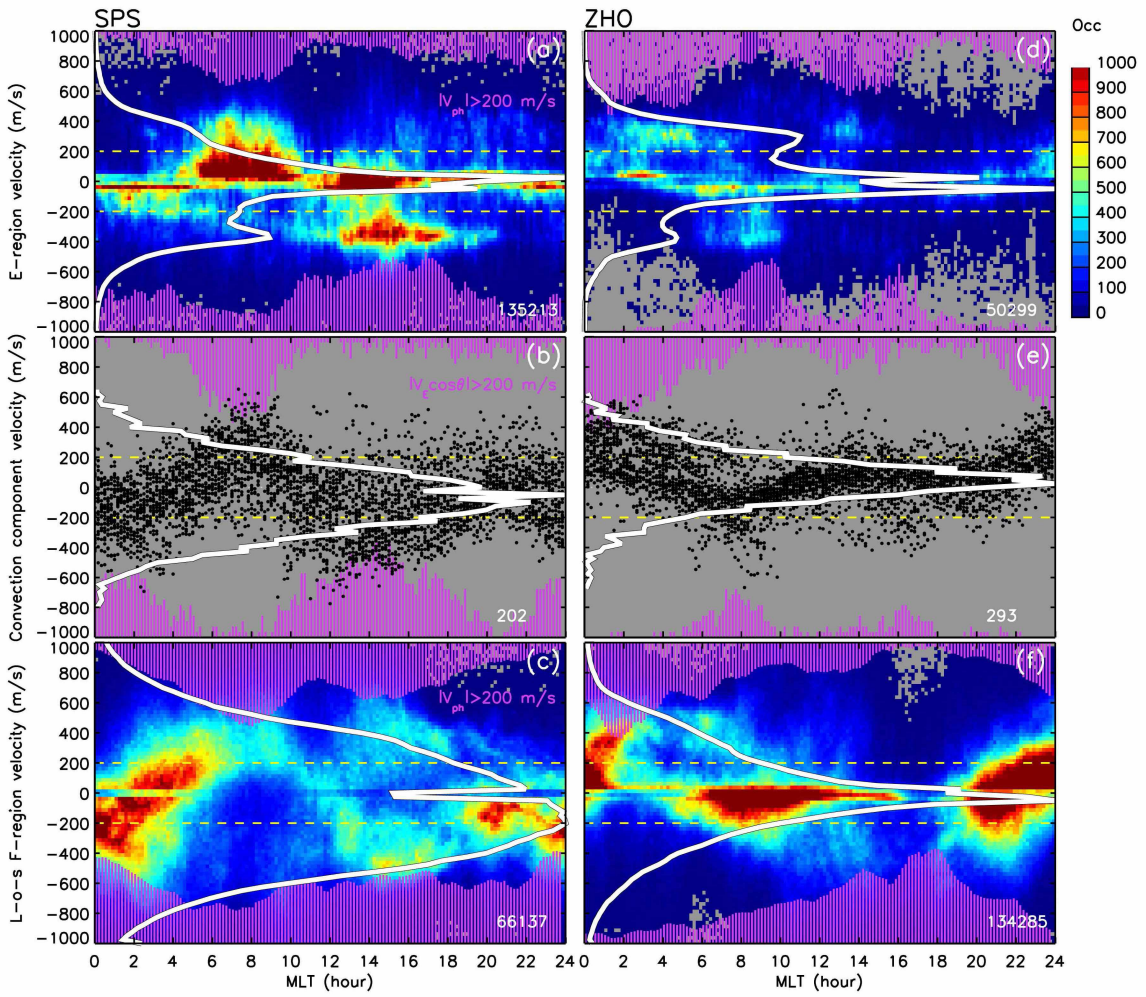

Figure 5.2. SPS and ZHO observations during February 2013. (a) Short-range SPS echoes binned in MLT and velocity with point occurrence shown by the color. (b) Convection velocity component in the center of the E-region FoV of SPS. (c) Same as (a) but for long-range F-region line-of-sight velocities. The thick white lines in all panels show the velocity distribution normalized by the maximum number of echoes shown in the bottom-right corner. The pink histograms show the occurrence of positive and negative high-velocity echo populations as a percentage of the total echo number for each MLT bin. The dashed lines indicate the threshold velocity of 200 m/s used for this analysis. Figures 5.2d–5.2e show same information but for ZHO.

The pink histograms in Figure 5.2 show the fractional occurrence of the positive and negative high-velocity echoes at 10-min bins. The threshold velocity value is chosen to be 200 m/s. The percent contribution of high-negative-velocity (away from the radar) echoes is presented as the bottom histogram. The height of each pink bar from the bottom indicates the fractional occurrence, where the vertical extent of each panel itself represents 100%.

The percent contribution of high-positive-velocity (towards the radar) echoes is presented in the same manner, but the entire histogram is vertically flipped and occurrence increases from the top down. In this presentation, the vertical spacing between the bars represent a percent contribution of low-velocity echoes.

The velocity threshold of 200 m/s was chosen for this analysis in order to include all E-region echoes that form a population of high-velocity echoes. Thus Figure 5.2a shows a cluster of high-negative-velocity echoes centered at 16 MLT that is clearly separated from echoes with velocities near zero. The overall distribution of echoes shown by the white line in Figure 5.2a shows a clear minimum near -200 m/s. The same features are observed for ZHO only here the overall distribution has two minima near ± 200 m/s. The same velocity value of 200 m/s is chosen as a threshold for the convection component analysis. This value differs from the value of 350 m/s used by *Makarevich et al.* [2015]. In the current study, however, a direct comparison of the fractional occurrence of high-velocity echoes of E-region velocity distribution and the distribution of convection component will be performed, which ideally requires the same threshold boundary. The possible physical reasons why this threshold may be lower than the nominal C_s value of 350 m/s for both E-region and convection velocities include density gradients changing the FBI threshold, different altitudes of E-region echoes, and aspect angle attenuation of irregularity velocity. These reasons are further discussed in Section 5.7.3. In Section 5.7.2 we also present a similar analysis, but for the nominal C_s value of 350 m/s.

Figure 5.2a shows that the occurrence of the low-velocity E-region echoes ($|V| < 200$ m/s) is high and more uniform in MLT than that of the high-velocity echoes ($|V| \geq 200$ m/s). That is, the vertical distance between the two pink histograms is larger than the values shown by either histogram and it does not appear to change much with MLT. The high-velocity echoes tend to cluster around particular MLT sectors, for instance, a well-defined cluster of high-negative-velocity echoes for SPS is seen near 16 MLT, which is reflected in the bump-on-tail seen in the white line near -350 m/s when all MLTs are combined. This cluster has been previously attributed to FBI [*Makarevich et al.*, 2015]. At positive velocities, no clustering is seen and instead the distribution has an inflection point near $+350$ m/s due to some high positive velocities near 08 MLT. The height of the inflection point is much lower than that of the bump-on-tail for SPS.

In comparison with the overall distribution of the E-region echoes, the distribution of the convection component shown in Figure 5.2b appears to be much more symmetric and

almost Gaussian, i.e. no bumps-on-tail or inflection points. It is also not as smooth but this is simply because of the much lower numbers of measurements (∼200 vs ∼50,000 or ∼135,000) since only convection component at one location within the FoV is considered rather than all echoes for all cells. One can see however that there is a small bias towards negative velocities for SPS.

Figure 5.2c shows the same analysis as Figure 5.2a, but for the line-of-sight velocities of echoes from long-range gates 765–1350 km that refer to the F-region. This portion of the FoV was shown in Figure 5.1 as areas that were more densely filled with lines. All long-range gates 765–3555 km cover a significant portion of the entire MLT range, as shown in Figure 5.1 by the large fan-shaped areas filled with lines. In order to ensure reasonable accuracy of the UT–MLT conversion, the top range was restricted to 1350 km and the UT–MLT conversion was performed for each range separately. Similar to the distribution of the convection component, the distribution of the F-region line-of-sight velocities is more symmetric than the E-region distribution. This feature is consistent with that seen in the convection components in Figures 5.2b and 5.2e. The line-of-sight F-region velocity distribution for SPS (white line in Figure 5.2c) has a negative bias, which is also consistent with that seen in Figure 5.2b. The ZHO distribution in Figure 5.2f has a small negative bias (the white line crosses a line of –200 m/s at a somewhat higher value that the line at +200 m/s), but the difference is relatively small. Overall, both analyses involving F-region velocity show distributions that are more symmetric than their E-region counterparts. Importantly, F-region velocity distributions show no evidence of a bump-on-tail feature near ±350 m/s. Since only the convection component (Figures 5.2b and 5.2e) represents truly coincident measurements, the focus of the following analyses is on this estimate.

ZHO observes two clusters of high-positive-velocity E-region echoes around 02 and 12 MLT, and one cluster of high-negative-velocity echoes near 08 MLT. Interestingly, ZHO does not have a population of high-velocity echoes merged with low-velocity echoes similar to the one that SPS has around 08 MLT. This feature is reflected in the fact that there is no inflection point in the velocity distribution, and bump-on-tail is present on both sides of the distribution. In contrast with SPS, ZHO has a higher number of high-positive-velocity echoes, which is seen in the difference between the heights of the bump-on-tail features.

FBI is operational when the plasma component exceeds a certain threshold near the ion-acoustic speed C_s, see Section 5.7.2. Comparing the tails of the convection component

distributions in Figures 5.2b and 5.2e (intersections of the white and yellow dashed lines), SPS (ZHO) has higher occurrence of the negative (positive) convection component. The same feature can be seen in the l-o-s F-region velocities in Figures 5.2c and 5.2f. This feature is consistent with observation of higher occurrence of the negative (positive) FBI echoes for SPS (ZHO) in Figures 5.2a and 5.2d. This relation is further investigated below.

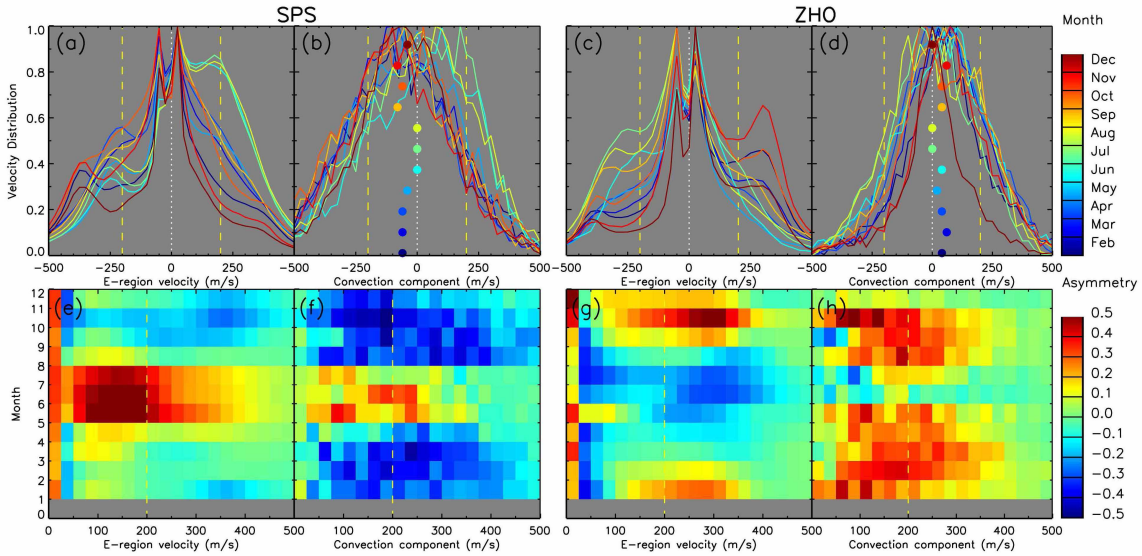

Figure 5.3. E- and F-region velocity distributions and their asymmetry for different months in 2013. Panel (a) shows the E-region velocity distributions for SPS. Panel (b) shows the F-region convection component distributions. Each circle in panel (b) shows a shift of the distribution. The color of the lines and circles indicates the month. Panels (c) and (d) show the same information but for ZHO. Panels (e)–(h) show the differences between the positive and negative branches of velocity distributions in panels (a)–(d). Plot cells are color-coded in fractional differences according to the color bar to the right. The yellow dashed lines in all panels show the threshold velocity value of ±200 m/s.

The distributions of the E-region velocity and the convection component during one month of February 2013 were presented in Figure 5.2. The same distributions were obtained for all months in 2013 and the results are presented in Figure 5.3. Figures 5.3a and 5.3c show the E-region velocity distributions for SPS and ZHO, respectively, color coded in month. Figures 5.3b and 5.3d similarly show the convection component distributions. The horizontal position of the circles in Figures 5.3b and 5.3d show a shift of the monthly distribution of the convection component, with color again indicating the month. Yellow dashed lines show velocity values of ±200 m/s.

From Figure 5.3a, the bump-on-tail feature is seen at negative velocities for SPS in most

months. The peak is near −350 m/s but it changes its position with season. At positive velocities, the bump-on-tail is seen only for 3 months in austral winter (green lines), with the inflection point seen in most other months. The situation is somewhat different for ZHO, Figure 5.3c, and it is not a simple reflection of that for SPS. That is, a bump-on-tail is seen most often at negative velocities for ZHO, despite its opposite orientation to SPS.

The convection component distributions shown in Figures 5.3b and 5.3d reveal a different picture. Besides the noise due to the low number of convection estimates, these distributions show no bump-on-tail or inflection points. Some asymmetry in the convection component is seen, but it is due to a small shift of the entire distribution as represented by the large circles. This shift shows some seasonal dependence; it is negative during the austral summer for SPS and positive for some summer months for ZHO. Comparing the shift behavior with season between SPS and ZHO, large color circles in Figure 5.3b appear to be a simple reflection of those in Figure 5.3d, as expected for opposite orientations of SPS and ZHO. As noted before, however, this was not the case for the E-region velocity distributions, which were significantly different between SPS and ZHO, even if the latter was reversed in velocity polarity.

This feature is further analyzed by finding the asymmetry or the difference between the positive and negative branches of the distributions for both E-region and convection velocities. That is, for each velocity magnitude value V, the asymmetry is defined as $N(V, V+dV) - N(-V-dV, -V)$, where $N(V_1, V_2)$ is the number of velocity measurements between V_1 and V_2 and dV is the bin size (25 m/s in our case).

Figures 5.3e–h show these differences for all velocity bins and months. The yellow dashed line shows the value of 200 m/s. The asymmetry at velocities < 100 m/s is meaningless due to the elimination of the ground scatter. In this presentation it is easier to see that the seasonal variation is very pronounced. The E-region velocity asymmetry is mostly positive (negative) in the austral winter (summer) season for SPS, and vice versa for ZHO, Figures 5.3e and 5.3g. This feature is also seen in the convection component, Figures 5.3f and 5.3h. Thus, the plot cells are green-to-red in the May–July period in both Figures 5.3e and 5.3f. A similar, although less pronounced, feature is seen for ZHO, where the plot cells are blue and green-to-yellow in June–July in Figures 5.3g and 5.3h. This indicates not only that asymmetries in the E-region velocity and convection component distributions are consistent, but also that their seasonal trends are similar.

The E-region asymmetry also changes between different velocity bins. Thus SPS ob-

serves predominantly positive asymmetry at 100–200 m/s (red to green colors in Figure 5.3e), particularly during winter. Similarly, a negative asymmetry is seen near the nominal C_s (blue colors), except for winter. These features are related to the bump-on-tail and inflection point features in the overall velocity distributions. For example, negative asymmetry near C_s for SPS is due to the bump-on-tail at negative velocities being higher than the inflection point at positive velocities. In contrast to SPS, asymmetry for ZHO does not have distinct trends at different velocity bins, i.e. the blue and red peaks of the asymmetry are vertically aligned, Figure 5.3g. The velocity value where asymmetry peaks is near 300 m/s; at this value the seasonal trend is most clear and this is also the value where most bump-on-tail features are seen in Figure 5.3c. The patterns are similar between the E-region and convection component asymmetries, Figures 5.3g and 5.3h, although for ZHO the similarity is not as strong as for SPS.

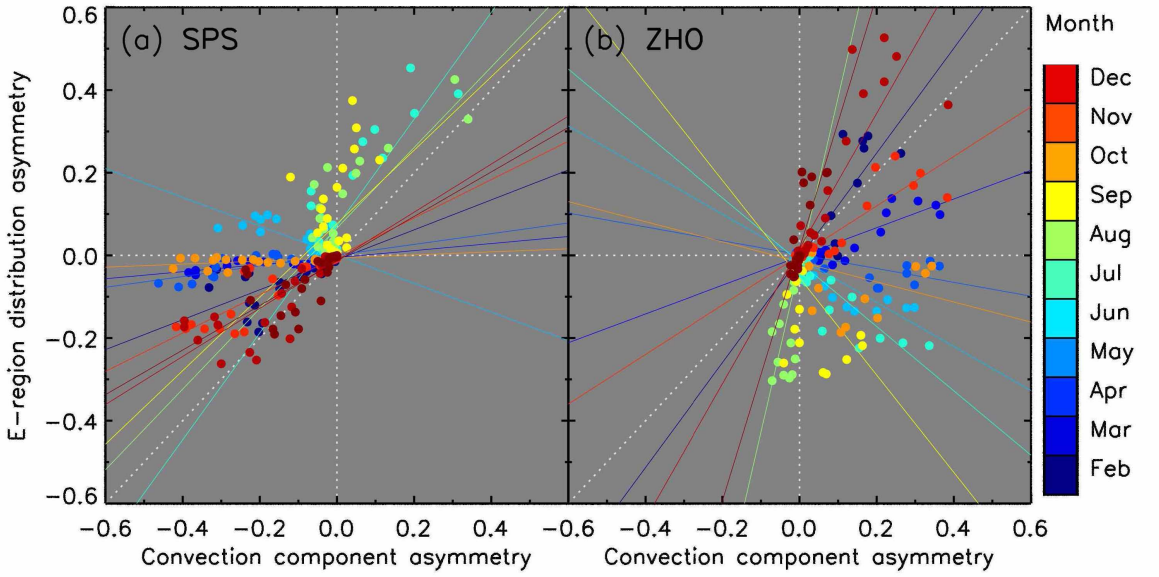

Figure 5.4. Scatter plots of the E-region velocity asymmetry versus the convection component asymmetry for (a) SPS and (b) ZHO. Fractional differences from the second row of Figure 5.3 are shown, with color indicating the month. Linear least-squares fits are also shown for each month.

This similarity between the E-region velocity and convection component asymmetries prompts the next analysis in which the two quantities are compared directly. Figure 5.4 presents scatter plots of the E-region velocity asymmetry versus convection component asymmetry, with both expressed as fractional differences from Figures 5.3e–5.3h. The velocities were restricted to the high-velocity range $|V| \geq 200$ m/s. From Figure 5.4, there

is no particularly strong correlation between the two quantities for the entire dataset that would indicate a strong control of the E-region asymmetry by the asymmetry in the convection component. However, positive correlation is present in some months for both radars. One can also seen that most of the points are located on the left of the ideal coincidence line for SPS and on the right for ZHO, which is again consistent with their opposite orientation. The slopes of linear trends are all positive for SPS, with an exception of one month of June, while for ZHO 6 are positive and 5 are negative. Overall, this analysis shows some control of the E-region velocity asymmetry by that of the convection component.

5.5 Asymmetry Analysis Using High-Velocity Echo Occurrence

In the previous analysis, the MLT dependence was eliminated from the very beginning and the focus was on the seasonal variation of the velocity distributions. In this section, the MLT variation of the occurrence of high-velocity echoes and their control by the plasma convection are investigated. The pink histograms in Figure 5.2 showed the diurnal variation of the fractional occurrence of high-velocity echoes for the E-region velocities and for the convection components. Comparing Figures 5.2a and 5.2b for SPS as well as Figures 5.2d and 5.2e for ZHO, the peaks of the fractional occurrence are in the same MLT sectors. For example, the high-positive-velocity echoes peaked near 08 MLT in Figure 5.2a, which was the same sector where the convection component exceeded 200 m/s most often in Figure 5.2b. To perform a detailed comparison between these fractional occurrences, the MLT–month patterns were obtained and are presented in Figure 5.5.

The first row of Figure 5.5 shows the fractional occurrence of the high-velocity echoes in the E-region, where Figures 5.5a and 5.5c show the occurrence of the positive and negative velocities, respectively, for SPS. Similarly, Figures 5.5e and 5.5g show the same information for ZHO. The second row of Figure 5.5 shows the fractional occurrence of the high-velocity convection component. Due to the lower number of estimates for the convection component, the MLT bin size was set to be 20 min, i.e. twice as large as that for the E-region velocity occurrence.

Figure 5.5 shows that the MLT–month patterns are similar for the two quantities under consideration for each radar, e.g. compare Figures 5.5c and 5.5d. The linear Pearson correlation coefficients between values shown in panels (a) and (b), (c) and (d), (e) and (f), (g) and (h) are 0.72, 0.79, 0.48, 0.68. Comparing the patterns between the two radars, one finds that they are essentially opposite, i.e. Figure 5.5c are more similar to Figure 5.5e. This can be easily explained by the opposite orientation of the radars, Figure 5.1.

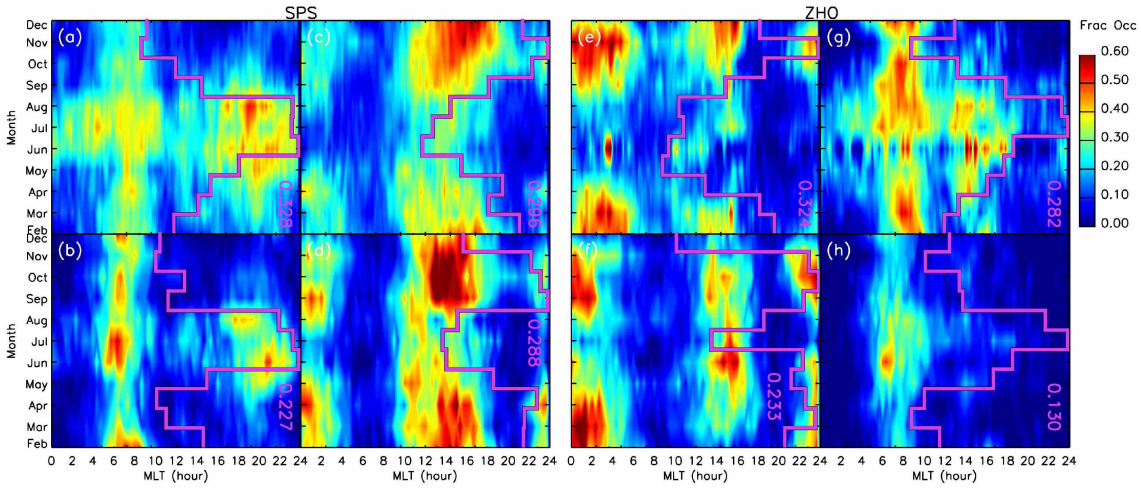

Figure 5.5. MLT–month patterns of the fractional occurence of positive and negative E-region echoes and the convection component both exceeding 200 m/s. Panels (a) and (c) respectively show fractional occurrences of positive and negative E-region velocities for SPS. Panels (b) and (d) respectively show fractional occurrence of positive and negative convection components for SPS. Panels (e)–(h) show the same information but for ZHO. The pink line in all panels shows the normalized fractional occurrence averaged in MLT. The maximum that was used for normalization is shown on the right of each panel.

The diurnal variation of the fractional occurrences can be explained by increasing plasma density around magnetic noon, due to increased photoionization, and magnetic midnight, due to the increased impact ionization. These trends can be more visible if one combines the fractional occurrence of positive and negative velocities into one plot (e.g. Figure 5.5a and 5.5b). In order to investigate the seasonal variations of the fractional occurrences, these were averaged in MLT for all panels, which is shown as a pink histogram. In this presentation, the histograms are normalized to a maximum, with the normalization coefficient shown in the left of each panel. Again, the seasonal trends are similar between the two quantities, e.g. during the austral winter the high-positive-velocity echoes are predominant, and so are intervals with high positive convection components.

One way to analyze the predominant polarity of the high-velocity echoes is to look at the differences between fractional occurrences of high-positive-velocity and high-negative velocity echoes. That is, in the next analysis we subtract the values represented by the pink lines in each pair of panels in Figure 5.5, e.g. the values represented by the pink line in Figure 5.5c are subtracted from those in Figure 5.5a. In this analysis, the proper fractional occurrences were used, i.e. with no normalization to the maximum.

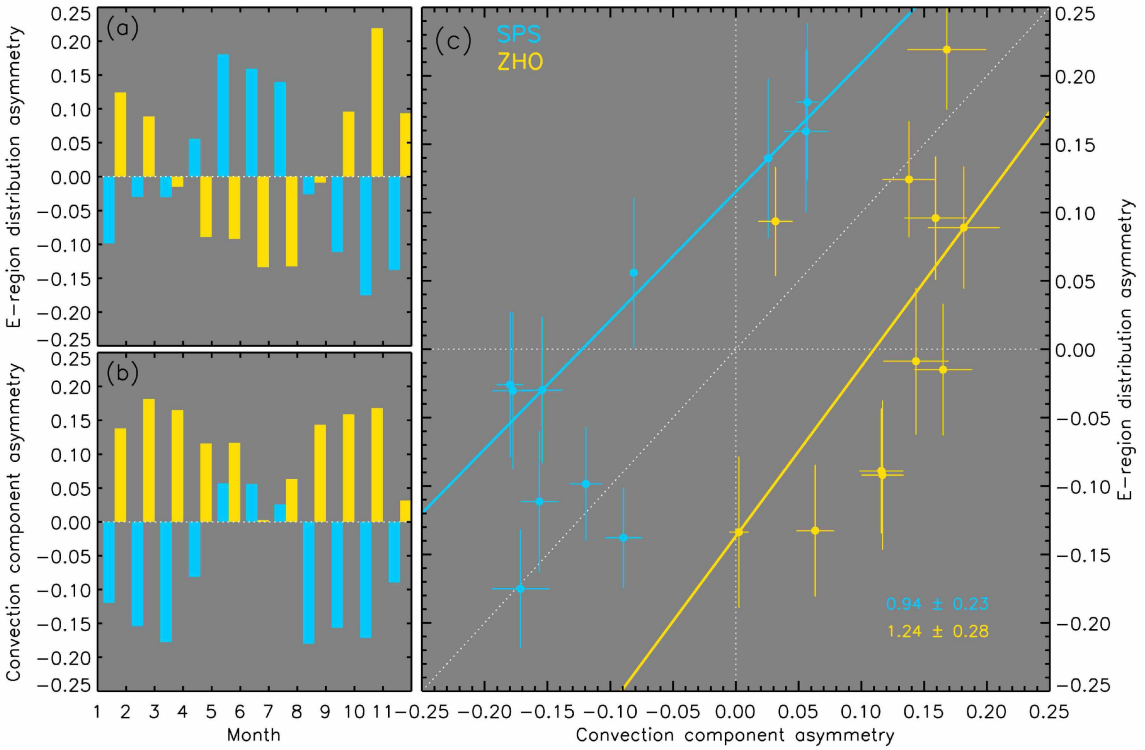

Figure 5.6. Seasonal variations of asymmetries in the occurrence of the (a) high-velocity echoes and (b) high-velocity convection components. The data for SPS and ZHO are shown in blue and yellow, respectively. Panel (c) shows the two quantities plotted against each other. The linear trends show the least-absolute-deviation fits with slopes and their fitting errors shown in the right corner.

The first column of Figure 5.6 shows a seasonal variation of the asymmetry in the occurrence of the (a) high-velocity E-region echoes and (b) high-velocity convection component for SPS (blue) and ZHO (yellow). Figure 5.6c shows these two quantities plotted against each other for each month and for both radars. The error bars were estimated by lowering and rising the limit of the threshold velocity by 25 m/s before performing the same analysis, e.g. to lower the fractional occurrence the velocity boundary that defines the high-velocity E-region echoes was set to be 225 m/s instead of 200 m/s. The least-absolute-deviation fit was used to produce the linear fit for each radar. The slopes of the lines are 0.94±0.23 and 1.24±0.28 for SPS and ZHO, respectively. Seasonal dependencies of these two quantities for SPS (blue bars) are similar in Figures 5.6a and 5.6b, with mostly negative (positive) values in austral summer (winter). For ZHO the seasonal trends are not as similar but they too show more negative/less positive asymmetries in winter. Comparing the data for two radars, one can also immediately see strong similarities when accounting for the opposite

directions. Thus seasonal dependencies in Figures 5.6a and 5.6b are approximately the reflections of each other. It is Figure 5.6c however, that shows most clearly both the agreement between the E- and F-region asymmetries and the similarity between the two radars. Thus both slopes are unity within the uncertainty, and if one reverses the polarity of the yellow points and of the linear trend, the data for the two radars would look very similar. Overall, this analysis indicates that the asymmetries in the high-velocity E-region echoes and high-velocity convection component exhibit strong seasonal dependence and that the E-region asymmetry is strongly controlled by the convection component asymmetry. At the same time, the bias in the convection component distribution also appears to be important, with SPS (ZHO) convection component being mostly negative (positive), which shifts the linear trend upward (downward).

5.6 Asymmetry of the Plasma Convection Pattern

In the previous two sections, the asymmetry in the convection component in the center of the E-region FoV has been shown to exhibit strong control over that of the E-region velocity distribution. In this previous analysis, the convection component asymmetry estimate was obtained by allowing each radar to sample the entire MLT range. Hence the convection component asymmetry must be due to the asymmetry of the convection pattern itself and this is what is investigated in this section.

The average zonal convection component for any given MLAT value can quantify the asymmetry in the convection pattern at that MLAT and these were calculated for all 10-min intervals in the period under investigation. The results of this analysis are shown in the first column of Figure 5.7, where each row shows monthly average zonal convection component versus UT and month for 5 selected MLAT values. Note that two different color bars are used for this plot; the westward (eastward) component of the convection velocity is shown in blue (red), with the maximum of 200 m/s (30 m/s).

The first feature that is seen in Figure 5.7 is a significant change in the pattern from the polar cap to the auroral region. The zonal convection is predominantly westward (blue colors), especially at the lower latitudes. In the polar cap, the zonal convection asymmetry has a distinct UT dependence, where zonal convection is predominantly eastward (red) at 06–16 UT and westward in other UT sectors, with no pronounced seasonal variation. Some seasonal variation is noticeable at MLATs of 75°S and 80°S, where during the austral winter the convection is more symmetric (white or red colors). Color circles in a panel that corresponds to MLAT of 75°S show the UT-averaged zonal convection, where the color of the circles indicate the month. The scale is determined by the circle furthest away from the dashed line (zero velocity) in November, whose shift position is 62 m/s. This presentation is very similar to that in Figures 5.3b and 5.3d, and both the shift values and their seasonal variations are very similar to those in Figure 5.3b. A MLAT of 75°S is the closest to the one that both SPS and ZHO sample, and this therefore confirms that the asymmetry or bias in the convection component is due to the bias in the convection pattern itself. Only in case when the color of the pattern is white the eastward and westward flows are balanced, which gives zero zonal flow on average. Note that, on average, the convection pattern is hardly ever eastward-biased. This feature will be further discussed in Section 5.7.

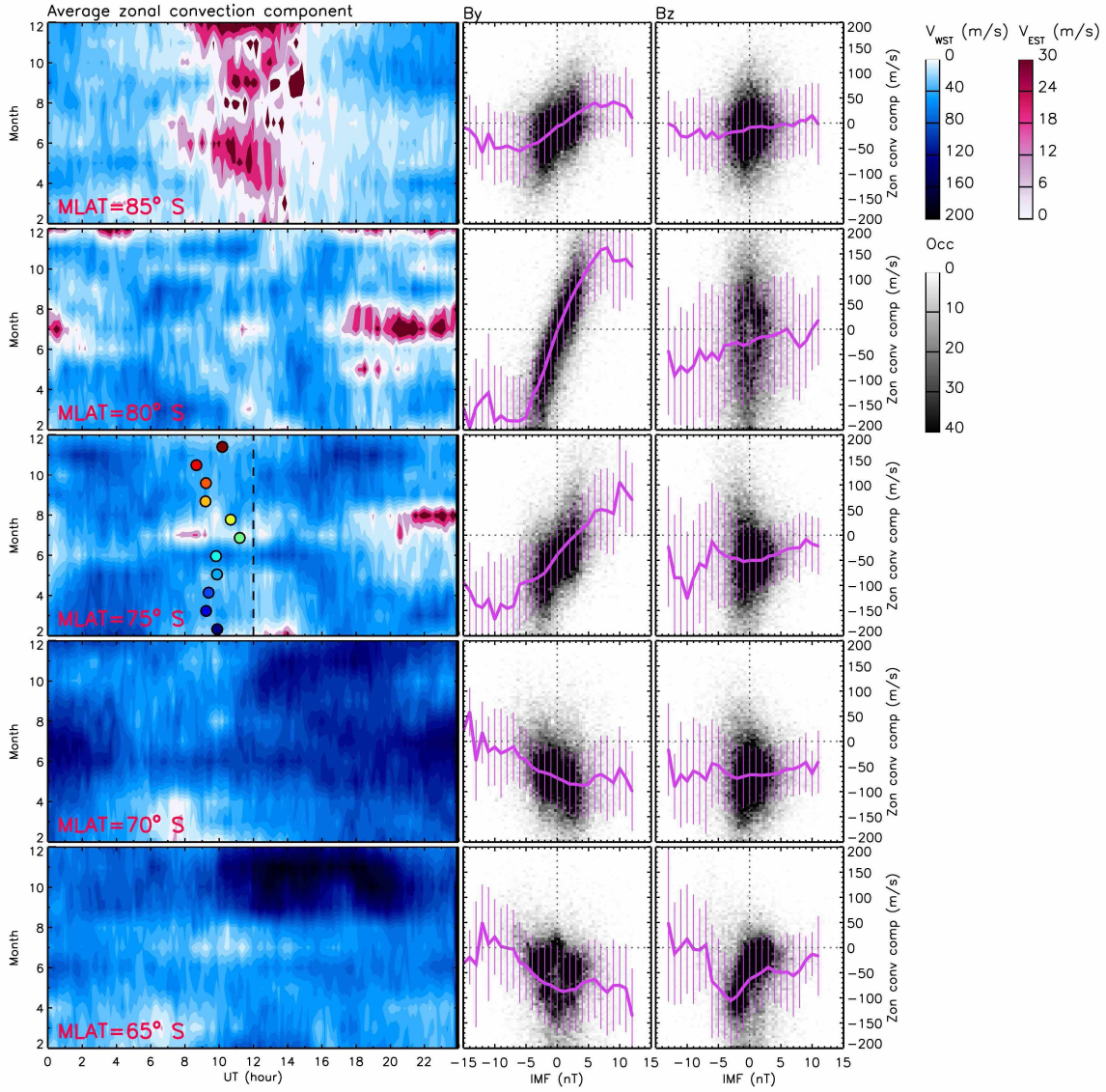

Figure 5.7. Average zonal convection component velocity and its IMF control at different latitudes. The first column shows the average zonal convection component binned in UT and month for 5 different magnetic latitudes. Color circles in the panel that corresponds to MLAT of 75°S show the zonal convection component averaged in UT in arbitrary scale. The colors of the circles indicate the month of the year, same as in Figures 5.3b and 5.3d. The second and third columns show a dependence of the average zonal convection component on IMF B_y and B_z, respectively, with gray scale representing the point occurrence. The pink line with the error bars is the binned trend.

The configuration and the intensity of the plasma convection pattern is strongly controlled by IMF. To investigate the effects of IMF on the asymmetry of the convection pattern, the average zonal convection component for each time frame is plotted versus (second

column) IMF B_y and (third column) B_z components in Figure 5.7. The point occurrence is shown in grey scale and the average trend with the standard deviation is shown in pink. On the vertical axis, the negative (positive) sign of the zonal convection component represents the westward (eastward) orientation. In the polar cap and auroral regions, the highly positive (negative) IMF B_y component makes the convection flow more eastward (westward) oriented. Interestingly, the trend is opposite at the lower latitudes. The B_z dependence is less obvious, but, at all latitudes, the convection is more symmetric for more positive B_z.

5.7 Discussion

This statistical study presented an investigation of the predominant velocity polarity of the E-region echoes using the SuperDARN South Pole and Zhongshan radars. Both radars are located close to each other in magnetic latitude and sample the E-region along the same magnetic L shell but in opposite directions. The uniqueness of this study is in the continuous, simultaneous, and coincident observations of the plasma irregularities in the E- and F-regions, that was enabled by the location of the radars deep within the convection pattern. Assuming that the dawn and dusk cells of the convection pattern are equal, the distribution of the convection component is expected to be symmetric, and so is the E-region velocity distribution, if it is largely controlled by the plasma convection. If convection pattern is somewhat asymmetric, then the two radars should observe E-region velocity distributions that have similar asymmetries (after accounting for opposite orientations). However, it was found that the E-region velocity distribution was asymmetric, in large part because of FBI echoes and that the two radars observed somewhat different asymmetries due to different occurrences of FBI echoes. Further, it was shown that the convection asymmetry strongly controls the asymmetry in the E-region, and a small shift of the convection component distribution causes a significant asymmetry in the E-region velocity distribution. Below it is argued that the E-region velocity distribution may be highly sensitive to the asymmetry in the F-region convection component and that it may be affected by factors other than plasma convection.

5.7.1 Asymmetry in the Convection Pattern and the Convection Component

Plasma convection exhibits a significant level of variability, even during the steady solar wind conditions [*Bristow et al.*, 2004], and is highly dependent on the IMF orientation and strength [*Heelis*, 1984; *Ruohoniemi and Greenwald*, 1995]. A new aspect of the current study is related to the analysis of the asymmetry convection pattern, Section 5.6. The fact that the dusk cell is sometimes larger than its dawn counterpart was reported in several previous studies [e.g. *Cowley et al.*, 1991; *Knipp et al.*, 1991; *Ruohoniemi and Greenwald*, 1996], however this asymmetry has not been analyzed quantitatively. In the current study, the asymmetry of the plasma convection pattern was quantified and analyzed in terms of the asymmetry in the average zonal convection component and its MLAT and IMF dependencies.

An important new result was that the convection is hardly ever symmetric, which is

reflected in the predominance of the westward flow of plasma. Further, this asymmetry changes significantly with magnetic latitude. The basic reason for why such an asymmetry would be observed is a difference between the dawn and dusk cells. In the extreme case, convection pattern would be one large cell and a radar would always observe a zonal component of a particular polarity. In less extreme cases, one cell is larger and a radar observes a zonal component of a particular polarity for a longer period of time. *Ruohoniemi and Greenwald* [1996] reported that the cells are more equal for a larger IMF B_y, however no noticeable B_z effects have been reported. In the current study, the IMF B_y component was demonstrated to affect the asymmetry of the convection pattern stronger than IMF B_z, particularly at the higher latitudes >75°S, Figure 5.7. An interesting reversal in the IMF B_y dependence was also noticed at the lower latitudes.

Seasonal variation of the convection pattern has been discussed in numerous previous studies [*Crooker and Rich*, 1993; *Rich and Hairston*, 1994; *Ruohoniemi and Greenwald*, 1995, 2005], usually in context of the IMF effects. A recent study by *Pettigrew et al.* [2010] about the interhemispheric asymmetry of the plasma convection has demonstrated that seasonal variation of the convection pattern is closely related to the seasonal change in the Earth's dipole tilt angle which changes the magnetic reconnection topology and the solar-produced conductivities. A related new result of the current study is that a seasonal variation of the asymmetry of the zonal convection component is evident only at the MLATs of 75°–80°S, where the predominantly westward component changes to more eastward during the austral winter.

Taking into account the asymmetry in the zonal convection, it is important to determine how it will be reflected in the velocity distribution of the convection component. It has been shown in Section 5.4 that a distribution of the convection component has a Gaussian shape, which is related to the fact that the convection has a closed-loop geometry. It has also been demonstrated in Section 5.4 that the monthly distribution of the convection component has a positive or negative bias, depending on the radar. This bias was shown to exhibit a particular seasonal variation, Figures 5.3 and 5.6. In case of the MLAT of 75°S, the sign of the bias depends on the orientation of the radar, while its magnitude depends on the season. From Figure 5.7, a particular seasonal trend of the bias would hold only for a particular MLAT. Ultimately, the asymmetry of the zonal convection component is predominantly westward and exhibits a strong IMF B_y dependence. The asymmetry of the zonal convection component is obviously reflected in the bias of the velocity distribution

of the convection component. In the next section, we discuss how this bias may affect the occurrence and characteristics of the E-region FBI echoes. The overall conclusion that can be drawn from this analysis is that the convection asymmetry is stronger than perhaps previously thought, changes with MLAT, and has a westward bias due to predominantly westward zonal component of the convection.

5.7.2 E-Region Velocity Aasymmetry Expected from Convection Bias

It has been demonstrated in Section 5.4 and discussed in Section 5.7.1 that the convection component distribution usually has a Gaussian form that is shifted from zero by 25–50 m/s depending on a season, with a sign determined mostly by the radar's orientation. In this section, the expected E-region velocity asymmetry is estimated based on the shift of the convection component distribution using a simple model that uses a Gaussian function.

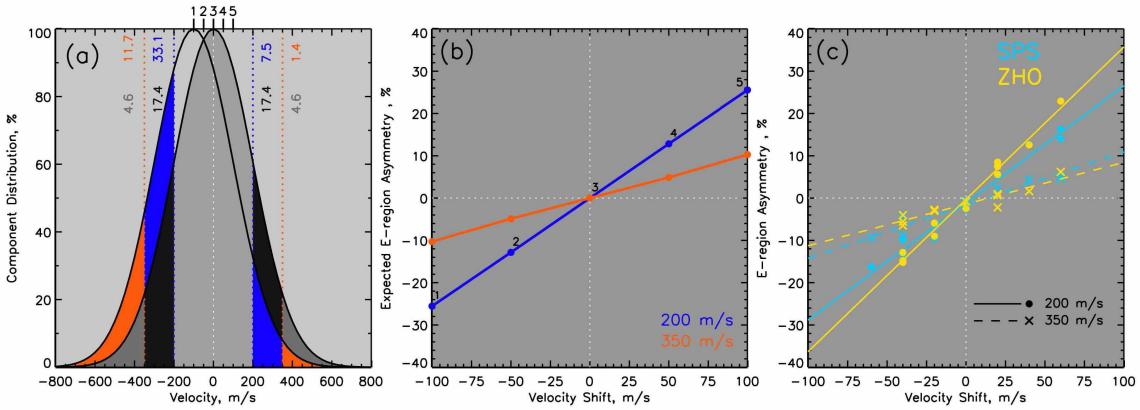

Figure 5.8. Expected E-region asymmetry caused by the shift of the symmetric distribution of the convection component. Panel (a) shows two Gaussian velocity distributions centered at zero and −100 m/s. Areas filled with black and gray show the unshifted distribution tails with two different threshold values of 200 and 350 m/s. Areas filled with blue and orange colors similarly show the tails of the shifted distribution. The percentages in the tails are given by the numbers at the top of the panel. Panel (b) shows the differences between the positive and negative tails for 2 different threshold values and 5 different shift positions. The color scheme that indicates the threshold value is the same as in panel (a). Panel (c) shows the differences between the positive and negative tails of E-region velocity distributions versus the shift of the convection component distribution for all 11 months for SPS (blue) and ZHO (yellow). Circles (crosses) refer to the threshold value of 200 m/s (350 m/s), with solid (dashed) line giving the linear fits.

Figure 5.8a shows two Gaussian distributions, where one that is filled with dark grey color is not shifted and another one is shifted by 100 m/s to the left. Three other shifts are

also considered, but not shown to keep the diagram readable. All 5 different shifts are shown at the top of the panel, where numbers 1–5 correspond to the shifts by −100, −50, 0, 50, 100 m/s, respectively. The dashed color lines indicate positive and negative velocity threshold values of 200 and 350 m/s used in this analysis. Grey-scale (color) numbers show the area in the tails expressed as percentage of the total area of the unshifted (shifted) distribution for two threshold values. The tails on positive and negative sides for the unshifted distribution are equal as seen in the grey-scale numbers. For example, for the threshold value of 200 m/s, the black areas of the positive and negative tails both contain 17.4% of the distribution. In contrast, the negative tails are greater for the shifted distribution, e.g. for the same threshold of 200 m/s, the blue areas contain 33.1% and 7.5%, respectively.

Figure 5.8b shows the percent differences between the positive and negative tails for two threshold values (indicated by the color, same as in Figure 5.8a) for 5 different shifts of the distribution. For instance, for the threshold of 200 m/s (blue) and a shift of −100 m/s, the difference is $7.5\% - 33.1\% = -25.6\%$ which corresponds to the leftmost and lowest point in Figure 5.8b. Note that at the position number 3 (no shift) the percent difference is 0, as expected. From Figure 5.8b, the asymmetry increases linearly with the shift of the distribution.

The idea for the next analysis comes from the expectation that convection velocities exceeding a certain threshold will produce FBI echoes that, in turn, will produce the *E*-region velocity asymmetry as explained below. The linear fluid theory of FBI predicts that the growth rate in the ion reference frame [*Rogister and D'Angelo*, 1970; *Sudan et al.*, 1973; *Fejer et al.*, 1975] is equal to

$$\gamma = \frac{\Psi}{\nu_i(1+\Psi)}\left(V_{ph}^2 - C_s^2\right), \tag{5.1}$$

where $V_{ph} = V_E \cos\theta/(1+\Psi)$ is the irregularity phase velocity, and

$$\Psi = \frac{\nu_i \nu_e}{\Omega_e \Omega_i}\left(1 + \sin^2\alpha \frac{\Omega_e^2}{\nu_e^2}\right) \tag{5.2}$$

is the anisotropy factor that depends on collision frequencies ν_i and ν_e, gyrofrequencies Ω_i and Ω_e, and the angle between perpendicular to the local magnetic field and the irregularity wave vector, known as the aspect angle α.

The FBI instability is operational when the growth rate $\gamma > 0$, which defines a threshold for the component of the convection velocity $V_E \cos\theta > C_s$, assuming that the aspect

angle is small and hence $\Psi \ll 1$. Thus, FBI irregularities are expected whenever the convection component exceeds the ion-acoustic speed C_s. In Figure 5.8a, the tails of the distribution with high velocity component essentially represented the percent occurrence when the threshold condition for the E-region irregularity production is satisfied. Therefore, the percent difference, or asymmetry, between the positive and negative tails can serve as an estimate for the percent difference between the number occurrence of the FBI waves with positive and negative phase velocities. For this analysis, we used two threshold values of 350 and 200 m/s. The first value is the nominal FBI threshold, while the second value of 200 m/s was chosen based on our observations, as was previously discussed in Section 5.4, and since the FBI threshold can be lower, as further discussed in Section 5.7.3.

In order to compare the expected and observed trends, the measured asymmetries in the E- and F-region velocities were calculated in the same way (as a difference between the positive and negative tails) for 11 monthly datasets; these distributions were previously shown in Figures 5.3a–5.3d. Figure 5.8c presents the E-region asymmetry versus the convection component velocity shift for SPS (blue) and ZHO (yellow). Circles represent the measured E-region asymmetry for a threshold of 200 m/s (same as in Sections 5.4 and 5.5), while crosses show the same analysis for a threshold of 350 m/s. The linear fits are also shown by the solid (200 m/s) and dashed (350 m/s) lines.

From Figure 5.8c, both radars have very similar trends for either value of the threshold, which is expected for the radars that are located at the same MLAT. Both radars have also a larger slope for a smaller threshold, which is consistent with Figure 5.8b. The slopes of the fits for the 200-m/s and 350-m/s threshold values are slightly higher than the expected slopes from Figure 5.8b, but not by much. This indicates that the expected and measured E-region asymmetries are very similar both in values and in terms of their dependence on the F-region asymmetry.

Finally, the analysis presented in Figure 5.6 demonstrated that asymmetry in the E-region velocity distribution is strongly controlled by the asymmetry in the convection component, which was indicated by the slopes in the presentation of Figure 5.6c that were very close to 1. A simple modeling analysis presented in this section indeed supports this idea. In addition, this analysis showed that even relatively small shifts in the convection component distribution resulted in large differences between the tails and the expected E-region asymmetries. This indicates a high sensitivity of the E-region asymmetry to small changes in the convection pattern. Importantly, the experimentally-observed dependence of the E-

region asymmetry on the shift of the convection component in Figure 5.8c was generally consistent with the model.

5.7.3 Other Factors that Contribute to the E-Region Velocity Asymmetry

The E-region velocity distributions for SPS have quite different shapes at 06–08 and 16–18 MLT, Figure 5.2a. For example, the high-positive-velocity echoes at 06–08 MLT were "merged" with the low-velocity echoes, whereas the high-negative-velocity echoes were separated from the low-velocity population. The same feature was previously reported by *Makarevich et al.* [2015] for the same monthly dataset. An interesting new result of the current study is that this was also reflected in the overall velocity distribution, where the high-velocity echoes that were merged with low-velocity echoes create an inflection point on the tail of the distribution, whereas the negative velocities clustering near the nominal C_s form a distinct bump-on-tail of the distribution. Moreover, the current study demonstrated that, based on the velocity distributions, Figure 5.3a, and the occurrence distributions for different months (not presented here for brevity), the same difference between the tails of the distributions is present for all months, except March. Further, from Figures 5.5a and 5.5c, the presence of the positive FBI echoes that are merged with the low-velocity echoes (at 06–08 MLT) is mostly independent of season, whereas the occurrence peak of negative velocities (12–16 MLT) shows a strong seasonal variation.

The low-velocity population of echoes is usually associated with the gradient-drift instability (GDI) [*Milan and Lester*, 1999] or could possibly be generated via a non-linear process that would effectively reduce the irregularity phase velocity, e.g. via the three-wave resonance interaction involving primary FBI waves [*Sahr and Farley*, 1995]. Small-scale gradients in the electron density can also destabilize plasma by decreasing the FBI threshold [*Farley and Fejer*, 1975; *St.-Maurice et al.*, 1994]. The fact that the high-positive-velocity SPS echoes are not separated from the low-velocity population can indicate that both mechanisms, GDI and FBI, are operational.

Another factor that can cause the differences between the echoes in the morning and evening sectors is the irregularity height. *Kamide and Brekke* [1977] have reported that the differences between the heights of the eastward and westward electrojets could be as large as 20 km. The height where the E-region irregularities are generated can also differ between pre- and post-midnight sectors [*Moorcroft and Ruohoniemi*, 1987]. The irregularity height is closely related with their generation mechanisms as elaborated on below. The central

E-region (110–115 km) is strongly destabilized through FBI regardless of density gradient strength, whereas at higher altitudes (120–130 km), FBI is more damped and GDI can dominate for sufficiently strong gradients [*Makarevich*, 2016]. Assuming that the high-positive-velocity echoes between 04–10 MLT in Figure 5.2a are originated from a higher altitude, this would be consistent with our hypothesis that both GDI and FBI contribute to this population. In contrast, the high-negative-velocity echoes at 12–18 MLT in Figure 5.2a would then be generated by FBI near the E-region peak.

In contrast with SPS observations, ZHO did not observe a population of high-velocity FBI echoes that was merged with the low-velocity echoes, but it does have a cluster of high-positive-velocity echoes at 12–14 MLT. This cluster is seen in the same MLT sector as the cluster of negative FBI echoes for SPS. The ZHO and SPS velocity polarities are opposite, which is consistent with the opposite orientations of the radars. The MLT extent of ZHO echoes is, however, much smaller ($\sim$2 hours for ZHO vs $\sim$8 hours for SPS). This short-duration cluster of ZHO echoes near 12 MLT may be related to the echoes from the cusp region and therefore is likely to be associated with soft particle precipitation. This observation is somewhat similar to that by *Hu et al.* [2013], who found that the spectral widths measured by ZHO on the dayside are often higher than those on the nightside, which relates to the particle precipitation in the cusp region. The cluster of high-positive-velocity echoes largely disappears during the austral winter, Figure 5.5e, which suggests seasonally-dependent solar illumination may also be a factor. The high-positive-velocity FBI cluster seen by ZHO near 12 MLT could therefore be related to both solar illumination and the particle precipitation near cusp.

One of the more interesting results of the current study was that the high-velocity echo population occupied a relatively wide range of velocity values (as low as 200 m/s). Under the assumption that these echoes are due to FBI, it is important to understand what can cause such a significant reduction in the FBI threshold from its nominal value of 350 m/s. Both horizontal and vertical density gradients have been employed in the past to explain the observed variation in the phase velocity of FBI echoes [e.g. *Fejer et al.*, 1984; *St.-Maurice et al.*, 1994; *Milan and Lester*, 2001; *Lacroix and Moorcroft*, 2001]. The sign of the gradient would determine the enhancement or reduction of the phase velocity from C_s. Strong horizontal gradients could be present near the dayside auroral oval from the intensified particle precipitation associated with the cusp region, whereas the vertical gradients are expected to occur on the top and bottom side of the precipitation enhanced

E-region [*Lacroix and Moorcroft*, 2001].

One can conclude that analysis of the E-region velocity distribution and its asymmetry as well as their diurnal and seasonal variations may contain valuable information on factors that are critical for irregularity production mechanisms such as convection electric field, plasma density gradients, and irregularity production heights. By employing dual and multiple radars, these factors can be decoupled from those related to the radar orientation and position. The analysis conducted in the current study indicates that the two main features can be interpreted as follows. The bump-on-tail feature is most likely associated with FBI echoes, whereas the inflection point feature may indicate that both GDI and FBI contribute to generation of these echoes.

5.8 Summary and Conclusions

The following conclusions can be drawn from the statistical analysis of the SuperDARN South Pole and Zhongshan radar observations of the E-region plasma irregularities with coincident and simultaneous observations of the F-region plasma convection derived from the entire SuperDARN array in the southern hemisphere:

1. The E-region velocity distribution is highly asymmetric. It has a bump-on-tail due to the cluster of echoes near the nominal ion-acoustic speed that are driven by the Farley-Buneman instability and the inflection on the tail most likely due to echoes driven by both the Farley-Buneman and gradient-drift instabilities. The asymmetry of the distribution exhibits a strong seasonal variation. FBI waves from the westward (eastward) electrojet dominate during the austral summer (winter). The distribution of the F-region plasma convection component is approximately Gaussian in shape and has a small bias (shift) that is caused by the asymmetry of the zonal convection component.

2. The high-latitude convection pattern exhibits a significant asymmetry, with the westward convection being dominant at most locations and under most IMF conditions. The asymmetry in the convection pattern is more pronounced at the lower latitudes. The more positive IMF B_z forces the convection to be more symmetric, while the IMF B_y control is strongly dependent on the latitude. The convection pattern asymmetry results in the bias of the convection component distribution, with its sign being dependent on the orientation of the radar.

3. The E-region velocity asymmetry is strongly controlled by the asymmetry in the convection component, which indicates that the asymmetry of the E-region velocity distribution is highly sensitive to small changes in the plasma convection. The bump-on-tail and inflection point in the E-region velocity distribution may also depend on the irregularity height and presence of strong density gradients modifying the FBI threshold value.

Acknowledgements

This work was supported by National Science Foundation grants PLR-1139806 and PLR-1443504. SuperDARN data are freely available through the SuperDARN website at Virginia Polytechnic Institute and State University (http://vt.superdarn.org/). The SuperDARN Zhongshan radar is operated by the Polar Research Institute of China (PI: Dr. Hongquio Hu). The SuperDARN South Pole radar is operated by the University of Alaska Fairbanks (PI: Dr. Bill Bristow). OMNI data are available at National Aeronautics and Space Administration OMNIWeb (http://omniweb.gsfc.nasa.gov/).

5.9 References

Bahcivan, H., D. L. Hysell, M. F. Larsen, and R. F. Pfaff (2005), The 30 MHz imaging radar observations of auroral irregularities during the JOULE campaign, *J. Geophys. Res.*, *110*, A05307, doi:10.1029/2004JA010975.

Bristow, W. A., R. A. Greenwald, S. G. Shepherd, and J. M. Hughes (2004), On the observed variability of the crosspolar cap potential, *J. Geophys. Res.*, *109*, doi:10.1029/2003JA010206.

Buneman, O. (1963), Excitation of field-aligned sound waves by electron streams, *Phys. Rev. Lett.*, *10*, 285–287.

Chisham, G., et al. (2007), A decade of the Super Dual Auroral Radar Network (SuperDARN): scientific achievements, new techniques and future directions, *Surveys in Geophysics*, *28*, 33–109, doi:10.1007/s10712-007-9017-8.

Cowley, S. W. H., J. P. Morelli, and M. Lockwood (1991), Dependence of convective flows and particle precipitation in the high-latitude dayside ionosphere on the X and Y components of the interplanetary magnetic field, *J. Geophys. Res.*, *96*(A4), 5557–5564, doi:10.1029/90JA02063.

Crooker, N. U., and F. J. Rich (1993), Lobe-cell convection as a summer phenomenon, *J. Geophys. Res.*, *98*, 13,403–13,407.

Farley, D. T. (1963), A plasma instability resulting in field-aligned irregularities in the ionosphere, *J. Geophys. Res.*, *68*, 6083–6093.

Farley, D. T., and B. G. Fejer (1975), The effect of the gradient drift term on type 1 electrojet irregularities, *J. Geophys. Res.*, *80*(22), 3087–3090.

Fejer, B. G., and M. C. Kelley (1980), Ionospheric irregularities, *Geophys. Rev.*, *18*, 401–454.

Fejer, B. G., D. T. Farley, B. B. Balsley, and R. F. Woodman (1975), Vertical structure of the VHF backscattering region in the equatorial electrojet and the gradient drift instability, *J. Geophys. Res.*, *80*, 1313–1324.

Fejer, B. G., J. Providakes, and D. T. Farley (1984), Theory of plasma waves in the auroral E region, *J. Geophys. Res.*, *89*, 7487–7494.

Greenwald, R. A., et al. (1995), DARN/SuperDARN: A global view of the dynamics of high-latitude convection, *Space Sci. Rev.*, *71*, 763–796.

Haaland, S. E., G. Paschmann, M. Förster, J. M. Quinn, R. B. Torbert, C. E. McIlwain, H. Vaith, P. A. Puhl-Quinn, and C. A. Kletzing (2007), High-latitude plasma convection from Cluster EDI measurements: method and IMF-dependence, *Ann. Geophysicae*, *25*, 239–253.

Haldoupis, C., and G. Sofko (1976), Doppler spectrum of 42 MHz CW auroral backscatter, *Can. J. Phys.*, *54*, 1571–1584.

Haldoupis, C., E. Nielsen, and H. M. Ierkic (1984), STARE Doppler spectral studies of westward electrojet radar aurora, *Planet. Space Sci.*, *32*, 1291–1300.

Heelis, R. A. (1984), The effects of interplanetary magnetic field orientation on dayside high-latitude ionospheric convection, *J. Geophys. Res.*, *89*, 2873–2880.

Hepner, J. P., and N. C. Maynard (1987), Emperical high-latitude electric field models, *J. Geophys. Res.*, *92*, 4467–4489.

Hu, H., E. Liu, R. Liu, H. Yang, and B. Zhang (2013), Statistical characteristics of ionospheric backscatter observed by SuperDARN Zhongshan radar in Antarctica , *Adv. Polar Sci.*, *24*, 19–31, doi:10.3724/SP.J.1085.2013.00019.

Kamide, Y. R., and A. Brekke (1977), Altitude of the eastward and westward auroral electrojets, *J. Geophys. Res.*, *82*(19), 2851–2853.

Knipp, D. J., A. D. Richmond, B. Emery, N. U. Crooker, O. de la Beaujardiere, D. Evans, and H. Kroehl (1991), Ionospheric convection response to changing IMF direction, *Geophys. Res. Lett.*, *18*(4), 721–724, doi:10.1029/90GL02592.

Lacroix, P. J., and D. R. Moorcroft (2001), Ion acoustic HF radar echoes at high latitudes and far ranges, *J. Geophys. Res.*, *106*(A12), 29,091–29,103, doi:10.1029/2001JA000024.

Makarevich, R. A. (2008), HF radar observations of high-velocity *E*-region echoes from the eastward auroral electrojet, *J. Geophys. Res.*, *113*, A09321, doi:10.1029/2008JA013204.

Makarevich, R. A. (2010), On the occurrence of high-velocity E-region echoes in SuperDARN observations, *J. Geophys. Res.*, *115*, A07302, doi:10.1029/2009JA014698.

Makarevich, R. A. (2016), Toward an integrated view of ionospheric plasma instabilities: Altitudinal transitions and strong gradient case, *J. Geophys. Res. Space Physics*, *121*, 3634–3647, doi:10.1002/2016JA022515.

Makarevich, R. A., A. V. Koustov, A. Senior, M. Uspensky, F. Honary, and P. L. Dyson (2007), Aspect angle dependence of the E-region irregularity velocity at large flow angles, *J. Geophys. Res.*, *112*, A11303, doi:10.1029/2007JA012342.

Makarevich, R. A., V. V. Forsythe, and A. C. Kellerman (2015), Electric field control of E region coherent echoes: Evidence from radar observations at the South Pole, *J. Geophys. Res. Space Physics*, *120*, 2148–2165, doi:10.1002/2014JA020844.

Milan, S. E., and M. Lester (1999), Spectral and flow angle characteristics of backscatter from decametre irregularities in the auroral electrojets, *Adv. Space Res.*, *23*, 1773–1776.

Milan, S. E., and M. Lester (2001), A classification of spectral populations observed in HF radar backscatter from the E region auroral electrojets, *Ann. Geophysicae*, *19*, 189–204.

Moorcroft, D. R., and J. M. Ruohoniemi (1987), Nearly simultaneous measurements of radar auroral heights and Doppler velocities at 398 MHz, *J. Geophys. Res.*, *92*(A4), 3333–3344.

Moorcroft, D. R., and R. T. Tsunoda (1978), Rapid scan doppler velocity maps of the UHF diffuse radar aurora, *J. Geophys. Res.*, *83*, 1482–1492.

Nielsen, E., and K. Schlegel (1983), A first comparison of STARE and EISCAT electron drift velocity measurements, *J. Geophys. Res.*, *88*, 5745–5750.

Nielsen, E., and K. Schlegel (1985), Coherent radar Doppler measurements and their relationship to the ionospheric electron drift velocity, *J. Geophys. Res.*, *90*, 3498–3504.

Nielsen, E., C. F. del Pozo, and P. J. S. Williams (2002), VHF coherent radar signals from the E region ionosphere and the relationship to electron drift velocity and ion acoustic velocity, *J. Geophys. Res.*, *107*, 1012, doi:10.1029/2001JA900111.

Pettigrew, E. D., S. G. Shepherd, and J. M. Ruohoniemi (2010), Climatological patterns of high-latitude convection in the Northern and Southern hemispheres: Dipole tilt dependencies and interhemispheric comparisons, *J. Geophys. Res.*, *115*, A07305, doi:10.1029/2009JA014956.

Ribeiro, A. J., J. M. Ruohoniemi, P. V. Ponomarenko, L. B. N. Clausen, J. B. H. Baker, R. A. Greenwald, and K. Oksavik (2013), A comparison of SuperDARN ACF fitting methods, *Radio Sci.*, *48*, 274–282.

Rich, F. J., and M. Hairston (1994), Large-scale convection patterns observed by DMSP, *J. Geophys. Res.*, *99*, 3827–3844.

Rogister, A., and N. D'Angelo (1970), Type II irregularities in the equatorial electrojet, *J. Geophys. Res.*, *75*, 3879–3887.

Ruohoniemi, J. M., and K. B. Baker (1998), Large-scale imaging of high-latitude convection with Super Dual Auroral Radar Network HF radar observations, *J. Geophys. Res.*, *103*, 20,797–20,811.

Ruohoniemi, J. M., and R. A. Greenwald (1995), Observations of IMF and seasonal effects in high-latitude convection, *Geophys. Res. Lett.*, *9*, 1121–1124.

Ruohoniemi, J. M., and R. A. Greenwald (1996), Statistical patterns of high-latitude convection obtained from Goose Bay HF radar observations, *J. Geophys. Res.*, *101*, 21,743–21,764.

Ruohoniemi, J. M., and R. A. Greenwald (2005), Dependencies of high-latitude plasma convection: Consideration of interplanetary magnetic field, seasonal, and universal time factors in statistical patterns, *J. Geophys. Res.*, *110*, A09204, doi:10.1029/2004JA010815.

Sahr, J. D., and D. T. Farley (1995), Three wave coupling in the auroral E region, *Ann. Geophysicae*, *13*, 38–44.

Shepherd, S. G. (2014), Altitude-adjusted corrected geomagnetic coordinates: Definition and functional approximations, *J. Geophys. Res.*, *119*(9), 7501–7521, doi:10.1002/2014JA020264.

St.-Maurice, J.-P., P. Prikryl, D. W. Danskin, A. M. Hamza, G. J. Sofko, J. A. Koehler, A. Kustov, and J. Chen (1994), On the origin of narrow non-ion-acoustic coherent radar spectra in the high-latitude E region, *J. Geophys. Res.*, *99*, 6447–6474.

Sudan, R. N., J. Akinrimisi, and D. T. Farley (1973), Generation of small-scale irregularities in the equatorial electrojet, *J. Geophys. Res.*, *78*, 240–248.

Chapter 6

Conclusions and Suggestions for Future Research

The first observation of the E-region ionospheric irregularities was made 80 years ago [*Eckersley*, 1937; *Harang and Stoffregen*, 1938]. During this time a tremendous effort has been expended to develop the theory that would explain their origin and characteristics. Constantly advancing experimental setups, we reached the time when it is possible to monitor the dynamics of the plasma convection on the global scale. Yet, there are still more questions to answer until we are able to predict the occurrence and characteristics of the E-region irregularities. This work has contributed towards theoretical and experimental understanding of the irregularity formation, occurrence, and controlling factors. In this chapter, we summarize the most important findings of this research and propose suggestions for the future work.

6.1 Conclusions

One of the main reasons why it is challenging to model the occurrence and characteristics of the E-region irregularities is multiple factors that can control their behavior. The growth rate and the phase velocity of the produced waves in particular depend on both external and local parameters. The local parameters describe the plasma itself, such as the concentrations of neutral and charged particles, the amount of thermal energy that they have, and the gradient in the plasma density associated with their spatial distribution. The external parameters, such as the background magnetic and electric fields, together with the neutral wind velocity, control the plasma motion. The pattern of the irregularities produced in the linear regime in the magnetic-field-perpendicular plane (i.e. in the $\mathbf{k}_\perp$ space) is typically assumed to be controlled by the electric field component in the same plane. In this study, it was demonstrated that one additional parameter affects significantly the distribution in the $\mathbf{k}$ space, namely the parallel electric field. Importantly, it affects both the $\mathbf{k}_\perp$ and $\mathbf{k}_\parallel$ patterns. This introduces significant asymmetries about the plane perpendicular to the magnetic field, which can potentially impact experimentally measured characteristics.

The measured phase velocity of irregularities contains information on all the parameters listed above. Radar observations aim to isolate a particular parameter, i.e. to minimize the influence of the others. In both experimental investigations presented in this body of work (Chapters 4 and 5) the central element was dual radar setup which allowed to perform this minimization to the extent that was not possible with a single radar setup that has been

predominantly used in the past.

In Chapter 4, the first type of a dual radar setup was employed with the SuperDARN MCM and DCE radars probing the E region along the same line and from opposite directions. This allowed focusing only on the control by the aspect angle and altitude. It was demonstrated that the polar cap irregularities are similar to their auroral counterparts, but without the contribution of the destabilizing gradients, due to the unfavorable orientation of the magnetic field in the polar cap. It has also been shown that one more factor can control the occurrence and location of the backscatter from the polar cap, namely the tilt of the strong E layer. It was demonstrated that, in case when the layer is tilted, the aspect angle and the height become important, and when the layer is stratified, the electric field is a controlling factor of the received backscatter. Overall, it was shown that the importance of the controlling factors in the magnetic polar cap depends strongly on the large-scale density conditions.

In Chapter 5, a second type of the dual radar setup has been used in which the SuperDARN SPS and ZHO radars were sampling the same MLAT range from opposite directions. Unlike the first study in which MCM/DCE measurements were coincident in both MLAT and MLT, however, SPS and ZHO were coincident in MLT only in statistical sense, i.e. after collecting observations over each 24-h period. A distinct advantage of the SPS/ZHO setup was however that E-region observations referred to the MLAT range where high-quality data were available on large-scale plasma convection from the entire SuperDARN array in the southern hemisphere. This allowed to investigate factors that control occurrence and polarity of E-region irregularity phase velocity. It has been demonstrated in Chapter 5 that polarity of the E-region irregularity velocity is strongly controlled by that of the convection component. A strong correlation between asymmetries in the velocity distributions in the E- and F-region was found, as expected for irregularities generated predominantly through the Farley-Buneman instability. The unexpected part was the high sensitivity of the E-region distribution to small changes in the convection pattern. One possible interpretation was put forward in this thesis, i.e. that the FBI threshold was lower than perhaps expected and that this modification could be due to the destabilizing density gradients. Even though density gradients are commonly expected to influence the irregularity generation (see review presented in Section 1.3 of this thesis), the previously reported experimental evidence is surprisingly scarce and mostly indirect (see review in Section 1.3.2). In this thesis, an important additional piece of the puzzle was provided, i.e. that small convection changes

may be responsible for large changes in E-region irregularity generation. In addition, it was discovered that the distribution of the convection component exhibits an unexpectedly strong latitudinal variation, with the westward zonal flow being predominant in the southern hemisphere.

It was also demonstrated in Chapter 5 that the E-region velocity distribution exhibits some characteristic features that are seasonally dependent and that this information can potentially be used to reveal further details on the irregularity generation regime. In particular, it was found that the bump-on-tail feature centered at the nominal ion-acoustic velocity in the velocity distribution most likely implies the FBI regime, whereas the inflection point feature may indicate the GDI mode.

From the more practical side, knowing the information about the convection pattern, season, and radar orientation, it is now possible to predict statistical distributions of the E-region irregularity velocity. This brings us ever closer to the ultimate goal of this research, i.e. predicting the E-region plasma irregularity occurrence and characteristics.

6.2 Suggestions for Future Research

In the context of the above discussed overarching goal of the plasma irregularity prediction, the most important question is: What information do we need to know in order to be able to predict the occurrence of the E-region irregularities and what is the priority/importance order of these factors? From this body of work, the top priority should be given to obtaining the vector field of the convection velocity. This information can be deduced from SuperDARN observations by either using standard [*Ruohoniemi and Baker*, 1998] or more advanced data analysis methods [*Bristow et al.*, 2016]. From this information, geomagnetic position of the regions where the convection component exceeds the nominal ion-acoustic speed can be found. The direction of the convection velocity at any given location will define a bisector of the flow angle cone, where the instability is operational. This will allow to predict irregularity occurrence as a function of location as well as the flow and aspect angles.

The next step is further improvement in the model through comparisons of the model predictions with SuperDARN observations in their E-region fields-of-view. In this context, this body of work tells us that the second priority should be given to obtaining the plasma density information for the following reasons. For any given location within their FoVs, radars always sample particular values of the flow and aspect angles. Thus both must

be known for meaningful model-experiment comparisons. The standard tool for obtaining aspect angle information is raytracing simulations [e.g. *Koustov et al.*, 2007]. The complication in this process is that plasma density distribution is rarely available from measurements and is often underestimated by models such as IRI especially in the polar cap. Therefore, it would be better to perform this modeling for the northern hemisphere, where incoherent scatter radars could estimate the plasma density and at least scale up the modeled IRI values. In case when the modeled regions, where the backscatter is predicted to be observed, agree with the SuperDARN E-region observations, that would indicate a correct global positioning of the irregularities. Further, the location of the E-region irregularities should be analysed on a more global scale. It has been generally accepted that many auroral phenomena are geomagnetically conjugate. For example, the oval shape of the Aurora Borealis is conjugate to the Aurora Australis. We propose that the above method can be used to address the question about the conjugate nature of the radar aurora and, through that, of the magnetic conjugacy of the auroral phenomena as a whole.

In addition to further data analysis studies based on the currently available experimental tools, further (and arguably more significant) insights can be obtained from new experiments specifically designed to address the still outstanding issues. One such experiment is described below. As was demonstrated in Chapter 5 of this body of work, the occurrence of the E-region irregularities binned in velocity and MLT was somewhat different even for the radars that are located at the same latitudinal domain. The main reason for this difference is the orientation of radars with respect to the magnetic field and the plasma flow direction. Here we propose one way that can isolate these effects. Figure 6.1 shows the field-of-view of the existing SuperDARN radar in Dome Concordia (known

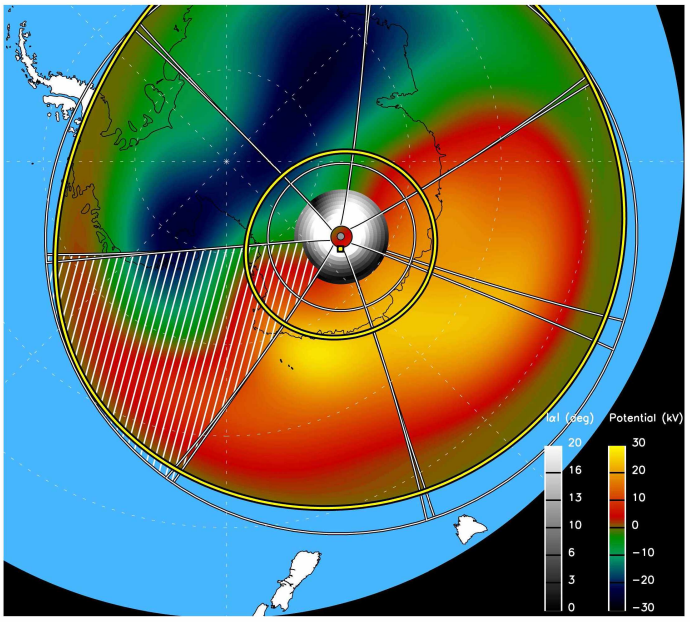

Figure 6.1. SuperDARN Dome Concordia East radar and six proposed radars at the same location.

as Dome C East or DCE) that has been employed in Chapter 4 and that is located very close to the geomagnetic south pole. Utilizing the strategic location of the existing research station, we propose to deploy 6 more radars that would provide a complete coverage of the central portion of the southern polar cap with the short-range radar cells where the E-region backscatter is observed.

In Figure 6.1 the short-range radar cells are coded in the aspect angle magnitude, with the grey scale shown in the bottom-right corner of the diagram. The aspect angles were calculated assuming no refraction. Comparing the data from those radars, the MLT dependence of the backscatter can be fully investigated. As was demonstrated in Chapter 4, when the ionospheric E layer is stratified, the Pedersen signal propagation mode is predominant. This ensures that height effects on the backscatter will be minimized. The radial and azimuthal location of the E-region backscatter, together with the raytracing simulations and the interferometric data, could also be used to estimate the plasma density conditions in the polar cap. The proposed setup will also be very useful for experimental studies in other areas of ionospheric physics. The new radars would significantly improve the accuracy of the convection maps and enable investigations of the polar cap plasma dynamics including observations of three- and four-cell convection patterns, inter-hemispheric comparisons, and studies of the polar cap patches.

In conclusion, this body of work provided further insights into fundamental plasma instability processes, most notably the ubiquitous Farley-Buneman instability. The E-region of the ionosphere is the closest place where we can observe and study the Farley-Buneman instability using radar techniques. By utilizing the data from the SuperDARN short-range gates, our understanding of the processes in the collisional plasma can be significantly improved. When the technological progress in the radar science allows the deployment of the solar radar, this knowledge can be further applied to the investigation of the Farley-Buneman instability in the solar coronae, advancing the understanding of the coronal heating processes.

6.3 References

Bristow, W. A., D. L. Hampton, and A. Otto (2016), High-spatial-resolution velocity measurements derived using Local Divergence-Free Fitting of SuperDARN observations, *J. Geophys. Res. Space Physics*, *121*(2), 1349–1361, doi:10.1002/2015JA021862.

Eckersley, T. L. (1937), Irregular ionic clouds in the E layer of the ionosphere, *Nature*, *140*, 846–847.

Harang, L., and W. Stoffregen (1938), Scattered reflections of radio waves from a height of more than 100 km, *Nature*, *142*, 832–833.

Koustov, A. V., D. André, E. Turunen, T. Raito, and S. E. Milan (2007), Heights of SuperDARN F region echoes estimated from the analysis of HF radio wave propagation, *Ann. Geophysicae*, *25*, 1987–1994, doi:10.5194/angeo-25-1987-2007.

Ruohoniemi, J. M., and K. B. Baker (1998), Large-scale imaging of high-latitude convection with Super Dual Auroral Radar Network HF radar observations, *J. Geophys. Res.*, *103*, 20,797–20,811.